ATOMIC FORCE MICROSCOPY STUDY OF NANO-CONFINED LIQUIDS

A Thesis
Presented to
The Academic Faculty

by

Tai-De Li

In Partial Fulfillment
of the Requirements for the Degree
Doctor of Philosophy in the
School of Physics

Georgia Institute of Technology
August 2008

ATOMIC FORCE MICROSCOPY STUDY OF NANO-CONFINED LIQUIDS

Approved by:

Professor Elisa Riedo, Advisor
School of Physics

Professor Daniel I. Goldman
School of Physics

Professor Uzi Landman
School of Physics

Professor L. Andrew Lyon
Chemistry and Biochemistry Department

Professor Dragomir Davidovic
School of Physics

Date Approved: 4 June 2008

To my beloved families

ACKNOWLEDGEMENTS

I would like to express my deepest gratitude to the countless family members and friends who have supported and helped me through all these year during the pursuit of my PhD. Thanks to Elisa for the guidance of my research, without her, this thesis wouldn't be possible. Thanks to our remarkable collaborators, Uzi and Jianping, for providing valuable discussion and simulations for this work. Thanks to Robert, Marcel, Debin, and Deborah, who were/are in this group and for their assistance in answering my questions. Thanks to my entire family in Taiwan, who support me in the prosecution of my career. Extra special thanks to my mother and my mother in law, who volunteer to share their time to care for my son, allowing me to finish my research and thesis. I send endless appreciation to my wife and my best friend, Li-Ting, for always being there whether I needed her or not. And thanks to my son Benjamin, for making this not an ending, but a new beginning.

TABLE OF CONTENTS

LIST OF TABLES

LIST OF FIGURES

INTRODUCTION

The understanding and ability to manipulate fluids at the nano-scale is a matter of continuously growing scientific and technological interest [1, 2, 3, 4]. This topic is crucial for the design of nano-fluidic devices, and for a better understanding of aquaporine behavior, protein ion channels functionality, and clay swelling [5, 6, 7]. Fluid flow in nano-confined geometries is relevant in biology, polymer science and geophysics. Confined fluids exhibit unique structural, dynamical, and mechanical properties that are different from those of the bulk liquids. Their behavior depends on the degree of confinement, shear rate, temperature, fluid molecular structure, and interactions with boundaries. Surprising effects have been found when liquids are confined to nano-gaps. For example, the electric field induced freezing of water at room temperature [8] and the spontaneous condensation of water in under-saturated pressure at room temperature [9, 10, 11].

Early studies proved that squeezing a molecular liquid between two surfaces leads to oscillating solvation forces and an increase of the shear viscosity [12, 13, 14, 15, 16]. The idea is that, due to confinement, more "order" is induced in the fluid and as a consequence, its viscosity increases. Furthermore, when the distance between the two surfaces is of the order of the liquid molecule, oscillating forces are observed due to transitions between "more" ordered and "more" disordered states, i.e. solvation shells. Indeed, the period of these oscillations is the molecular dimension of the liquid. However, as some agreement has been reached on the behavior of non-polar complex liquids [16, 17, 18, 19, 14, 20], the structure and dynamics of nano-confined water remain unclear despite the intense scientific scrutiny. Some studies show that the structure of nano-confined water is ice-like [21, 22, 23], some researchers find a liquid

phase [24, 25, 26] and other investigations suggest a gas-like behavior [27, 28, 29, 31]. Controversial results have also been found about solvation shells [32, 24, 33, 34, 35]. This controversy is partially due to experimental limitation, in term of force resolution, spacial resolution and confining-surfaces choices. These limitations have, for example, prevented an understanding of how the topography and wettability of the confining surfaces determine the structural and dynamical response of nano-confined water.

Oscillating solvation forces in water have only been experimentally measured when at least one of the two confining surfaces was hydrophilic [32, 33, 36]. Experiments on graphite (hydrophobic) have suggested the absence of oscillations in force-distance curves [37]. Molecular dynamics simulations show that when water is confined between hydrophobic surfaces, a gas like structure can be promoted [29, 30]. Also X-ray reflectivity [27] and neutron scattering measurements [28, 31] have highlighted a gas-like water structure at the interface of a hydrophobic polymer floating on water. This suggests that chemistry and wettability of the confining surfaces might play a key role in determining water structure.

The key questions of this thesis are the following:

1. What is the structure and dynamics of water in the close proximity of a solid boundary surface?
2. What is the role of surface roughness and wettability?
3. How does water differ from other liquids?

This thesis explores the structure and dynamic properties of liquids enduring nano-confined geometries. In the **chapter I** of this thesis, we present an overview of the basic concepts of the physics of confined fluids, as well as a brief review of the different methods used to study surface forces in liquids at the nano-scale. In the experiments presented in this thesis, we measure the properties of nano-confined liquids by means of state-of-the-art atomic force microscopy (AFM) techniques (see

[h]

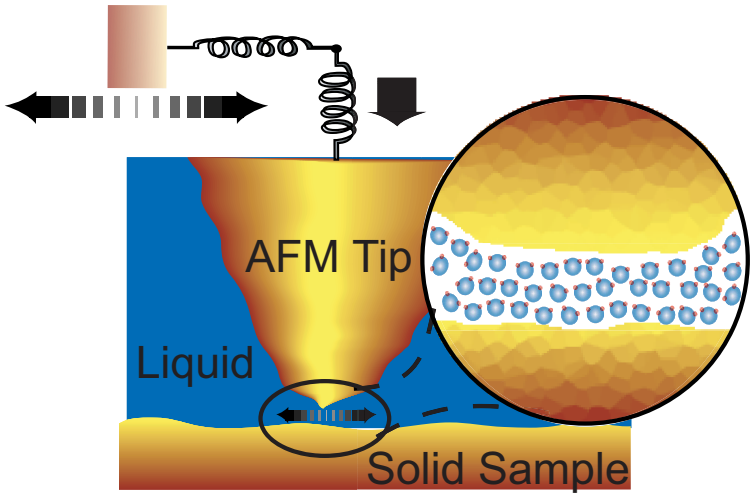

Figure 0.0.1: *The schematic of the experimental setup used in this thesis.*

chapter II). The force acting on the AFM tip is measured while the tip approaches the sample surface in liquid and the liquid molecules in between the tip and sample surface are naturally confined (as shown in Fig. 0.0.1). Furthermore, the tip is oscillated laterally (parallel to the surface) while the approaching, thus the lateral force is measured simultaneously with the normal force and the distance between the tip and sample. By utilizing information from the measured normal and lateral force, the structural and dynamical properties of nano-confined liquids are investigated.

In **chapter III**, we show the experiments that find oscillatory solvation forces for hydrophilic surfaces (mica and glass) and less pronounced oscillations for a hydrophobic surface (graphite). In this chapter, we also present lateral force measurements that indicates , for sub-nanometer hydrophilic confinements, orders of magnitude increase of the viscosity with respect to bulk water, agreeing with a simulated sharp decrease in the diffusion constant. No viscosity increase is observed for hydrophobic surfaces.

Chapter IV presents the results of the dynamic response of nano-confined fluids. In this part of the research, the shear rate of the AFM tip is changed in a large range of values by using different shear amplitudes and/or frequencies. Surprisingly,

the viscoelastic response of nano-confined water is not linear; more specifically, it depends on shear amplitude. Furthermore, we observe the same non-linear behavior in both nano-confined water and nano-confined silicon oil. This highly non-linear behavior can be described by a theory developed for bulk complex fluids, e.g., colloid system, glassy materials, or gels. The origin of this non-linear phenomenon is the extremely slow intrinsic relaxation time of the nano-confined liquid molecules. By analyzing the viscoelastic behavior of nano-confined water, the intrinsic relaxation time is found to be about 10 orders of magnitude slower than that of bulk water. This value is comparable with the dielectric relaxation time measured in supercooled water at 175 K. In other words, the local temperature seems to be reduced by the confinement that reduces the thermal motion of the "trapped" molecules.

Based on the results of this thesis, two future developments are proposed in **chapter V**. In the first section of chapter v, we introduce the concept of "slip length" that provides an interpretation of the different viscous behavior observed with hydrophilic and hydrophobic confinements. In the second section, we propose new method to study confined liquids by means of nano-fabricated surfaces. Based on a new chemical nano-lithography technique developed in our group [38], we envisage to design confinement geometries with the desired chemical properties and dimensions. Some ideas based on this unique ability of manipulating nano-confined geometries are presented and discussed.

SUMMARY

In this thesis, we investigate the structural and dynamical properties of nano-confined liquids by means of a new AFM-based technique that has the ability to measure normal force, lateral force, and the distance between the AFM tip and the sample simultaneously. Thanks to the mechanical stability of our apparatus, a judicious choice, and a new mechanical drift analysis, we are able to measure the tip-sample distance with sub-angstrom resolution, all the way down to the last liquid layer.

For tip-surface distances, 0 ± 0.03 nm $< d < 2$ nm, experiments and grand canonical molecular dynamics simulations (performed by Prof. Landman's group) find oscillatory solvation forces for hydrophilic surfaces, mica and glass, and less pronounced oscillations for a hydrophobic surface, graphite. For sub-nanometer hydrophilic confinement, the lateral force measurements show orders of magnitude increase of the viscosity with respect to bulk water, agreeing with a simulated sharp decrease in the diffusion constant. No large viscosity increase is observed for hydrophobic surfaces.

Furthermore, the viscoelastic dynamics of nano-confined wetting liquids is studied. We observe a nonlinear viscoelastic behavior remarkably similar to that widely observed in metastable complex fluids. We show that the origin of the measured nonlinear viscoelasticity in nano-confined water and silicon oil is a strain rate dependent relaxation time and slow dynamics. By measuring the viscoelastic modulus at different frequencies and strains, we find that the intrinsic relaxation time of nano-confined water is in the range $0.1 - 0.0001$ s, orders of magnitude longer than that of bulk water, and comparable to the dielectric relaxation time measured in supercooled water at $170 - 210$ K.

CHAPTER I

FUNDAMENTALS

In this thesis, the rheological properties of nano-confined liquids are studied by measuring the interaction forces between two surfaces sandwiching the liquid. In order to interpret the force measurements in this thesis, it is necessary to understand all the interactions that participate in the force measurements.

In the first section of this chapter, we will discuss the surface forces acting between the surfaces of two solids. After discussing the force between two surfaces sandwiching liquids, it is essential to discuss the properties of the confined liquid itself, which is the main purpose of this thesis. As it will become clear in chapter III and IV, the viscoelasticity theory used to describe the rheological behaviors of the soft matter, such as polymers, gels, or glassy materials is a good theoretical tool for interpreting the rheological behaviors of nano-confined liquids.

Since the major technique used in this thesis is the atomic force microscopy (AFM), a brief review of AFM is presented in third section of this chapter.

In the final part of this chapter, we will present and compare some previous remarkable studies on nano-confined fluids performed by other groups by means of other apparatus or techniques.

1.1 Surface Forces

1.1.1 Van der Waals Force

By definition, the van der Waals (vdW) force is a relatively weak attraction between neutral atoms and molecules arising from the polarization induced in each particle by the presence of other particles. In order to interpret the Van der Waals force, we need to understand all the interactions related to dipoles.

From the classical electro-magnetic theory, the *Coulomb potential* between two electric charges in vacuum is:

$$V = \frac{Q_1 Q_2}{4\pi\epsilon_0 \cdot d} \tag{1.1.1}$$

where Q_1 and Q_2 are the charges, d is the distance between them and ϵ_0 is the permittivity of free space. From the *Coulomb potential*, the energy between two dipoles can be calculated, and it is known as the *Keesom energy* [39]:

$$V = -\frac{\mu_1^2 \mu_2^2}{3(4\pi\epsilon_0)^2 k_B T} \frac{1}{d^6} \tag{1.1.2}$$

where, μ_1 and μ_2 are the dipole moments for these two dipoles. Also the energy between a static dipole and a polarizable molecule can be calculated, and it is known as the *Debye energy* [40]:

$$V = -\frac{\mu^2 \alpha}{(4\pi\epsilon_0)^2} \frac{1}{d^6} \tag{1.1.3}$$

where the α is the polarizability defined as $\mu_{ind} = \alpha E$, where E is an external applied electric field and μ_{ind} is the dipole moment induced by the electric field.

The next term of the dipole-related potential energy is the one between two polarizable molecules. A proper calculation of this interaction needs quantum mechanics perturbation theory, but the general form of the result can be obtained by the following simple argument [43]. In the Bohr model of the hydrogen atom, the smallest orbital radius, a_0, is the ground state and Bohr calculated that:

$$a_0 = \frac{e^2}{8\pi\epsilon_0 h\nu} \tag{1.1.4}$$

where e is the proton charge, h is Planck's constant, and ν is a characteristic frequency associated with the electron's motion around the nucleus. Although the H atom has no permanent dipole, it can be regarded as having an instantaneous dipole momentum, $p \approx a_0 e$. The electric field of this instantaneous dipole at a distance d is:

$$E \approx \frac{p}{4\pi\epsilon_0 d^3} \approx \frac{a_0 e}{4\pi\epsilon_0 d^3} \tag{1.1.5}$$

If a polarizable molecule is nearby, it is polarized by this electric field and the induced dipole momentum is:

$$p' = \alpha E \approx \frac{\alpha a_0 e}{4\pi\epsilon_0 d^3} \tag{1.1.6}$$

The potential between p and p' is then:

$$V = -\frac{pp'}{4\pi\epsilon_0 d^3} = -\frac{\alpha a_0^2 e^2}{(4\pi\epsilon_0)^2 d^6} \tag{1.1.7}$$

The d^{-6} distance dependence and the main physical coefficients are the same as in the result deduced from the perturbation theory. Instead of two hydrogen atoms, the general situation of two molecules can be obtained as the *London dispersion Energy* [41]:

$$V = -\frac{3}{2}\frac{\alpha_1\alpha_2}{(4\pi\epsilon_0)^2}\frac{h\nu_1\nu_2}{(\nu_1+\nu_2)}\frac{1}{d^6} \tag{1.1.8}$$

where $h\nu_1$ and $h\nu_2$ are the ionization energies for these two molecules.

The vdW force is the sum of the Keesom, the Debye and the London dispersion interaction, i.e., all the terms that consider dipole interactions. All three terms contain the same distance dependence, $V \propto d^{-6}$, and usually the London dispersion term is dominating. By integrating over different geometries, the vdW potential energy for several commonly used geometries can be calculated and they are shown in Fig. 1.1.1.

The geometry of our AFM experiments where a silicon conical tip approaches a flat mica surface in water, can be represented by a sphere and half-space, with the $d \ll R$ approximation, the vdW force can be written as (see Fig. 1.1.1):

$$F = -\frac{AR}{6d^2} \tag{1.1.9}$$

The AFM tip radius is $R \sim 30$ nm and the Hamaker constant for mica/silicon in water is $A \sim 10^{-19}$ J. The van der Waals force at $d = 1$ nm is thus ~ 0.5 nN.

1.1.2 Electrostatic Force

As mentioned in section 1.1.1, the vdW force between two particles in a medium is always attractive. Therefore if the vdW force is the only interaction, all dissolved

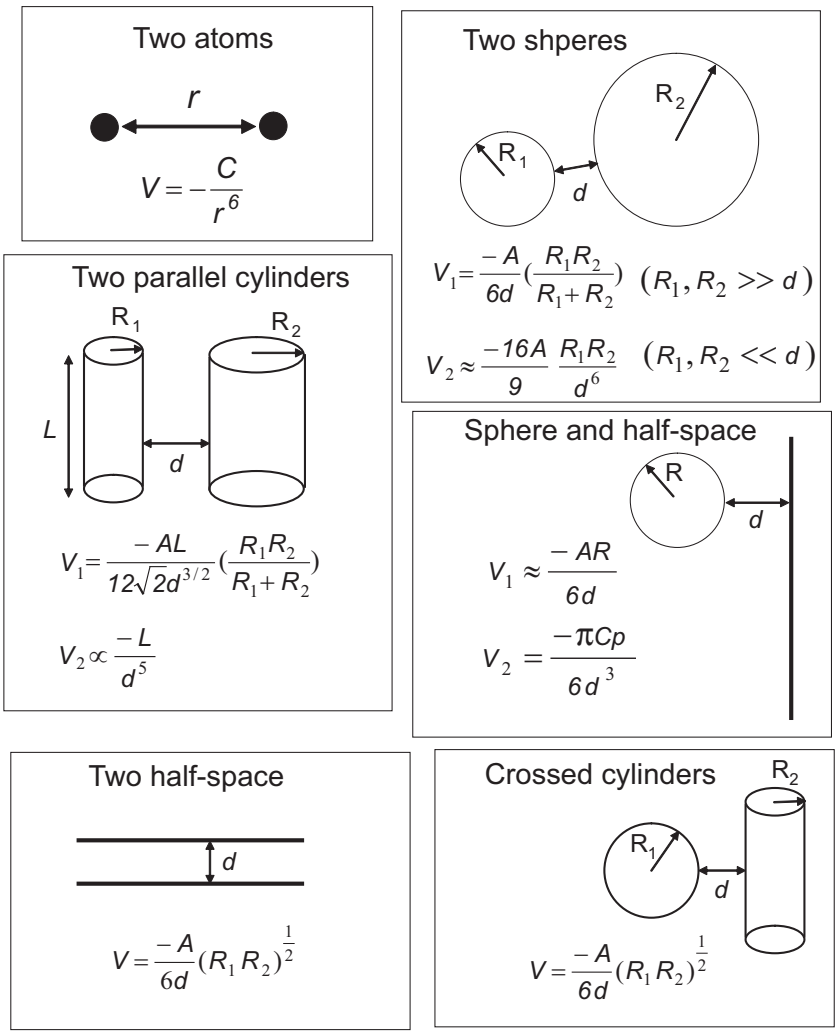

Figure 1.1.1: *The Van der Waals potential for several common geometries. The Hamaker constant A is defined as $A = \pi^2 C \rho_1 \rho_2$ where ρ_1 and ρ_2 are the number of atoms per unit volume in two bodies and C is the coefficient in the atom-atom pair potential. V_1 and V_2 are the potentials for the dimension of the objects much larger and smaller than the distance (d), respectively.*

particles are expected to stick together (coagulate) as a mass of solid material in liquids. Also our bodies will be subject to the same fate since we are composed of 75% water. However, it does not happen, because particles suspended in water or in any other liquid with high dielectric constant, are usually charged, and the repulsive electrostatic force prevents the coagulating. Other repulsive forces that also can prevent the coagulating, will be presented in following sections.

The charge of the particle surface in liquids has two origins: i) the ionization or dissociation of surfaces and ii) the adsorption of ions from the solution onto an uncharged surface. In some ionic conditions, even the air-water and hydrocarbon-water interfaces can become charged in this way. Whatever the charging mechanism, the final surface charge is balanced by the counterions present in the solution, which are bound or usually transient to the surface, as shown in Fig. 1.1.2. These charged regime is usually called the diffuse electric double layer, thus the force due to it is called the double layer force.

Because of the charged surfaces, the ions density in the solution is going to be redistributed and the potential energy is no more a constant in between the two flat charged surfaces as shown in Fig 1.1.2. From classical electro-magnetism, the potential energy (per unit area) between these two charged surfaces can be written as [13]:

$$V(d) = 64\pi kTC_0\gamma^2\lambda_D \approx \frac{2\sigma_1\sigma_2\lambda_D}{\varepsilon\varepsilon_0}e^{-\frac{d}{\lambda_D}} \tag{1.1.10}$$

where C_0 is the ion concentration, $\gamma = \frac{1}{2}[\tanh(\frac{e_0\Psi_1}{4k_BT}) + \tanh(\frac{e_0\Psi_2}{4k_BT})]$ (ψ_1 and ψ_2 are the effective surface energy of the two surfaces in water and e_0 is the electron charge), σ_1 and σ_2 are the surface charge density of the two plates, ε is the permittivity of the liquid in between the plates, and λ_D is the *Debye Length*. The magnitude of the Debye length depends only on the properties of the liquid and not on any property of the surfaces such as its charge or potential. At room temperature, the Debye length

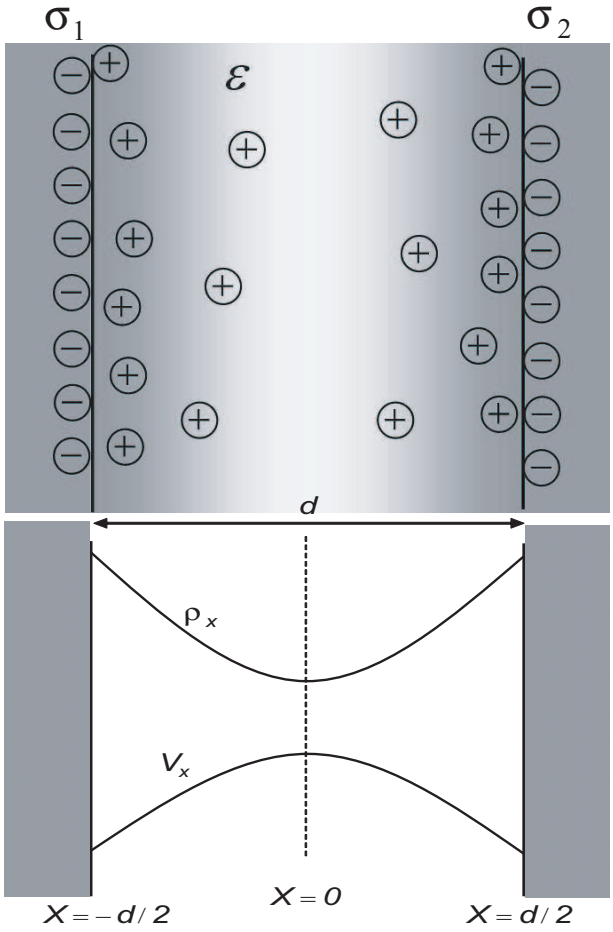

Figure 1.1.2: *The schematic of the charge density and potential energy of the double layer effect between two plates separated by a distance d. V_x and ρ_x are the potential energy and charge density as the function of x.*

of aqueous solution is:

$$\lambda_D = \frac{0.304}{\sqrt{[NaCl]}} nm \qquad \text{for } 1:1 \text{ electrolytes (e.g., } NaCl) \tag{1.1.11}$$

$$= \frac{0.176}{\sqrt{[CaCl_2]}} nm \qquad \text{for } 1:2 \text{ electrolytes (e.g., } CaCl_2) \tag{1.1.12}$$

$$= \frac{0.152}{\sqrt{[MgSO_4]}} nm \qquad \text{for } 2:2 \text{ electrolytes (e.g., } MgSO_4) \tag{1.1.13}$$

The double layer force together with the van der Waals force constitute the DLVO theory (Derjaguin, Landou, Verwey, and Overbeek).

1.1.3 Derjaguin Approximation

In order to derive the double layer interaction in different geometries, the straightforward method is to integrate the point-to-point potential energy over all the surface area. It is very time consuming. Fortunately, a useful approximation can be easily used to derive the force between two curved surfaces from the potential energy per unit area between two planar surfaces. This approximation is based on the situation that the distance between these two surfaces is much smaller than the radii of them, $d \ll R_1,\ R_2$. For two spherical surfaces, the force is:

$$F(d) \approx 2\pi(\frac{R_1 R_2}{R_1 + R_2})V(d) \tag{1.1.14}$$

where $F(d)$ is the interacting force between two spheres and $V(d)$ is the interacting potential energy (per unit area) between two plates of the same material of the spheres. This is called the *Derjaguin approximation* [42]. It is applicable to any type of force law, whether attractive, repulsive, or oscillatory, as long as the condition $d \ll R_1,\ R_2$ is satisfied. Also, the Derjaguin approximation for two right-angle-crossed cylinders gives:

$$F(d) \approx 2\pi\sqrt{R_1 R_2}V(d). \tag{1.1.15}$$

Note that for two cylinder of equal radii ($R_1 = R_2 = R$), it reduces to the same result as for a sphere of radius R near a flat surface:

$$F(d) \approx 2\pi R V(d). \tag{1.1.16}$$

By applying the Derjaguin approximation to Eq. 1.1.10, the double layer force between a sphere and a flat surface is given by:

$$F(d) \approx \frac{4\pi R \sigma_1 \sigma_2 \lambda_D}{\varepsilon \varepsilon_0} e^{-\frac{d}{\lambda_D}}. \tag{1.1.17}$$

The other practical form of Eq. 1.1.17 can be written as:

$$\begin{aligned} F(d) &= \alpha \lambda_D R \gamma^2 \exp(-\frac{d}{\lambda_D}) \\ \alpha &= 128\pi C_0 \; k_B T \\ \gamma &= \frac{1}{2}[\tanh(\frac{e\Psi_1}{4k_B T}) + \tanh(\frac{e\Psi_2}{4k_B T})] \end{aligned} \tag{1.1.18}$$

where k_B is Boltzmann's constant, T is the absolute temperature, λ_D is Debye length, R is the spherical radius, e is the electron charge, Ψ_1 and Ψ_2 are the effective surface energies of the two surfaces in the liquid, C_o is the ionic concentration.

In our AFM experiments, when a silicon tip approaches a flat mica surface in water, the surface charge density of mica and silicon are $\sigma_{mica} \approx -0.0025 \; C/m^2$ and $\sigma_{silicon} \approx -0.032 \; C/m^2$; the permittivity of water and vacuum are $\varepsilon_{water} = 80 \; C^2/m^2N$ and $\varepsilon_0 = 8.8542 \times 10^{-12} \; C^2/m^2N$; the Debye length for water in air is $\lambda_D = \frac{0.304}{\sqrt{10^{-6}}} \approx 300$ nm (pH value of water in air is ~ 6), and the radius of the tip is $R = 30$ nm. The double layer force at $d = 1$ nm is about 12 nN, which is much larger than the van der Waals force. However due to the extremely long Debey length of water in air, the double layer force is very uniform for a short distance range (as shown in Fig. 1.1.3), which is the range where we measure forces in our experiments on nano-confined liquids.

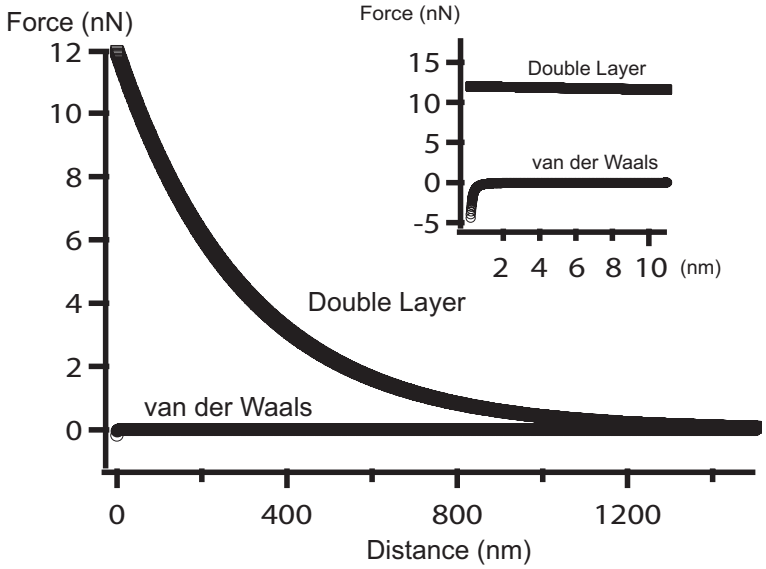

Figure 1.1.3: *The numerical result of the double layer and van der Waals force for a silicon tip approaching the flat mica surface in water. The double layer force dominates the DLVO until the distance smaller than* 1 *nm. The inset shows both of them for* $d < 10$ *nm, which is the same regime of our experiment.*

1.1.4 Structural Force

When the distance between two surfaces or particles in liquids is smaller than several nanometers, continuum theories of van der Waals and electric double layer forces usually fail to describe the interaction between them. This is because either one or both the DLVO forces break down or there are non-DLVO interactions come into play at small separations. These non-DLVO forces can be monotonically attractive, monotonically repulsive, or oscillatory in different circumstances, e.g., different geometries, different liquids, or different surfaces.

In order to understand how the structural force behaves between two surfaces, we have to know the way solvent molecules pack themselves on an isolated surface. Previous studies indicate that the liquid density profile does not oscillate at a liquid-vapor or liquid-liquid interface, but a very different situation arises at a liquid-solid interface [44]. The geometric constraining of the solid wall and the attractive interaction between a solid wall and liquid molecules and force the liquid molecules to

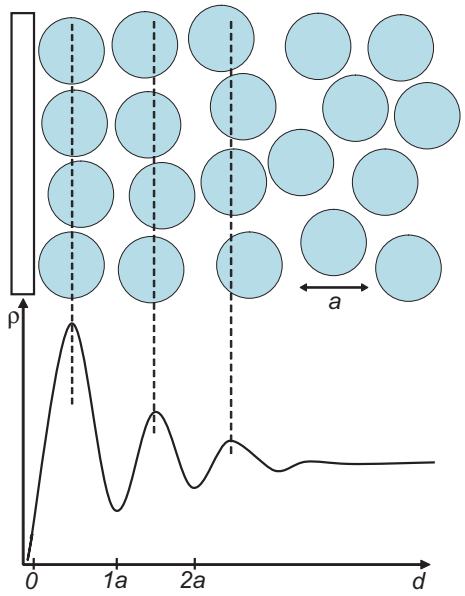

Figure 1.1.4: *The schematic of the density profile of the liquid molecules on an attractive flat surface. a is the diameter of the liquid molecules.*

structure into quasi-discrete layers. This layering is reflected in a oscillatory density profile as shown in Fig. 1.1.4, which extend several molecular dimensions into the liquid.

Now, we consider two of the same isolated surfaces in the liquid, approaching to each other. During the approaching, the interaction between them can be described by the DLVO forces until the distance between them is less than some molecular dimensions. The interacting force between the two surfaces starts to oscillate with the distance due to the transition between layering and non-layering structures, see Fig. 1.1.5. In a first approximation, the oscillation in terms of pressure between these two surfaces may be described by an exponentially decay cos-function:

$$P(d) \approx -kT\rho_f(\infty)\cos(2\pi d/a)e^{-d/a} \tag{1.1.19}$$

where k is the Boltzmann constant, T is the temperature, $\rho_f(\infty)$ is the bulk liquid density, d is the distance between these two surfaces, and a is the radius of the liquid molecule.

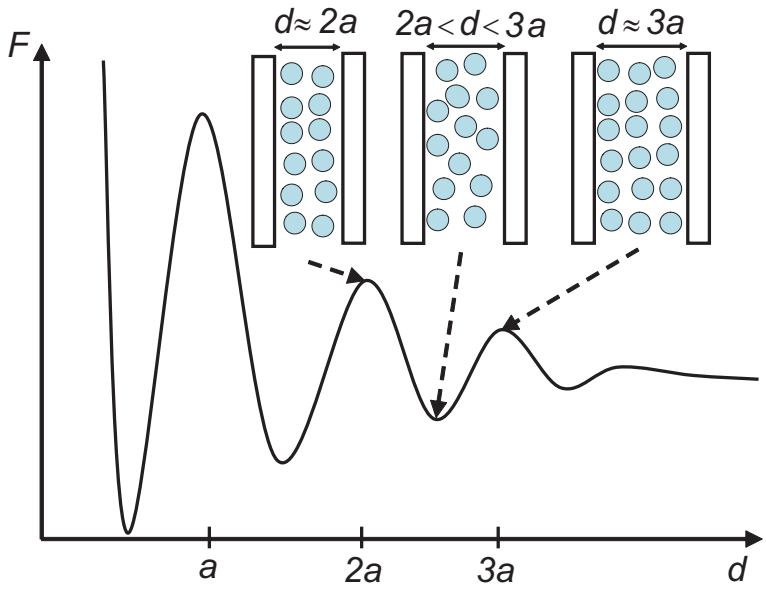

Figure 1.1.5: *The schematic of the interacting force between two flat surfaces separated by distance d. Due to the transition between layered and non-layered liquid molecules by varying the distance, the interacting force is oscillating with d.*

1.1.5 Hydrodynamic Force

The motion of a particle moving in a liquid can be described by the equation:

$$\eta \bigtriangledown^2 \overrightarrow{v} - \bigtriangledown P + F_b = \rho_f (\frac{\partial \overrightarrow{v}}{\partial t} + \overrightarrow{v} \cdot \bigtriangledown \overrightarrow{v}) \tag{1.1.20}$$

where $\overrightarrow{v}$ is the velocity of the fluid flow past the particle, ρ_f is the fluid density, P is the pressure, η is the dynamic viscosity of the fluid, t is the time, and F_b is the body volume force exerted on the particle. For a spherical particle under gravity ($\overrightarrow{g}$), F_b is:

$$\overrightarrow{F_b} = \frac{4}{3}\pi R^3 (\rho_p - \rho_f)\overrightarrow{g} \tag{1.1.21}$$

where ρ_p and R are the density and radius of the particle. For incompressible liquids, we have:

$$\bigtriangledown \cdot \overrightarrow{v} = \frac{\partial v_x}{\partial x} + \frac{\partial v_y}{\partial y} + \frac{\partial v_z}{\partial z} = 0 \tag{1.1.22}$$

Equations 1.1.20 and 1.1.22 together are called the *Navier-Stokes* equation. The *Navier-Stokes* equation is a highly non-linear equation and the complete solution

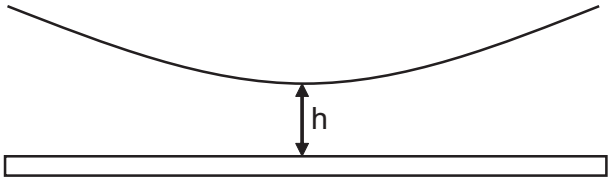

Figure 1.1.6: *A spherical particle approaching a flat surface.*

only exits for simple geometries. Fortunately, in most of the cases, the hydrodynamic steady-state is established very quickly, then the $\frac{\partial \overrightarrow{v}}{\partial t}$ can be neglected. Also, due to the small particle size ($\leq \mu$m), the Reynolds number is small ($Re = \frac{|\rho \overrightarrow{v} \cdot \bigtriangledown \overrightarrow{v}|}{|\eta \bigtriangledown^2 \overrightarrow{v}|} = \rho \frac{vR}{\eta} \leq 10^{-2}$ [43]) and the convective force term ($\rho \overrightarrow{v} \cdot \bigtriangledown \overrightarrow{v}$) can be neglected respected to the viscous force term ($\eta \bigtriangledown^2 \overrightarrow{v}$). By considering a sphere particle driven to approach a plane surface in liquids (Fig. 1.1.6), the body force F_b can be neglected. Therefore, the *Navier-Stokes* Eq. becomes:

$$\eta \bigtriangledown^2 \overrightarrow{v} = \bigtriangledown P \tag{1.1.23}$$

After taking the non-slip boundary condition and the geometric symmetry in Fig. 1.1.6 into account, the hydrodynamic force between the spherical surface of the particle and the plane can be deduced as [45]:

$$F = -\frac{6\pi\eta R^2}{h}\frac{dh}{dt} \tag{1.1.24}$$

In our experiments, for an AFM tip approaching to a flat mica surface in water, the approaching speed is 0.2 nm/s, the tip radius is 30 nm, and the viscosity of *bulk* water is about mPa·s (10^{-3} kg/m·s). The force at $d = 1$ nm should be about 3×10^{-10} nN, which is way too small for the sensitivity of our AFM force measurements.

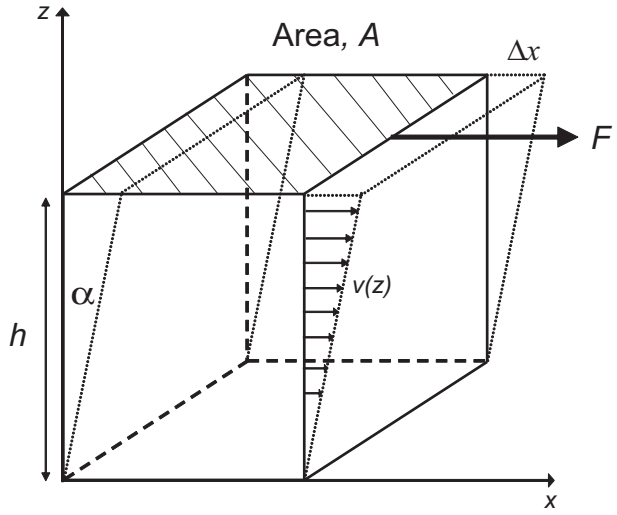

Figure 1.2.1: *Schematic of how the soft material behaves in between two plates when one plate is moving and the other one is stationary.*

1.2 Viscoelasticity of Soft Matter

1.2.1 The General Response to Shearing Stress

The ideal behavior for an elastic solid experiencing a tensile stress S_T is described by the Hook's Law:

$$S_T = F/A = Y\gamma \tag{1.2.1}$$

where Y is called the *Young's modulus* of the material. The strain γ is in this case the relative change in length. The corresponding behavior under a shearing stress is described as:

$$S = F/A = G\gamma \tag{1.2.2}$$

where G is the shear modulus of the material and γ is defined as $\gamma = \tan\alpha = \triangle x/h$, as shown in Fig. 1.2.1. Many solids follow Eq. 1.2.2 for small stresses. Under a limit stress S_L, they will recover completely when the stress is removed. If $S > S_L$, the material suffers permanent deformation, i.e., flow or creep occurs and the solid has begun to exhibit some of the characteristics of a plastic or liquid.

For an ideal liquid-like material, the applied shearing stress is directly proportional

to the rate of strain ($\dot{\gamma} = d\gamma/dt$):

$$S = \eta\dot{\gamma} \tag{1.2.3}$$

where the proportionality constant, η, is the viscosity of the liquid-like material. Consider the situation shown in Fig. 1.2.1 where the liquid material is confined between two plates ($z = 0$ and $z = h$). The lower plate is stationary and the upper plate is being pulled at a velocity, v, by the shearing stress. It is assumed that the liquid in contact with both the planar surfaces has no slippage against these surfaces. Thus, the velocity of the liquid confined between these plates has a gradient as shown in Fig. 1.2.1. The rate of shear/strain, $\dot{\gamma}$, for this simple shear regime is equal to the velocity gradient v/h. In the more general case $\dot{\gamma} = dv(z)/dz$.

However, in most of the cases, the study of soft materials reveals that either liquid-like or solid-like behavior is an exception. In general, a soft material is viscous and elastic (for example, the clay minerals). Such materials are said to be *visco-elastic* and they may be intrinsic liquid or solid depending on which state is dominant. For the viscoelastic materials, the history of deformation may influence its present state. An introduction to this theory is given in Ref. [46]. By the effect of the sequential change in strain is assumed to be additive, the stress for general viscoelastic materials can be written as:

$$S(t) = \int_{-\infty}^{t} G(t - t')\dot{\gamma}(t')dt' \tag{1.2.4}$$

where $G(t)$ is called the shear/relaxation modulus.

1.2.2 The Response to an Oscillating Strain

Consider a viscoelastic material that undergoes a periodic strain with frequency ω:

$$\gamma = \gamma^0 \sin \omega t \tag{1.2.5}$$

and

$$\dot{\gamma} = \omega\gamma^0 \cos \omega t. \tag{1.2.6}$$

where the γ^0 is the amplitude of the strain. By substituting γ and $\dot{\gamma}$ into Eq. 1.2.4 with $t - t' = \tau$, the time dependent stress can be written as:

$$S(t) = \int_0^\infty G(\tau)\omega\gamma^0 \cos[\omega(t-\tau)]d\tau \tag{1.2.7}$$

$$= \gamma^0[\omega \int_0^\infty G(\tau) \sin\omega\tau d\tau] \sin\omega t + \gamma^0[\omega \int_0^\infty G(\tau) \cos\omega\tau d\tau] \cos\omega t \tag{1.2.8}$$

τ is called the relaxation time which is the time needed for a material to relax back to the original shape under a stress. Thus, when $\tau \to \infty$, the shear modulus will converge and the material is liquid-like since a liquid can not permanently support a shearing stress. The terms in square brackets are functions of ω but not t and we can write

$$S(t) = \gamma^0(G' \sin\omega t + G'' \cos\omega t) \tag{1.2.9}$$

where G' is a modulus that measures the ratio of the *in-phase* stress to the strain. This is the shear storage modulus, which is the elastic part of the viscoelastic material. On the other hand, the G'' is the *out-of phase* modulus (shear loss modulus), which is the viscous part of the viscoelastic material. For a purely elastic material, the stress and strain are in phase and $G'' = 0$ and $G' = G$. For a purely viscous liquid ($G' = 0$), according to Eq. 1.2.3:

$$\eta = S/\dot{\gamma} = S/[\omega\gamma^0 \cos\omega t] = G''/\omega. \tag{1.2.10}$$

Since the the viscoelastic behavior can also be described by the phase lag, δ, between stress and strain. The stress can also be written as:

$$S = S^0 \sin(\omega t + \delta) = S^0 \cos\delta \sin\omega t + S^0 \sin\delta \cos\omega t \tag{1.2.11}$$

By comparison with Eq. 1.2.9, we have:

$$G' = \frac{S^0}{\gamma^0} \cos\delta \tag{1.2.12}$$

$$G'' = \frac{S^0}{\gamma^0} \sin\delta. \tag{1.2.13}$$

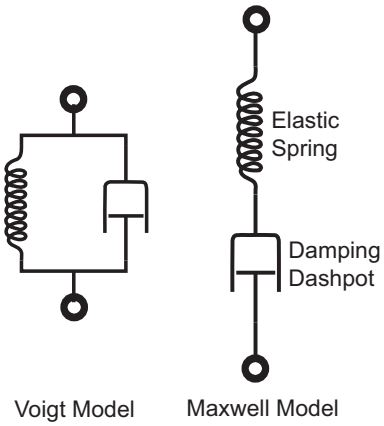

Figure 1.2.2: *The schematic of the Maxwell model and Voigt model for viscoelastic materials.*

1.2.3 Maxwell Model and Voigt Model

The simplest mechanical model analogous to a viscoelastic system is one elastic spring coupled with a damping dashpot, either in series (Maxwell Model) or in parallel (Voigt Model) (as shown in Fig. 1.2.2).

Following the Maxwell model for a material under a periodic strain as in Eq. 1.2.5, the shearing storage and loss modulus can be written as [46]:

$$G' = \frac{G_0 \omega^2 \tau^2}{1 + \omega^2 \tau^2} \tag{1.2.14}$$

$$G'' = \frac{G_0 \omega \tau}{1 + \omega^2 \tau^2}. \tag{1.2.15}$$

where τ is the relaxation time which is a measure of the time required for stress relaxation. For the Voigt model, we have:

$$G' = G_0 \tag{1.2.16}$$

$$G'' = G_0 \omega \tau'. \tag{1.2.17}$$

where τ' is defined as the retardation time which is a measure of the time required for the extension of the spring to its equilibrium length while retarded by the dashpot.

It is important to point out that the Maxwell model describes stress relaxation instead the Voigt model does not. A simple picture for interpreting these models, is

to consider a sudden strain applied to both of them at $t = 0$ and the strain is fixed as a constant for $t > 0$. In the Voigt model, the deformation of the spring is fixed with the fixed strain and the stress (proportional to the force) is fixed, too. There is no stress relaxation in this circumstance. In the Maxwell model, the deformation of the spring is going to relax while the damping dashpot relaxes. In this circumstance, the stress is not a constant and decays with time.

1.3 Surface Force Measurements: Atomic Force Microscopy

The atomic force microscopy is the most popular and powerful tool for measuring forces at the nano-scale since it was invented in 1986 [47]. It is a cantilever-based technique for imaging topology and measuring forces. Figure 1.3.2 shows how the AFM detects forces. The tip is located at the end of the cantilever and facing down toward the sample surface. A piezo scanner is used to move the cantilever/tip in x-, y- and z-direction by applying voltages to deform the piezo as shown in Fig. 1.3.1. Forces between the tip and the sample surface cause the cantilever to bend, or deflect. The normal force acting to the apex of the tip makes the cantilever to bend and the lateral force makes the cantilever to torque. A laser is projected onto the back of the cantilever and its reflection is detected by a four-quadrant-photo-detector as shown in Fig. 1.3.2. The bending of the cantilever makes the position of the laser reflection change normally (up and down) on the photo-detector. The torsion of the cantilever makes the same laser spot to change laterally (left and right) on the photo-detector. Normal forces are measured by detecting the change of intensity difference between the upper and lower parts of the photo-detector ($\Delta[(A + B) - (C + D)]$). Lateral forces are measured by detecting the change of intensity difference between left and right parts ($\Delta[(A + C) - (B + D)]$).

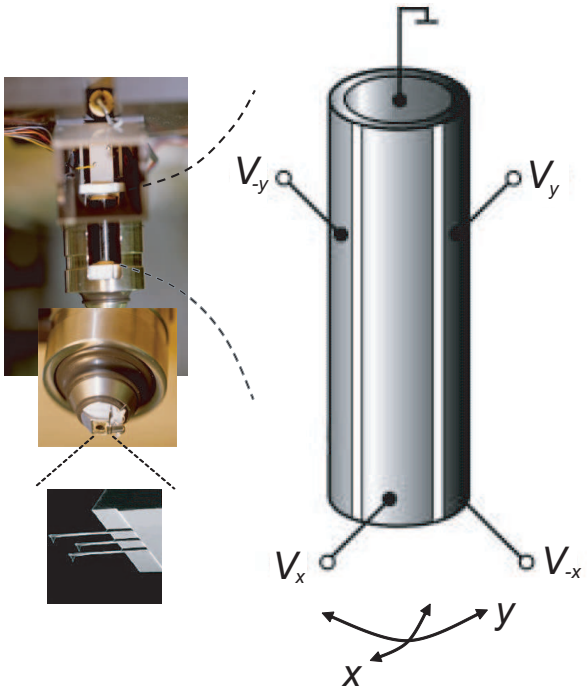

Figure 1.3.1: *The schematic of a piezo scanner tube used to drive the AFM tip in x- and y-direction. By applying a voltage to four individual ports of the tube, the tube can be manipulated to bend in x- and y-direction and to drive the tip mounted on it (not shown here). In our AFM, the z-position of the tip is manipulated by another separated piezo, which only deform in one direction (not shown here).*

1.3.1 Contact AFM

In contact AFM mode, also known as repulsive mode, an AFM tip makes soft "physical contact" with the sample. The tip is attached to the end of a cantilever with a low spring constant, lower than the effective spring constant holding the atoms of the sample together. As the piezo gently traces the tip across the sample (or the sample under the tip), the contact force causes the cantilever to bend to accommodate changes in topography. Or, a feedback loop maintains a constant bending/force on the sample by adjusting the height of the cantilever to compensate for topographical features.

When the tip is brought to within less than 10 nm of the sample surface , the resulting interacting forces can be represented by a Lennard - Jones intramolecular

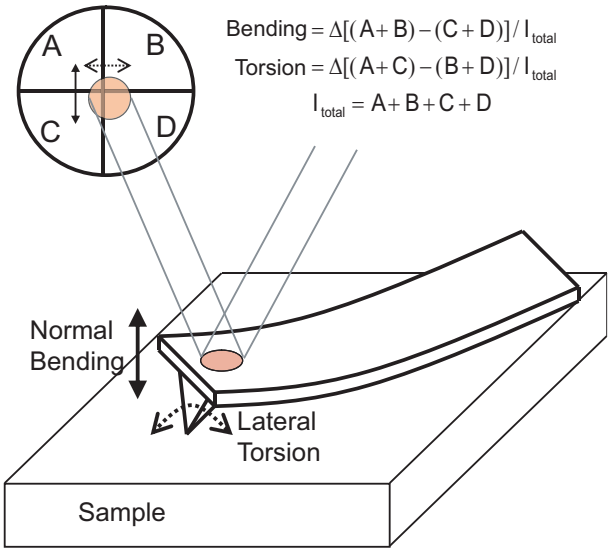

Figure 1.3.2: *In a typical AFM, a four-quadrant photo-detector is used to detect the bending and torsion of the cantilever to measure the normal and lateral forces.*

potential:

$$V(d) = \frac{\alpha}{d^{12}} - \frac{C}{d^6} \tag{1.3.1}$$

where d is the distance between molecules and α and C are constants. The behavior of the Lennard-Jones potential is shown in Fig. 1.3.3. The second term is the van der Waals energy (as shown in Fig. 1.1.1). The first term is repulsive and is the electrostatic repulsion felt by electrons in each molecule during orbital overlap. As the atoms are gradually brought together, they first weakly attract each other (vdW force). This attraction increases until the atoms are so close together that their electron clouds begin to repel each other electrostatically. This electrostatic repulsion progressively weakens the attractive force as the interatomic separation continues to decrease. The force goes to zero when the distance between the atoms reaches a couple of angstroms, about the length of a chemical bond.

The slope of the curve is very steep in the repulsive or contact regime. As a result, the repulsive force balances almost any force that attempts to push the atoms closer together. In AFM this means that when the cantilever pushes the tip against the

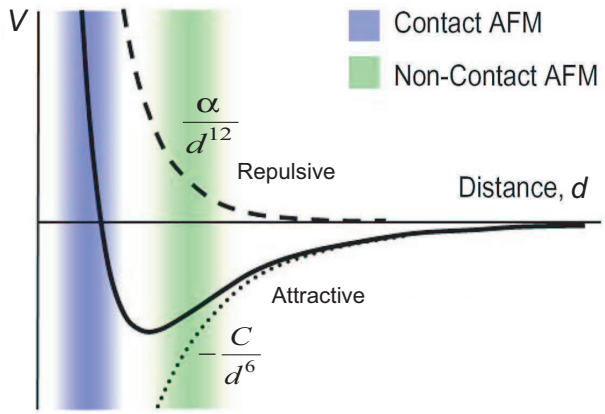

Figure 1.3.3: *The schematic of the Lennard-Jones potential. The α and C are constants. The attractive term is van der Waals potential, which is described in section 1.1.1.*

sample, the cantilever bends rather than forcing the tip atoms closer to the sample atoms. Even if you design a very stiff cantilever to exert large forces on the sample, the interatomic separation between the tip and sample atoms is unlikely to decrease much. Instead, the sample surface is likely to deform (nanoindentation).

In addition to the repulsive force described above, two other forces are generally present during contact AFM operation in air: a capillary force exerted by the thin water layer often present in an ambient environment, and the force exerted by the cantilever itself. The capillary force arises when water wicks its way around the tip, applying a strong attractive force (about 10^{-8} N) that holds the tip in contact with the surface. The magnitude of the capillary force depends upon the tip-to-sample separation. The force exerted by the cantilever is like the force of a compressed spring. The magnitude and sign (repulsive or attractive) of the cantilever force depends upon the deflection of the cantilever and upon its spring constant.

Most AFMs currently on the market detect the position of the cantilever with optical techniques. In the most common scheme, shown in Fig. 1.3.2, a laser beam bounces off the back of the cantilever onto a position-sensitive photo-detector (PSPD). As the cantilever bends, the position of the laser beam on the detector shifts. The

PSPD itself can measure displacements of light as small as 10 Å. The ratio of the path length between the cantilever and the detector to the length of the cantilever itself produces a mechanical amplification. As a result, the system can detect sub-angstrom vertical movement of the cantilever.

In standard contact mode AFM, the probe is scanned over the surface in an x-y raster pattern.

1.3.2 Tapping Mode, TM

Tapping Mode imaging is a key advance in atomic force microscopy (AFM) of soft, adhesive or fragile samples. This technique allows high resolution topographic imaging of sample surfaces that are easily damaged, loosely held to their substrate, or otherwise difficult to image by other AFM techniques. Specifically, Tapping Mode overcomes problems associated with friction, adhesion, electrostatic forces, and other difficulties that can plague conventional AFM scanning methods.

Tapping Mode imaging overcomes the limitations of the conventional scanning modes by alternately placing the tip in contact with the surface to provide high resolution and then lifting the tip off the surface to avoid dragging the tip across the surface. Tapping Mode imaging is implemented in ambient air by oscillating the cantilever assembly at or near the cantilever's resonant frequency using a piezoelectric crystal. The piezo motion causes the cantilever to oscillate with a high amplitude (the "free air" amplitude, typically greater than 20nm) when the tip is not in contact with the surface. The oscillating tip is then moved toward the surface until it begins to lightly touch, or "tap" the surface. During scanning, the vertically oscillating tip alternately contacts the surface and lifts off, generally at a frequency of 5 kHz to 500 kHz. As the oscillating cantilever begins to intermittently contact the surface, the cantilever oscillation is necessarily reduced due to energy loss caused by the interaction between the tip and surface see Fig. 1.3.4. The reduction in oscillation amplitude is

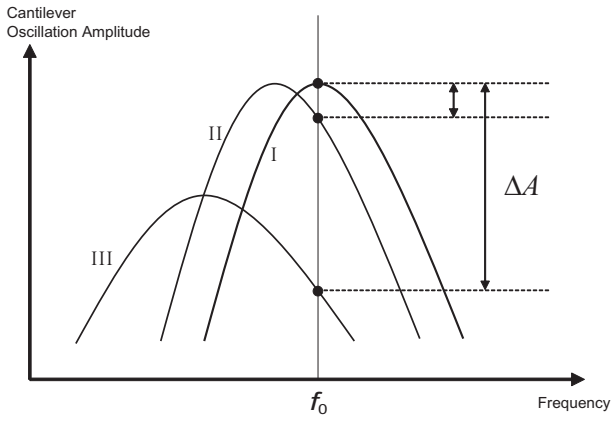

Figure 1.3.4: *The schematic of how the oscillation amplitude changes with shifted resonant frequency. When the tip is close enough to have interactions with the surface, the resonant frequency will shift from curve I to II and the amplitude of the oscillation at the free resonant frequency f_0 will decrease. For a case of even stronger interaction, the damping of the resonance comes in and decreases the amplitude more as shown by curve III.*

used to identify and measure surface features. During Tapping Mode operation, the cantilever oscillation amplitude is maintained constant by a feedback loop. When the tip passes over a bump in the surface, the tip has stronger interaction with the surface and the oscillation amplitude decreases. Conversely, when the tip passes over a depression, the tip has less interaction with the surface and the amplitude increases (approaching the maximum free air amplitude). The oscillation amplitude of the tip is measured by the detector and input to the controller electronics. The digital feedback loop then adjusts the tip-sample separation to maintain a constant amplitude and force on the sample.

1.3.3 Non-Contact Mode, NC-AFM

Non-Contact AFM (NC-AFM) is one of several vibrating cantilever techniques in which an AFM cantilever is vibrated near the surface of a sample. The spacing between the tip and the sample for NC-AFM is of the order of tens to hundreds of angstroms. This spacing range is the same as van der Waals interaction in Fig. 1.3.3

as the Non-Contact regime.

In contact mode, AFM measures surface topography by utilizing the systems sensitive response to the repulsive interactions in Eq. 1.3.1 that exist between the ion cores when the distance between the probe tip and the sample surface atoms is very small. However, the NC-AFM utilizes the attractive interaction regime of the Lennard-Jones potential, which is relatively larger distance than the one in contact mode. Because of the attractive force between the probe tip and the surface atoms, the cantilever vibration at its resonant frequency near the sample surface experiences a shift in spring constant from its intrinsic spring constant (k_0). This is called the effective spring constant (k_{eff}), and the following equation holds:

$$k_{eff} = k_0 - \frac{\partial F}{\partial d}. \tag{1.3.2}$$

When the attractive force is applied, k_{eff} becomes smaller than k_0 since the force gradient ($\frac{\partial F}{\partial d}$) is positive. According to the relation between the spring constant and resonant frequency, $f = \sqrt{\frac{k}{m}}$, the effective resonant frequency is shifting to lower as shown in Fig. 1.3.4. If we vibrate the cantilever at the frequency a little larger than the intrinsic resonant frequency where a steep slope is observed in the graph representing free space frequency vs. amplitude, the amplitude change ($\triangle A$) becomes very large even with a small change of intrinsic frequency caused by atomic attractions. Therefore, the measured amplitude change reflects the distance change between the tip and the surface atoms. By maintaining the amplitude constant with the feed back loop, the distance between the tip and sample will be constant. And the topography of the surface can be imaged by the voltage applied to z-scanner for compensating the feed back.

1.3.4 Lateral Force Microscopy

Lateral Force Microscopy (LFM) is an AFM technique that identifies and maps relative differences in surface frictional characteristics. It is particularly useful for differentiating among materials on surfaces. Applications include identifying transitions between different components in polymer blends, composites and other mixtures, identifying organic and other contaminants on surfaces.

The principle of LFM is the same as contact AFM, a feedback loop maintains a constant normal force on the sample by adjusting the height of the cantilever to compensate for topographical features. However in LFM, it records the torsion or twisting of the cantilever while scanning along the direction perpendicular to the cantilever length. The torsion, or twisting, of the cantilever supporting the probe will increase or decrease depending on the frictional characteristics of the surface (greater torsion results from increased friction). Since the laser detector has four quadrants, it can simultaneously measure and record topographic data, normal force, and lateral force data as shown in Fig. 1.3.2. All of these data sets can be viewed as side-by-side images in real time, as well as stored and processed independently.

1.3.5 Force-Distance Curves

Force-distance curves are used to measure the force normally acting on the tip while the tip approaches or retracts from the sample surface. In an elastic regime, the vertical forces between the tip and the surface (including adhesional forces) are proportional to the deflection $\triangle z$ of the cantilever $F = k_N \cdot \triangle z$, where k_N is the spring constant of the normal cantilever bending.

Strictly speaking, a force vs. distance curve is a plot of the deflection of the cantilever versus the extension of the piezo scanner, measured by a position-sensitive photo-detector. The method of how to convert the bending and the scanner extension

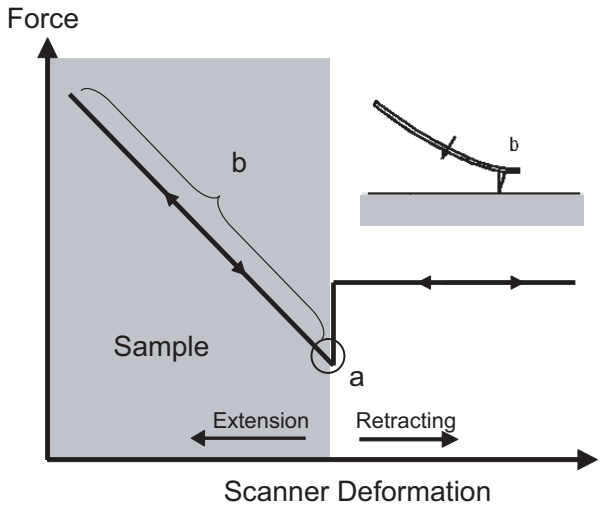

Figure 1.3.5: *The schematic of the force vs scanner deformation in vacuum.*

into normal force and tip-sample distance is described in 2.2.1 and 2.2.3. The discussion here refers to Fig. 1.3.5, 1.3.6, and 1.3.7 and represents a gross simplification, where shapes, sizes, and distances should not be taken literally.

Consider the simplest case of AFM in vacuum (Fig. 1.3.5), at the right side of the curve, the piezo scanner is fully retracted and the cantilever is undeflected since the tip is not touching the sample. As the piezo scanner extends, the cantilever remains undeflected until it comes close enough to the sample surface for the tip to experience the attractive van der Waals force. The tip snaps into the surface (point a in Fig. 1.3.5). Equivalently, the cantilever suddenly bends slightly towards the surface. (The physical reason of the cantilever not following the van der Waals force but snapping into the surface is described in 1.4.2). As the piezo continues to extend, the cantilever deflects, approximately linearly (region b in Fig. 1.3.5) and this deflection b_z is proportional to the normal force applied by the tip to the surface, $F_N = k_N \cdot b_z$. After full extension, at the extreme left of the plot, the piezo begins to retract. The cantilever deflection retraces the same curve (in the absence of piezo hysteresis) as the piezo pulls the tip away from the surface.

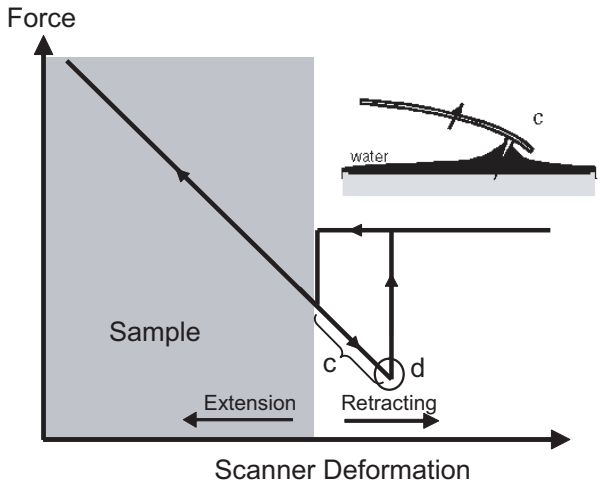

Figure 1.3.6: *The schematic of the force vs scanner deformation in air. The humidity in air forms a layer of water and causes the adhesion.*

In air, the retracting curve is often different because a monolayer or a few monolayers of water are present on many surfaces and because of the adhesional forces between the tip and the surface (Fig. 1.3.6). This water layer exerts a capillary force that is very strong and attractive. As the piezo pulls away from the surface, the water holds the tip in contact with the surface, bending the cantilever strongly towards the surface (region c Fig. 1.3.6). At some point, depending on the thickness of the water layer, the piezo retracts enough that the tip springs free (point d in Fig. 1.3.6). This is known as the snap-back point. As the piezo continues to retract beyond the snap-back point, the cantilever remains undeflected as the piezo moves it away from the surface in free space.

If a lubrication layer is present along with the water layer, multiple snap-back points can occur, as shown in Fig. 1.3.7.

1.3.6 AFM measurements of Solvation Forces in Liquids

By measuring force-distance curves, the forces between two surfaces (usually the AFM tip and the solid sample surface) in liquids can be measured to investigate how the liquid behaves under nano-confinements. Previous studies show that the oscillatory

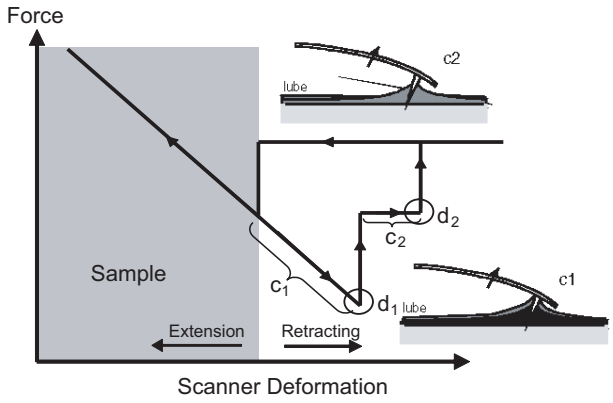

Figure 1.3.7: *The schematic of the force vs scanner deformation in air with impurities. There is one more step of the adhesion due to the lube on the water layer.*

solvation forces characterize the layered structure of many liquid molecules under nano-confinements, as shown in Fig. 1.3.8 [48]. Another way to measure tip-surface interactions is by applying normal oscillations with small amplitudes (~ 0.1 nm) and low frequency (several orders lower than the resonant frequency of the cantilever) to the cantilever. The stiffness of squalane ($C_{30}H_{50}$) [49] and water [50] can then be investigated by measuring the change of the cantilever amplitude and phase, see Fig. 1.3.9.

Frequency Modulated AFM (FM-AFM) Measurements

Frequency modulation atomic force microscopy (FM-AFM) is an alternative dynamic technique that employs a feedback circuit to self-excite the cantilever at its resonant frequency. The frequency can be measured with very high sensitivity and thus the frequency modulation mode allows for the use of very stiff cantilevers. Stiff cantilevers provide stability when the tip is very close to the surface and, as a result, this technique was the first AFM technique to provide true atomic resolution in ultra-high vacuum conditions [56]. Recently, FM-AFM was extended to measure the interaction forces in liquids [57]. The interaction force between tip and sample is detected as a change in resonant frequency, while the presence of dissipative forces can

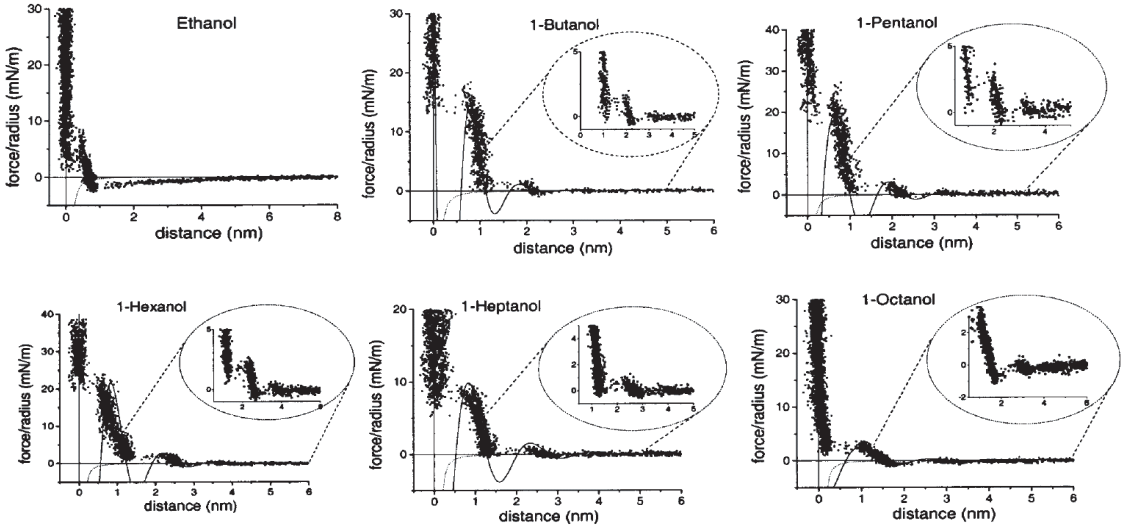

Figure 1.3.8: *The oscillatory structural normal force for different liquids measured by AFM. Picture from [48].*

be detected by monitoring the change in excitation required to keep the tip amplitude constant during the interaction. By means of this method, Uchihashi et al. [58] have studied the solvation forces between an AFM tip and a graphite surface in OMCTS (Fig. 1.3.10).

The FM-AFM has some unique advantages in force measurements, such as better noise-to-signal ratio and no jump-to-contact instability. However, there are some disabilities, which have to be pointed out here:

1. Since the oscillatory solvation force comes from the local organization of the liquid molecules, there is a doubt that the oscillatory solvation force is still the same when the applied normal oscillation (~ 2 nm) is equal or larger than the dimension of the liquid molecular size ($\sim 0.2 - 1$ nm).

2. The force is not directly measured from the AFM force measurement. Instead, the interacting force is deduced from a non-trivial mathematical calculation with approximations.

3. It has no capability to measure the interacting lateral force.

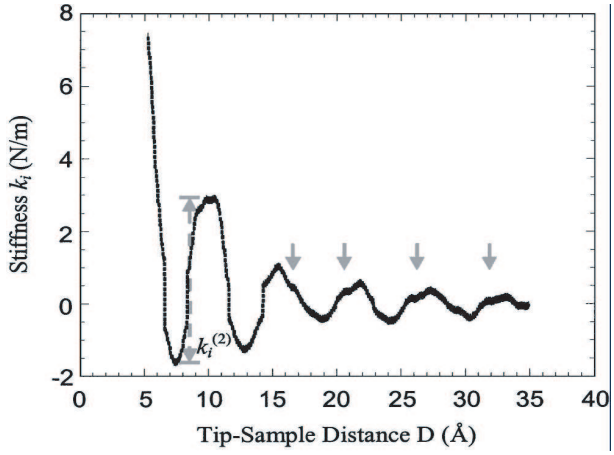

Figure 1.3.9: *The stiffness of squalane vs distance under nano-confinement. It is measured by applying a external normal oscillation to the cantilever and detecting the change of the cantilever amplitude. Picture from [49].*

1.4 Surface Force Measurements: Other Methods

1.4.1 Surface Force Apparatus

The surface force apparatus is a wildly used instrument to study surface forces between two surfaces separated by gaps in the range between 100 μm and 1 Å. It was initially invented by Tabor and Winterton [51] and then extensively modified by Israelachvili and Adams [52] for measurements in liquids. Figure 1.4.1 shows the schematic of a Mark II model SFA. The SFA contains two curved molecularly smooth mica surface (of curve radius $R \approx 1$ cm) between which the interaction forces are measured using interchangeable springs. The resolution of the force measurement is about 10 nN. The two mica surfaces are in a crossed cylinder configuration. The separation of the two mica surfaces can be measured by use of an optical technique called Fringes of Equal Chromatic Order (FECO), which gives the SFA a distance resolution about 0.1 nm. By acquiring the separation and forces simultaneously, the force-distance curve is measured.

With the extremely high distance-resolution, the first oscillatory solvation force was demonstrated by Horn et al [53], as shown in Fig. 1.4.2. Also, the increase

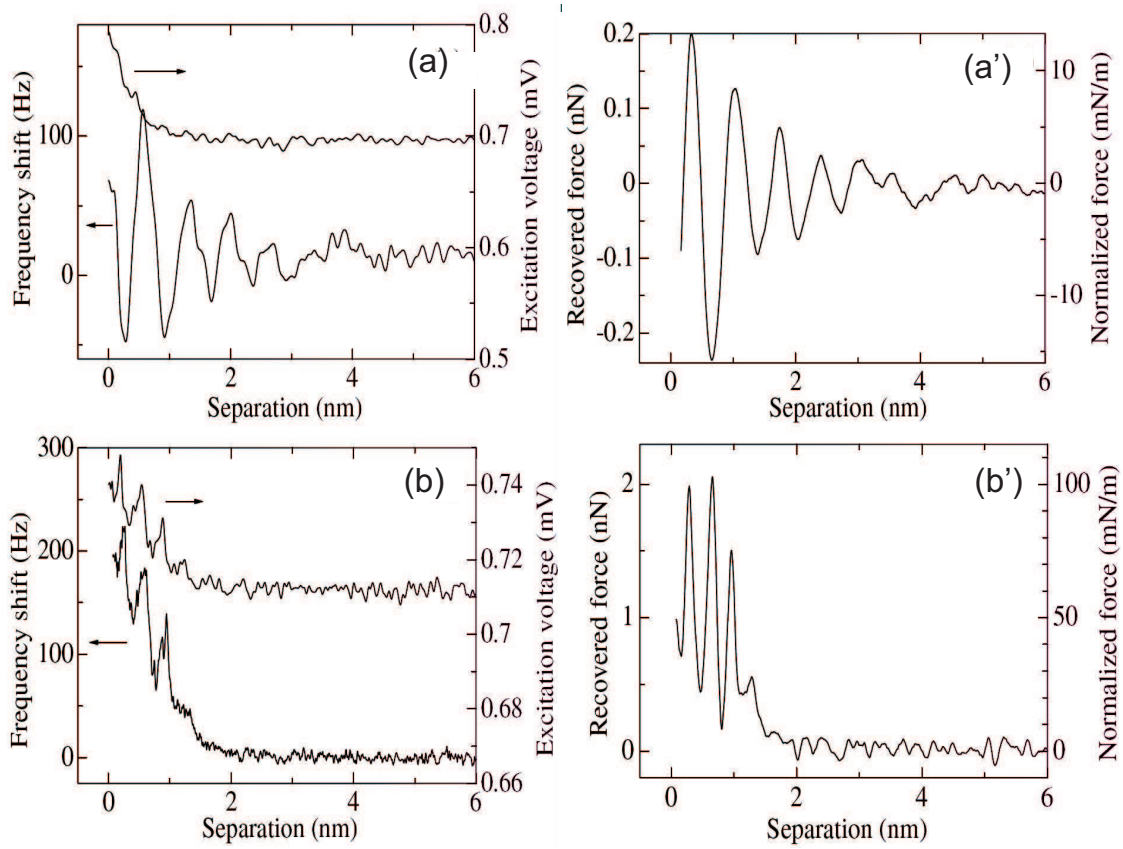

Figure 1.3.10: *The oscillatory solvation force measured by FM-AFM technique [58]. (a) and (b) are the frequency shift of the cantilever with OMCTS and water. (a') and (b') are the interacting forces deduced from (a) and (b). Picture from [58].*

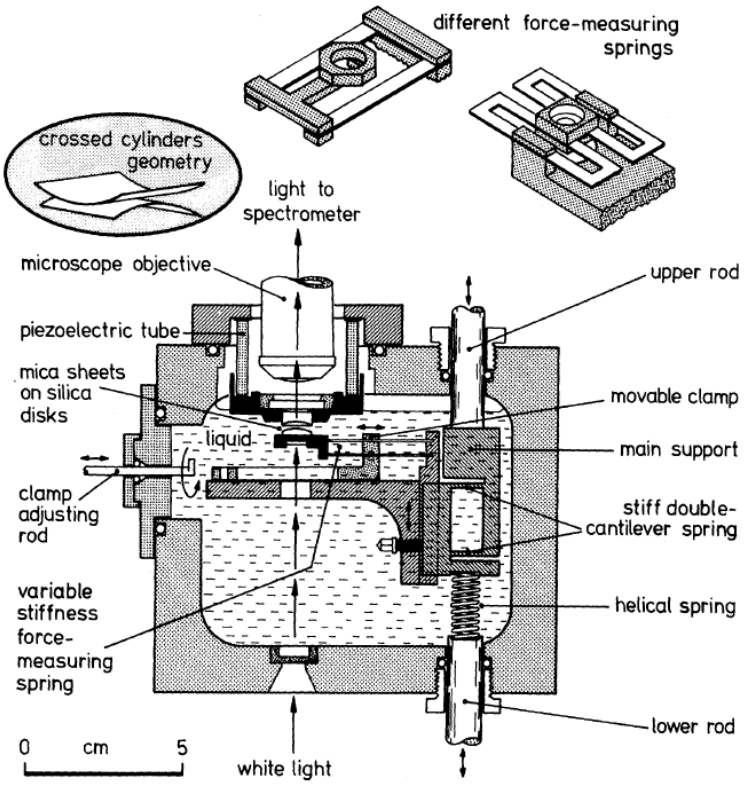

Figure 1.4.1: *Surface force apparatus (SFA) for directly measuring the force laws between surfaces in liquids or vapors at the angstrom resolution level. Picture from. [55]*

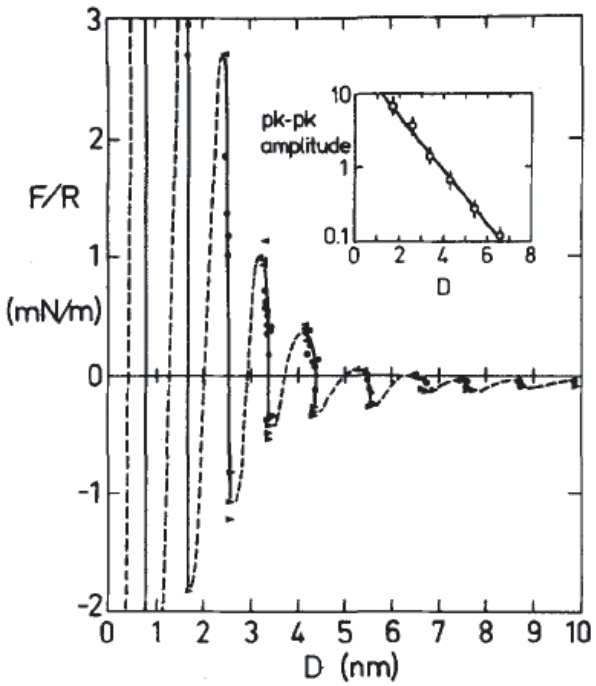

Figure 1.4.2: *The first observed oscillatory solvation force in liquids (OMCTS) by the SFA. The reason of no measuring of the dashed regimes is described in section 1.4.2. Picture from [53].*

of magnitudes of the viscosity of OMCTS under nano-confinement was observed by shearing the mica surface and measuring the lateral viscous force with a SFA [**?**]. So far, the SFA is one of the most wildly used tools for studying surface forces in liquids.

1.4.2 Comparison between SFA and AFM

The concepts behind AFM and SFA force measurements are straightforward and simple, however there is a major disadvantage for both of them: during the approaching/retracting, the tip jumps off the true force-distance curve when the gradient of the curve exceeds the spring constant of the apparatus (cantilever for AFM), k_N, i.e., $|\frac{\partial F}{\partial d}| \geq k_N$ [49, 54] (see Fig 1.4.3). It is a common disadvantage for all spring-based force measurements. Therefore, to minimize this mechanical instability in different force measurements, selecting a proper spring constant is crucial.

Although AFM and SFA have the same capabilities on direct force measuring, it

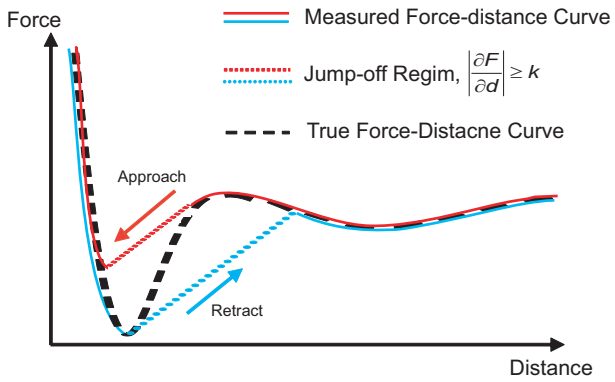

Figure 1.4.3: *The schematic of a typical force-distance measurement by spring-based methods, e.g., SFA and AFM. When the gradient of the true force-distance curve exceeds the spring constant ($|\frac{\partial F}{\partial d}| \geq k_N$), the measurement jumps off the real force curve and follows $|\frac{\partial F}{\partial d}| = k_N$.*

is useful to point out several main differences that matter in our experiments:

1. Because of the usage of FECO, all the materials on the light path have to be optical transparent, which limits the choice of the sample and substrate.

2. SFA needs molecularly smooth samples, thus it works best with mica surfaces or thin layers deposited on thin mica sheets.

3. AFM is less subject to contamination due to the orders of magnitude smaller interacting area.

4. SFA can not characterize indentation and topography.

1.4.3 Interfacial Force Microscopy, IFM

The interfacial force microscopy (IFM) is designed to avoid the mechanical instability problem mentioned in section 1.4.2 and allow quantitative measurements of normal and lateral (shear) forces throughout the entire range of interfacial separation [59]. The IFM sensor consists of a capacitor common plate suspended above two individual capacitor pads by torsion bars bisecting the long axis, as illustrated schematically in Fig 1.4.4. A tip is placed on one side of this teeter totter such that when a

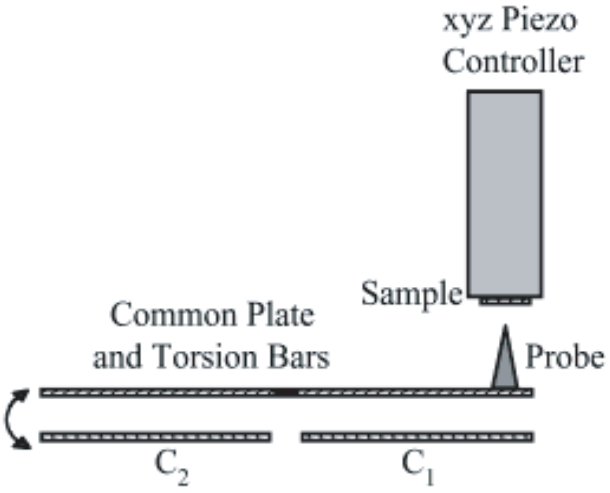

Figure 1.4.4: *Schematic of the differential-capacitor IFM forcefeedback sensor. The common plate supports the probe tip and is suspended above two capacitor pads by torsion bars going in and out of the page. Interactions between the tip and sample rotate the top plate, which is detected by an RF bridge. Low-frequency voltages are then supplied to the capacitor pads by a controller to maintain capacitor balance. Picture from [59].*

force is applied to the tip, arising from the interaction with a neighboring sample surface, the teeter totter will rotate about the torsion bars imbalancing the differential capacitance. The deflection is measured by an RF bridge circuit, and the resulting signal is fed to a controller which applies the appropriate dc voltages to the capacitor pads to rebalance the deflection. The result is that voltages appear at the controller output related to the level of applied force without sensor motion. The relationship between the voltage and force is dependent only on the capacitor geometry and is easily calibrated. In addition, the force-feedback sensor will balance any force applied to the tip which produces a torque about the torsion-bar axis, and it is this fact that is the basis for making lateral-force measurements in the friction mode.

By means of IFM techniques, Major et al. [61] showed that the shear viscosity of water, for 0.6 nm hydrophilic confinements, is 7 orders of magnitude higher than the bulk water viscosity.

1.4.4 Transverse Dynamic Force Microscopy, TDFM

The transverse dynamic force microscopy (TDFM) is also designed to measure the surface forces without the mechanical instability mentioned in section 1.3 [60]. In TDFM a tapered optical fiber is mounted vertically and perpendicularly to the sample surface and set in horizontal oscillation using a dither piezo. The oscillation amplitude and the corresponding phase signal are quantitatively measured with an optical detection system. The tapered probe is obtained by pulling and fracturing an optical fiber heated in the beam of a CO_2 laser. This technique produces a flat circular end with $\sim$ 50 nm radius. A known sinusoidal shear strain is imposed on the confined fluid and the corresponding stress response is evaluated. Figure 1.4.5 shows all the important elements involved in a typical force spectroscopy experiment. A sinusoidal displacement ($d_0 sin(\omega t)$) is applied at the top end of the probe. The corresponding oscillation amplitude and phase ($u_0 sin(\omega t + \phi)$) are recorded at the lower end. By detecting the damping of the amplitude and change in phase, the viscous and elastic forces are deduced. Thereby, the shear viscosity and rigidity of nano-confined water are extracted, see Fig. 1.4.6

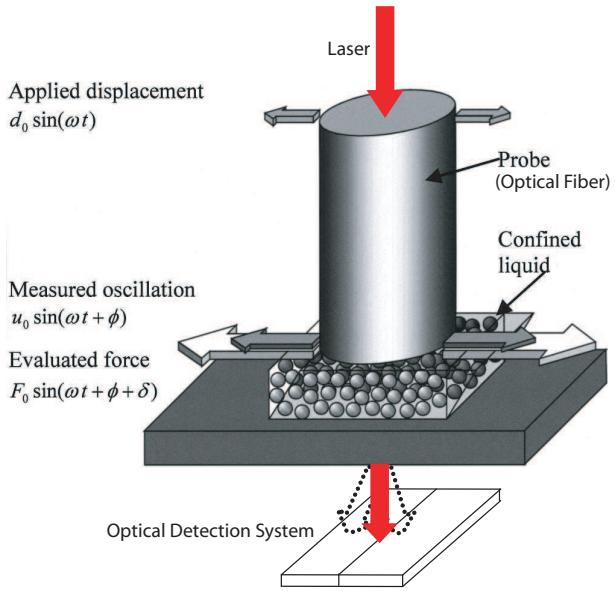

Figure 1.4.5: *The schematic of TDFM. Picture from [60].*

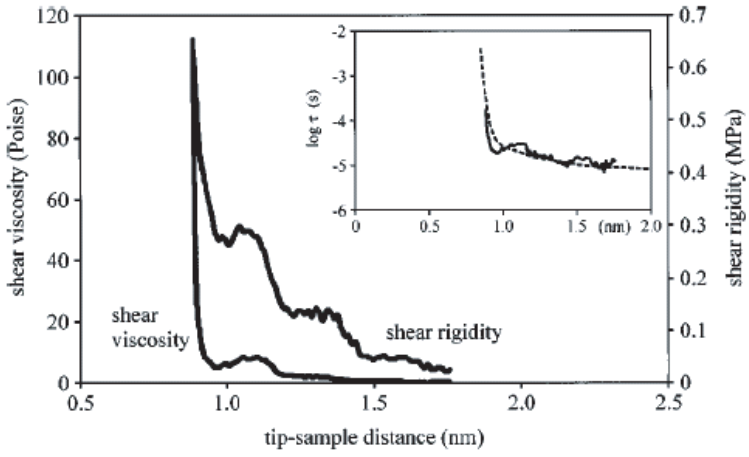

Figure 1.4.6: *The viscosity and rigidity of nano-confined water obtained by TDFM techniques. Picture from [60].*

CHAPTER II

MATERIALS AND METHODS

This chapter will describe the details of the AFM experiments presented in this thesis. The goal of this work is centered on the behavior of liquids confined between an AFM tip and a solid surface. The first half of this chapter is focused on the preparation and properties of the materials used in our experiments. In the second half of this chapter, we will present the details of how forces were measured and calibrated in our AFM experiments.

2.1 Liquids and Surfaces Preparation

2.1.1 Liquids

Water

The water used in this experiment is deionized ultra-filtered (DIUF) water purchased from Fisher Scientific. Due to the water's exposure to the atmosphere, it has dissolved CO_2, some of them reacts with water to form carbonic acid, which lowers the pH value to 6.1 instead of the expected 7. Previous studies show that a mica surface (we mainly used in our experiments) immersed in water is negatively charged due to the dissolved K^+ ion [62]. In our experimental setup, a liquid cell is used to contain the fluids. The liquid cell is composed of rubber and teflon, which may dissolve in water, therefore it is necessary to check for impurities on the mica surface and/or in water. For the investigation of impurities on the mica surface, the contact angle measurement was chosen because of its simplicity. Contact angle (θ_c) measurements of water were performed on a (i) freshly cleaved mica surface, (ii) mica surface left to evaporate the water used in our experiment, and (iii) mica surface where the

water used in the experiments was gently poured out of the liquid cell. If there were impurities, all of them should have been left on the mica surface in (ii). Only surface-active impurities could have remained on the mica surface in (iii). The first and third measurements gave the same θ_c, while in the second measurement indicated an increase in θ_c. These results suggest the presence of impurities in the experimental water, but the impurities were not surface-active. Conductivity measurements were performed, indicating an impurity concentration of 1.3×10^{-5} mole/l. Considering the volume of interest is defined by the confined space between the AFM tip and the mica surface, i.e. about 120 nm^3 for d=2 nm in Fig. 0.0.1, there were only 10^{-3} impurity molecules in the confined region .

The impurities were also tested by gas chromatography - mass spectrometry (GC-MS). GC-MS spectra of used and not previously used water samples were taken by 70SE spectrometry (VG Instruments). In both cases the results conveyed that any small molecular weight (less than 700 Da) organic contaminants were present at amounts below the instrumental threshold (5 ppm).

Before and after each measurement, AFM topography and friction images of the mica surface were taken to avoid any contaminated and/or inhomogeneous area, which could be detected by AFM images.

OMCTS

Octamethylcycloterasiloxane (OMCTS, $C_8H_{24}O_4Si_4$) is a kind of silicon oil used in waterproofing agent and lubricant for vacuum devices. Rheological properties of OMCTS are widely studied under nano-confinement [53, **?**, 63] because OMCTS has a spherical molecular shape, large molecular size (about $7 - 9$ Å), and is non-polar. Unlike water, it is stable on mica, rubber, and teflon, thus, the mica surface is not charged in OMCTS and presents no impurities. OMCTS wets the mica surface, as the contact angle of OMCTS on mica is less than 10^o. However OMCTS is sensitive

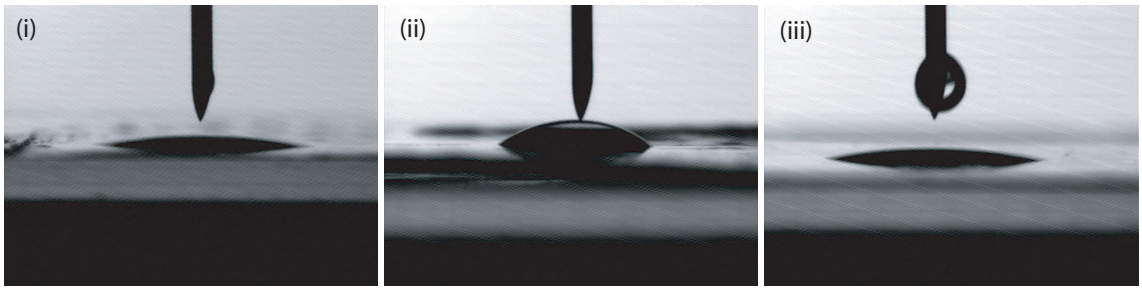

Figure 2.1.1: *Contact angle measurements of water on mica surface. (i) Water contact angle on freshly cleaved mica surface. (ii) Water contact angle on mica surface which has been left to evaporate all the water used in the experiment. (iii) Water contact angle on mica surface where the water used in the experiments was gently poured out. The contact in (i) and (iii) are the same, which means that the water used in our experiment does have some contaminations which are not mica surface active.*

to moisture, so high purity nitrogen was used to gently flush the AFM chamber to minimize the humidity of the experiment. The OMCTS used in our experiments was purchased from Fluka, purity $\geq 99.0\%$.

2.1.2 Surfaces

Mica

Because of the atomically smooth surface and simple preparation, mica has been used for AFM calibration for more than two decades. The most widely used mica is muscovite mica, which is a phyllosilicate mineral of aluminium and potassium with the following molecular formula: $KAl_2(AlSi_3O_10)(F,OH)_2$. It has a highly perfect basal cleavage yielding remarkably thin laminae (sheets), which are often highly elastic. It has a layer-like structure of aluminum silicate sheets not strongly bonded, are held together by the K^+ ions. Before use, the mica surface was refreshed by peeling some layers with scotch tape, followed by an immediate immersion in the fluid contained by the AFM liquid cell (see Fig. 2.1.3).

HOPG

Highly Oriented Pyrolytic Graphite (HOPG) is a highly ordered form of pyrolytic graphite with an angular spread of the c axes of less than 1 degree. It is also commonly used as a calibration tool for probe microscopies such as Scanning Tunnelling Microscopy or Atomic Force Microscopy due to the atomically smooth surface. HOPG has also a layered structure and the same method for refreshing the mica surface is also used on the HOPG surface in experimental preparation. The HOPG sample used in this experiment was purchased from SPI supplies (HOPG SPI-2 grade, $20 \times 20 \times 1$ mm).

Glass

The third sample surface used in this experiment is glass (Fisherbrand Microscope Slides). Before use, the glass slide was cut into squares roughly 2×2 cm^2 with thickness of 1 mm and cleaned with the same method used to clean liquid cell (see 2.1.3).

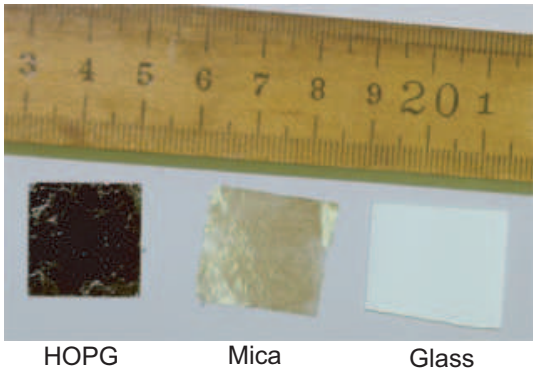

Figure 2.1.2: *Solid surface samples used in this thesis.*

2.1.3 Liquid Cell and Experimental Setup Preparation

To measure forces in liquids, a liquid cell must be used to contain the liquid on the solid sample surface. The cross-section schematic of the liquid cell for the AFM (PicoPlus SPMII) is explained in detail in Fig. 2.1.3. The liquid cell is clamped by a

[H]

Table 2.1.1: Comparison of the hydrophobicity and roughness of mica, HOPG, and glass.

Mica	Glass	HOPG
atomically smooth hydrophilic	nanometer-roughness hydrophilic	atomically smooth hydrophobic

spring used to secure it on the sample stage. A rubber o-ring is clamped in between the liquid cell and sample surface to prevent leakage. The retaining clip is used to support the compressed spring by inserting into a track on the retaining rod which one end of the spring is fixed on. During the experiment, the scanner-driven nose bearing the cantilever and tip is immersed in the liquid in liquid cell.

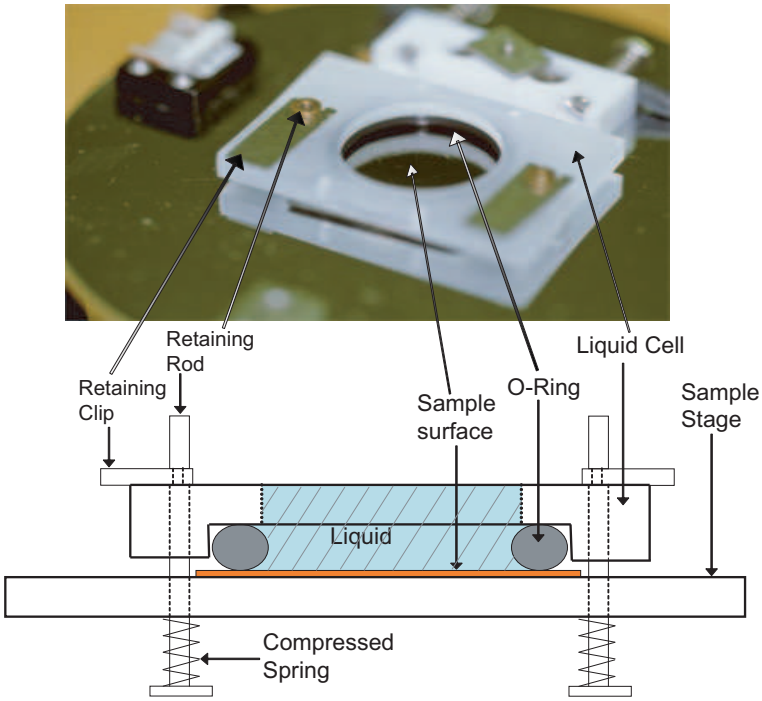

Figure 2.1.3: *Schematic of the liquid cell used in this experiment.*

Experiments performed at the nanometer scale are extremely sensitive to impurities. Therefore, all the parts that will contact to the liquid or sample surface (e.g., liquid cell, o-ring, retaining clips, AFM nose, tweezers used for mounting tips and

samples, or glass samples) were cleaned by the following procedure:

1. Sonicated in laboratory detergent for 30 mins.

2. Rinsed with water to remove the residual of the detergent.

3. Blew dry under N_2 or Ar gas.

4. Rinsed with isopropyl alcohol and wiped with clean gloves or clean wipes.

5. Sonicated in fresh isopropyl alcohol for 30 mins.

6. Blew dry under N_2 or Ar gas.

7. Repeated step 5 and 6 by replacing isopropyl alcohol with ethanol.

Even after the cleaning, impurities could have been presented in the liquid for the experiment, however they are not surface-active and had no influence on the experiment, as described in 2.1.1.

2.2 Force Measurements by AFM

In our AFM experiments [10], a nano-size spherical silicon tip is brought quasi-statically to the vicinity of a flat sample surface, all immersed in purified water or OMCTS, while small lateral oscillations are applied to the cantilever support. Lateral forces acting on the tip provide the cantilever with a torque, and the torsion of the cantilever starts to oscillate due to oscillation of the tip. By monitoring the amplitude of the torsion, the lateral force acting on the tip can be measured. The normal and lateral forces acting on the tip are measured directly and simultaneously as a function of the liquid film thickness, i.e., tip-sample distance, d. The zero distance, $d = 0$, is evaluated by comparison of the normal force vs. d curves with contact mechanics models (discussed in 2.2.3).

The experiments were performed with a Molecular Imaging PicoPlus AFM. We used silicon tips with radii $R = 40 \pm 10$ nm and Ultrasharp NSC12/50 cantilevers

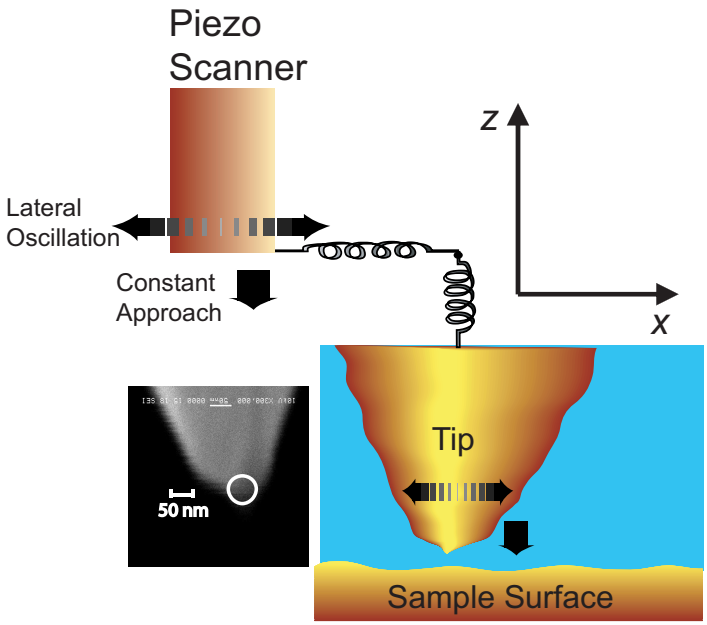

Figure 2.2.1: *Setup for AFM force measurements. A piezo scanner is used to drive the cantilever (not shown in the figure) and the tip on the cantilever. The tip is driven to constantly approach the sample surface and is also laterally oscillated by the piezo scanner. Both the tip and sample surface are immersed in liquids.*

with normal and lateral spring constants in the ranges of $k_N = 3 - 4.5$ N/m and $k_L = 50 - 120$ N/m, respectively. Before use in our experiments, all of the tips were imaged by a scanning electron microscope (SEM), JEOL JSM-5910, to make sure that the AFM tips apex is spherical and to measure the precise geometry of individual cantilevers for force constant calibrations. The apex spherical tips might not be atomically smooth; however the lateral force-distance curve was found to be reproducible for different tips. The approach velocity was 0.2 nm/s . During the approach, lateral oscillations parallel to the sample surface were applied to the cantilever holder by means of a lock-in amplifier. The same lock-in amplifier was then used to measure the amplitude of the lateral force, F_L, and the phase difference, θ, between the applied lateral displacement and the detected lateral force. The $\theta = 0$ was chosen when the tip was in hard contact with the mica surface, for lateral oscillation amplitudes, X_0 is small enough to guarantee an elastic contact without slippage [64].

2.2.1 Normal Force Measurements

To measure the normal force-distance curve, the tip is driven by the scanner piezo in z-direction. The cantilever does not bend until the normal forces have been acted to the tip. By acquiring the information of the scanner deformation and the bending of the cantilever, the normal force and the distance between tip and sample surface is extracted.

In an ideal situation with no interaction other than contact, the cantilever would not bend before contact, regime I in Fig. 2.2.2, i.e., the tip totally follows the scanner deformation toward the sample surface. However, once the tip is in contact with the surface, the tip can not follow the deformation to 'approach' anymore, as there is no more space for approaching. Therefore, the cantilever starts to bend due to the 'extra' displacement driven by the scanner. In a perfect hard contact case (no deformation of the tip and sample surface), the amount of bending is equivalent to the amount of scanner deformation, as shown in regime II of Fig. 2.2.2, i.e., all the scanner deformation contributes to the cantilever bending.

For small bending, the relation between the normal force (F_N) acting on the tip/cantilever and the bending (δX) follows Hook's law, $F_N = \delta X \cdot k_N$, where k_N is the force constant of bending. The distance between the tip and sample surface is the scanner deformation minus the bending. The corresponding normal force-distance curve is in Fig. 2.2.3.

Normal Force Calibration

For the normal force calibration, both the bending (δX) and the normal force constant (k_N) must be calibrated. In the AFM experiment, bending of the cantilever is detected by monitoring the normal position change of the laser spot reflected from the back of the cantilever, as shown in Fig. 1.3.2. The pre-amplified coefficient used to

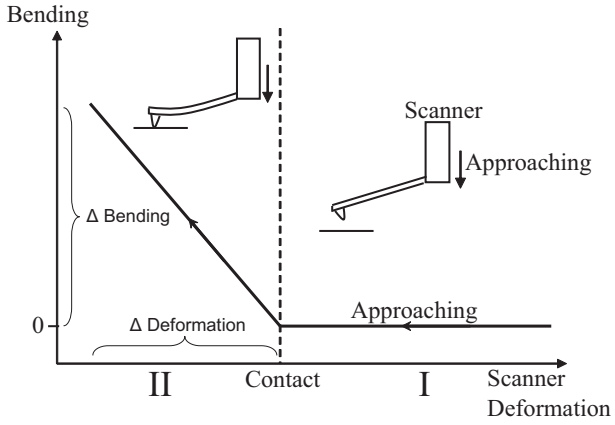

Figure 2.2.2: *A typical bending vs scanner deformation curve without any interaction other than the perfect hard contact. In regime I, the tip doesn't contact the surface, thus there is no normal force acting to the tip, and the bending of the cantilever is zero. In regime II, the tip is in hard contact with the surface, normal force acting to the tip, and the bending proportionally increases with the scanner deformation. The* $\Delta Bending$ *equals to* $\Delta deformation$ *after calibrated the pre-amplified coefficient between the bending signal detected in voltage and in nanometer.*

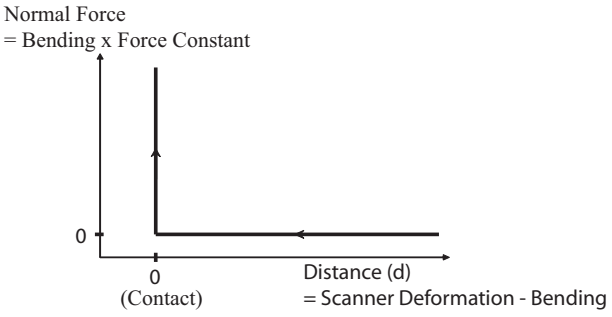

Figure 2.2.3: *Typical normal Force-distance curve deduced from Fig. 2.2.2. The regime II in Fig. 2.2.2 is deduced to a vertical line, contact point.*

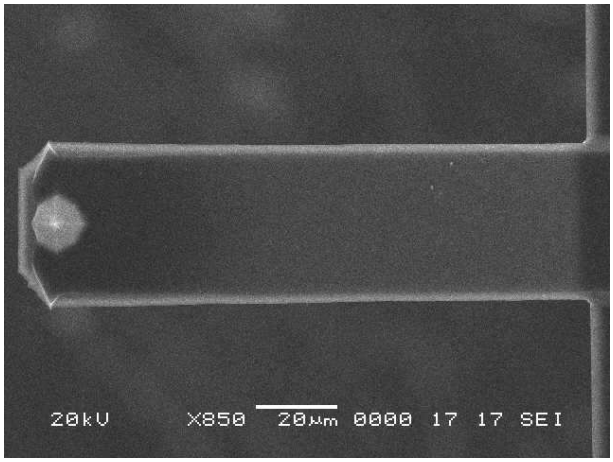

Figure 2.2.4: *A SEM image of the cantilever shows the length, L, and the width, w. They are the essential values in the force constant calibration, Eq. 2.2.1 and 2.2.3.*

convert bending in unit of volts to nanometer has to be calibrated before every measurement. Since the bending and scanner deformation should be equal in hard contact, the coefficient can be easily adjusted until the slope of the bending-deformation curve equals to -1 in the contact regime, as illustrated Fig. 2.2.2.

The normal force constant is a function of the cantilever geometry and elastic Young's modulus, E, [65]:

$$k_N = \frac{E}{4}\frac{wt^3}{L^3} \tag{2.2.1}$$

where L, w, and t are the length, width, and thickness of the cantilever respectively. All the geometrical parameters are conveyed in the SEM image taken before the use of a new tip/cantilever, as shown in Fig. 2.2.4. By comparing the values provided by the manufacturer and the SEM image, k_N for individual cantilevers can be extracted without measuring the elastic Young's modulus.

2.2.2 Lateral Force Measurements

For a rectangular cantilever, a lateral force acting on the tip will cause three different kinds of elastic deformation: bending of the tip, lateral bending of the cantilever, and torsion of the cantilever, as illustrated in Fig. 2.2.5. For measuring the lateral

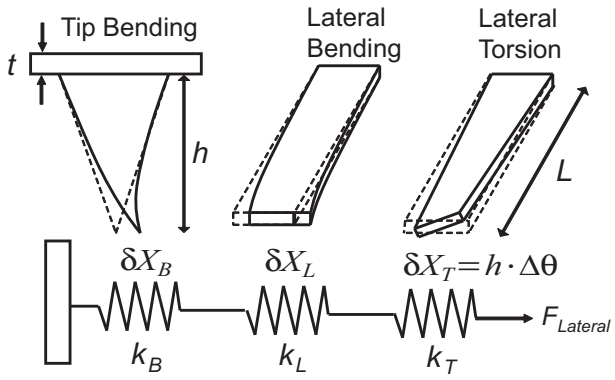

Figure 2.2.5: *The total displacement in lateral direction for lateral force measurements is contributed by three independent parts: tip bending, lateral cantilever bending, and cantilever torsion. The lateral elastic contact deformation is not considered here due to the much higher force constant. It can be considered as three different springs (k_B, k_L, and k_T) in series, and the lateral force can be written as $F_L = k_B \cdot \delta X_B = k_L \cdot \delta X_B = k_T \cdot \delta X_T$, where δX_B, δX_L, and δX_T are the corresponding displacement for each part. For generalizing the lateral force calibration to different type of cantilevers, the torsion displacement is written as $\delta X_T = h\Delta\theta$, thus the calibration of θ can be applied to different cantilevers with different tip hight, h.*

force, $F_L = k_B \cdot \delta X_B = k_L \cdot \delta X_L = k_T \cdot \delta X_T$, only one of the spring constants and its corresponding displacement are needed. For AFM techniques, the lateral force is detected by monitoring the lateral change of the laser spot reflected from the back of the cantilever, which is the only contributed by the torsion of the cantilever, as shown in Fig. 1.3.2 and Fig. 2.2.5. In our experiments, a lock-in amplifier (SRS830) is used to apply a sinusoidal signal to the piezo scanner in x-direction to oscillate the tip laterally. Once the tip apex has lateral interactions with the surrounding material, the cantilever is going to torque back and forth accordingly to the oscillation. Due to the oscillation of the torsion, the photo-detector generates an oscillating electric signal accordingly. The same lock-in amplifier is used to monitor the amplitude of this oscillation, which can be converted to the amplitude of cantilever torsion. With proper calibrations, the amplitude of the torsion can be converted to the lateral force acting to the tip, Fig. 2.2.6.

Lateral Force Calibration

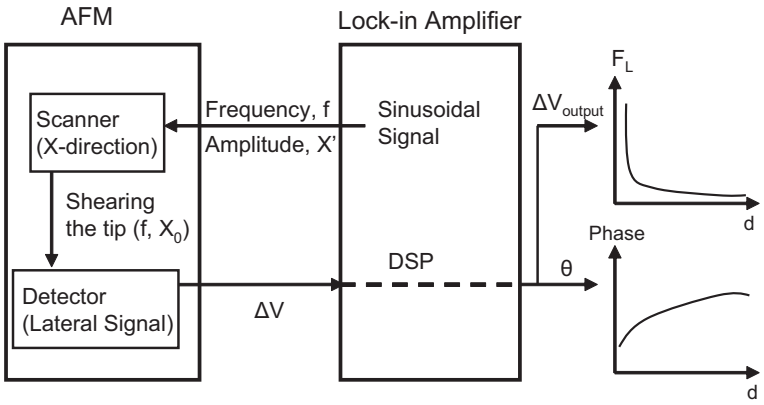

Figure 2.2.6: *Setup of the lateral force measurement. A lock-ing amplifier is used to oscillate the scanner piezo in x-direction to shear the tip laterally. The same lock-in amplifier is also used to detect the amplitude of the torsion due to the lateral force. After calibrating, the lateral signal in volts can be converted to lateral force in nano-Newtons. The θ is the phase difference between the oscillating signal applied to the scanner and the torsion oscillation detected. The amplitude applied to the scanner X' is not necessary the same as the lateral amplitude of the tip, X_0, due to the resonant effect, which is calibrated in 2.2.6.*

The lateral force acting on the tip can be extracted by:

$$F_L = K_T \cdot \delta X_T = K_T \cdot h\Delta\theta \tag{2.2.2}$$

where the X_T is the displacement due to the torsion only, h is the height of the tip, and $\Delta\theta$ is the torqued angle, as seen in Fig. 2.2.5. For the lateral force detection, the lateral change of the laser reflected spot (corrected to the cantilever torsion) is detected, and what we applied is the shearing amplitude and frequency. Unfortunately, the shear amplitude is not the same as X_T here; for a non-slippage friction, it is the total displacement of the tip bending, cantilever lateral bending, and cantilever torsion ($\delta X = \delta X_B + \delta X_L + \delta X_T$). Therefore to calibrate lateral force, the δX_T in terms of δX and the coefficient used to convert the lateral signal in voltage to lateral displacement in nanometers are needed.

In order to eliminate the unknown factors, a silicon nitride tip (B, MLCT-NOHW, Veeco Nanoprobe Tips) with a large apex angle (70 degree) was used to avoid the tip bending term in Fig. 2.2.5, which is difficult to calibrate. By imaging the rectangular

cantilever with the SEM, the spring constant of lateral cantilever bending and torsion can be extracted by [65]:

$$k_T = 0.4k_N \frac{L^2}{(H + \frac{t}{2})^2} \tag{2.2.3}$$

$$k_L = k_N \frac{w^2}{t^2} \tag{2.2.4}$$

where L, w, and t are the length, width, and thickness of the cantilever. For this particular cantilever, k_T is 28 m/N and k_L is 14 m/N. Since the tip bending can be neglected, the torsion displacement is 1/3 of the total displacement, $\delta X_T = 1/3\delta X$.

For calibrating the coefficient between the lateral signal in voltage and the lateral displacement in nanometers, the same silicon nitride tip is used to scan a friction image on silicon surface in contact mode. In the cross-section curve of the friction images forward and backward in Fig. 2.2.7, only the circled linear segments were used for calibrating the coefficient because only these parts of the curve are non-slippage cases, i.e., the total cantilever displacement (δX) is the same as the scanner displacement (ΔX). The slope of these linear segments is the coefficient. The average value of the coefficient between the lateral signal change (ΔV) and the total cantilever displacement (δX) is $\frac{\Delta V}{\delta X} = 0.083\ (\frac{V}{\mathring{A}})$ (averaged over 30 different segments). Therefore, the coefficient between the lateral signal and torsion displacement (X_L) is $\frac{\Delta V}{\delta X_L} = 0.25(\frac{V}{\mathring{A}}) = \frac{\Delta V}{h_0 \Delta\theta}$, where h_0 is the height of the tip ($h_0 \cong 3\ \mu$m). Ultimately, the relation between the torqued angle and the lateral signal can be presented as

$$\Delta\theta = \frac{\Delta V}{7.5 \times 10^3}. \tag{2.2.5}$$

In our AFM, Eq. 2.2.5 is universal for rectangular cantilevers.

By combining Eq. 2.2.3, 2.2.2 and 2.2.5, the lateral force can be deduced to

$$F_L = (0.4k_N \cdot \frac{L^2}{(h + \frac{t}{2})^2}) \cdot (\frac{h\Delta V}{7.5 \times 10^3}) \tag{2.2.6}$$

where ΔV is the lateral change of the reflected laser spot on the photo-detector, i.e., the $\Delta[(A + C) - (B + D)]$ in Fig. 1.3.2. Apparently, ΔV is proportional to the total

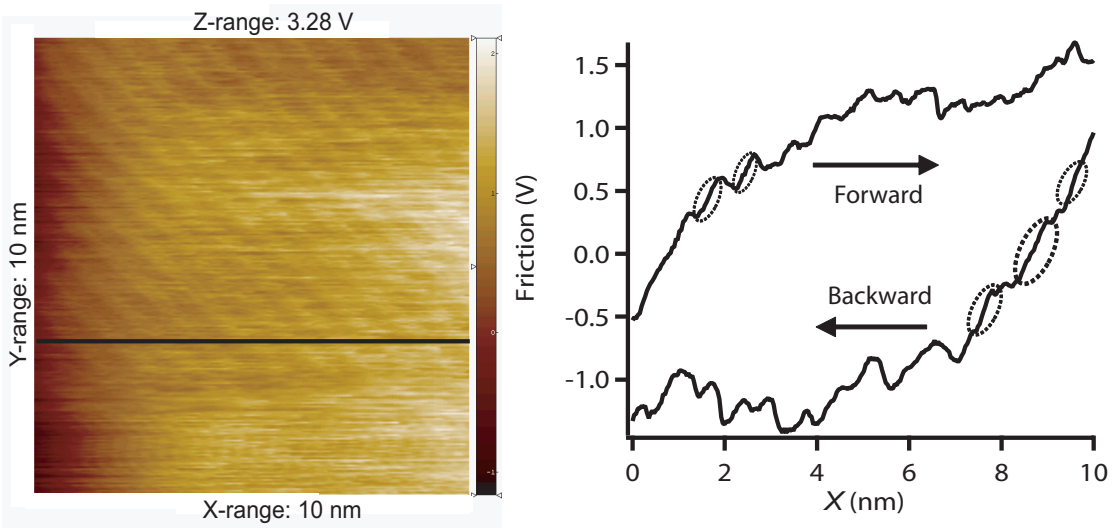

Figure 2.2.7: *The typical friction image for forward direction (upper) is taken in contact mode with a silicon nitride tip on silicon surface at room temperature. The normal force is maintained at* 2 *(nN). The scan area and speed are* 10×10 nm^2 *and* 2 *lines per second. Only the circled parts of the cross-section curve are used for lateral force calibration because they are non-slippage parts, i.e., the change of the lateral signal is proportional to the change of the scanner deformation.*

intensity of the laser spot projected onto the photo-detector ($I_{total} = A+B+C+D$). Therefore the value of ΔV in Eq. 2.2.6 has to be normalized to the I_{total} used in the calibration friction experiment of Fig. 2.2.7, which was 0.47 V. Another essential calibration is the difference between the amplitude signal detected and send out by the lock-in amplifier. For the lock-in amplifier used in my experiment (SRS 830), the relation between the output and detected signal (here is the amplitude of the torsion/lateral signal, ΔV) is $V_{output} = V_{detected} \times \frac{10}{Sen.}$, where the $Sen.$ is the selected sensitivity of the lock-in amplifier. By the corrections of I_{total} and the signal of lock-in amplifier, Eq. 2.2.6 can be finally written as:

$$F_L = 2.51 \times 10^{-3} \times k_N \frac{hL^2}{(h+\frac{t}{2})^2} \cdot \frac{\Delta V_{output} \times Sen.}{I_{total}} (nN) \qquad (2.2.7)$$

With SEM images, L, t, w, (Fig. 2.2.4) and h (Fig. 2.2.8) can be measured and the analytical value of Eq. 2.2.7 can be extracted from the measurement.

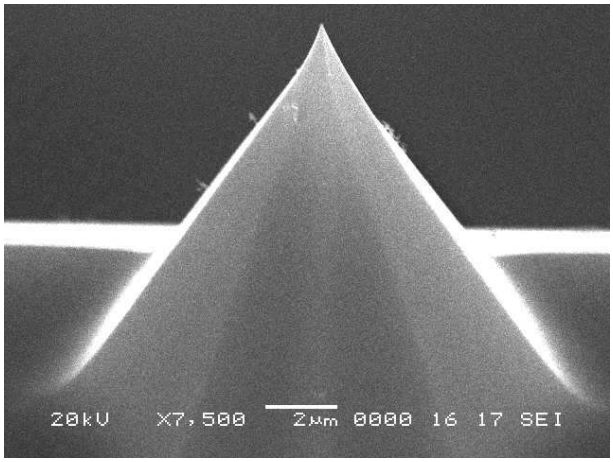

Figure 2.2.8: *A SEM image of the tip shows the tip height, h, a essential value for the lateral force constant calibration, Eq. 2.2.6.*

2.2.3 Tip-Sample Distance Calibration

In Fig. 2.2.3, there is an assumption of zero deformation of the tip and sample surface contact, i.e., both the hardness of the tip and surface are infinitely high. However, realistically, there exists deformation in contact, Fig. 2.2.9. For the small elastic deformation, the contact behavior can be described by the Hertz model [66]:

$$\delta = (\frac{9{F_N}^2}{16RE^{*2}})^{\frac{1}{3}} \tag{2.2.8}$$

where δ is the total deformation, R is the tip radius, F_N is the normal force loaded on the surface, and $E^* = \frac{1}{\frac{1}{E_1}+\frac{1}{E_2}}$ is the reduced elastic modulus of the tip and sample surface. All the parameters on the right side of Eq. 2.2.8 are known (F_N from the force-distance curve, R from the SEM image, and E^* from literatures) and the total deformation can be extracted.

Figure 2.2.10 shows that the force-distance curve determined by the method in 2.2.1 is in a good agreement with the Hertz model fitting (less than 0.1 nm error).

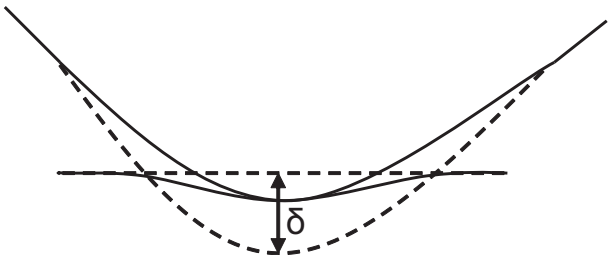

Figure 2.2.9: *In a non-perfect hard contact between the tip and sample, both the tip and surface are deformed by the normal force. For elastic deformation, the total deformation, δ, follows Eq. 2.2.8.*

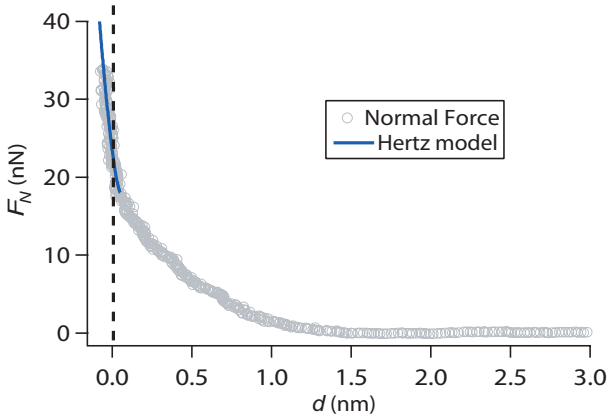

Figure 2.2.10: *A normal force-distance curve and the fitting of Hertz model (Eq. 2.2.8). The error between the measurement and the theoretical fitting is less than 0.1 nm.*

2.2.4 Drift Analysis

The force-distance curve used for the pre-amplified coefficient calibration is measured with a approaching speed (> 200 nm/s), much faster than the drifting speed, therefore the effect of the drifting can be neglected for this force-distance curve. In our force measurements, the tip is quasi-statical (with extremely slow constant speed) approaching to the sample surface. Therefore, any drift of the tip and/or sample in the z-direction is going to distort the force-distance curves. However, if the drifting is linear (constant speed), the precise force-distance curve still can be deduced. The basic idea is to acquire the same force-distance curves by approaching and retracting in order to deduce the drifting speed, the same idea as driving a boat downstream and upstream to measure the current velocity.

Without any drift, bending vs scanner deformation curves acquired by approaching and retracting are the same as the curve in Fig. 2.2.2, i.e., the contact points for both approaching and retracting are equivalent and the curve slope is -1 in the contact regime (regime II of Fig. 2.2.2) if there is no deformation in Eq. 2.2.8 (the E^* is infinite). According to section 2.2.3, it is a good approximation in this thesis and the following section is based on this approximation.

In our method of calibrating the linear drift, we measure the force-distance curve by approaching and retracting with the same speed and time, the total scanner deformation for approaching and retracting are the same (D nm). With linear drifting, the scanner deformation is not the sole source of how much the tip travelled. Therefore the contact point for approaching and retracting are different and the slope of the curve in contact regime is not -1 anymore as shown in Fig. 2.2.11. Since the total deformation is the same for both approaching and retracting, the total displacement showed by the AFM for both is still 'D nm', see Fig. 2.2.11. Here, we would like to remark that the 'D nm' for the approaching and retracting curve are actually different due to the linear drift. An efficient method to correct the effect of the drift is to

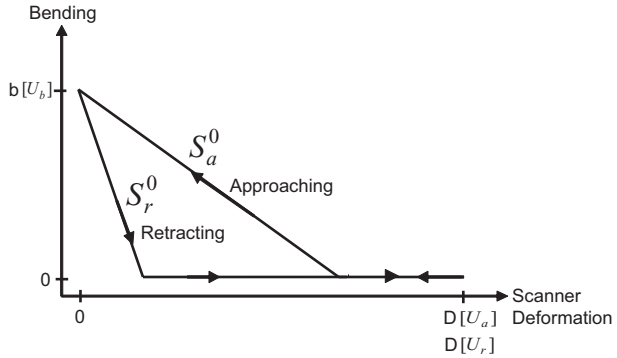

Figure 2.2.11: *With a constant speed drift, the typical approaching and retracting bending-scanner deformation curve becomes non-identical to each other. The slope of the curve in contact regime is not* -1 *for both approaching and retracting. Although the sweep range (D nm) is the same for approaching and retracting in the measurement display, the unit, nm, of them are distorted by the constant drifting. True compensated units,* U_b*,* U_a*, and* U_r*, are introduced for the purpose of calibrating the bending, approaching curve, and retracting curve. In contact regime, the original slope of the approaching and retracting curves in terms of the distorted 'nm' unit,* S_a^0 *and* S_r^0*, are used for calibrating these true compensated units.*

introduce new length units for the scanner deformation in approaching and retracting and for the cantilever normal bending. By determining the ratio between these new units and the original unit (1 nm) the true force-distance curve can be extracted.

During the process of the correction, the approaching and retracting curves have to be treated separately due to the different units in scanner deformation. Since the force-distance curve has been well calibrated with a fast approaching speed, the slope of the approaching and retracting curve in the contact regime, S_a and S_r, should be also -1, i.e., the bending equals to the scanner deformation. By this assumption, the new unit for bending, U_b, can be written in terms of the new unit for the scanner deformation of approaching (U_a) as:

$$U_b = \frac{U_a}{S_a^0} \tag{2.2.9}$$

where S_a^0 is the initial slope of the approaching curve in contact regime. Also, the S_r should be -1 and the new unit of scanner deformation in retracting, U_r, can be

written in terms of U_b/U_a as

$$U_r = U_b \cdot S_r^0 = \frac{S_r^0 \cdot U_a}{S_a^0} \tag{2.2.10}$$

where S_a^0 is the initial slope of the retracting curve in contact regime. We assume that the drift velocity V_{drift} is in the same direction of retraction, therefore, the true total approaching ($D\ [U_a^{'}]$) and retracting ($D\ [U_r^{'}]$) are:

$$D[U_a] = (V_{scanner} + V_{drift})T[nm] \tag{2.2.11}$$

$$D[U_r] = (V_{scanner} - V_{drift})T[nm] \tag{2.2.12}$$

where $V_{scanner}$ and T are the velocity of the scanner deformation and the time of approaching/retracting. From these equations above, U_a, U_b, and U_r can be deduced in term of the real length unit, nm,

$$U_a = \frac{2S_a^0}{S_a^0 + S_r^0}[nm] \tag{2.2.13}$$

$$U_r = \frac{2S_r^0}{S_a^0 + S_r^0}[nm] \tag{2.2.14}$$

$$U_b = \frac{2}{S_a^0 + S_r^0}[nm] \tag{2.2.15}$$

After the correction for the linear drifting, the bending vs scanner deformation curves go return to Fig. 2.2.2 and the force-distance curve can be extracted the same way as stated in 2.2.1. A program was developed to automatically select the measurements with linear drift and compensate the drift by this method. The program and this method was submitted as a Georgia Tech Invention Disclosure.

2.2.5 Misalignment Issue in Shearing Experiments

In our lateral force measurements, it is important that the shearing is parallel to the sample surface. If there is an angle other than zero between the shearing direction and sample surface, the contact point (zero distance between tip and sample) can not be determined; also, an artificial lateral force will occur due to the lateral tapping

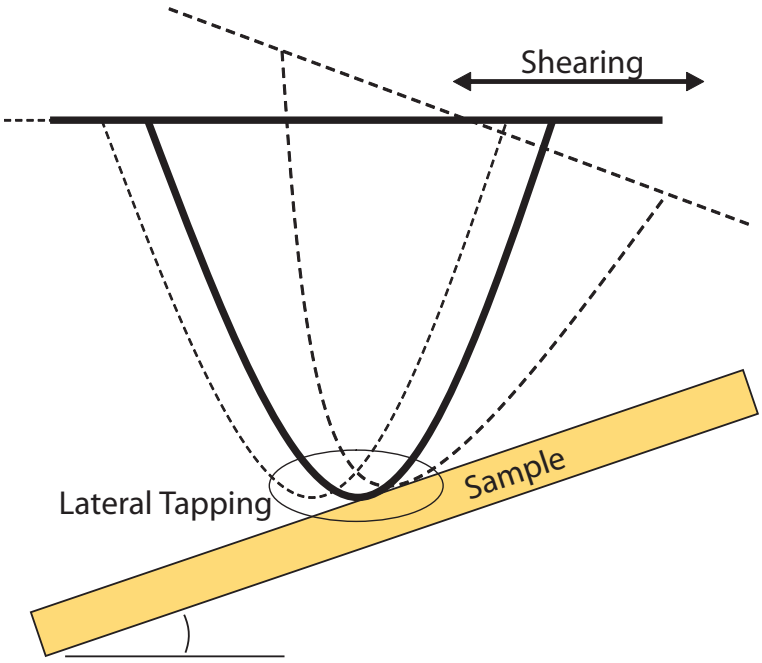

Figure 2.2.12: *If there is an angle between the shearing and sample surface, the vibrating tip is going to tap the surface laterally. Therefore, it is impossible to determine the zero distance in force-distance curves and the detected lateral force from the single of the torsion amplitude is affected largely by the tapping.*

between the tip and sample surface (Fig. 2.2.12) and it is impossible to extract the real lateral force from this artificial lateral force. In order to shear parallel to the sample surface, before each measurement we tilted the stage that holds the sample until the difference in height of the sample surface topography across an area of 1×1 μm^2 (as obtained from AFM sample topography imaging) was smaller than 1 nm. This corresponds to an angle less than 0.06^o between the sample surface and the tip shearing direction, thus, under the largest shearing in our experiments (10 nm), the difference in hight of the tip is less than 0.02 nm, which is smaller than the roughness of our samples (1 nm for glass, 0.2 nm for mica and HOPG) and the error of the scanning piezo in z-direction (0.05 nm).

2.2.6 Resonance of Piezo Scanner

In the lateral force measurements, a sinusoidal signal with amplitude X' and frequency f is applied to the scanner piezo in x-direction (see Fig. 2.2.6). However, the amplitude of the scanner piezo (X_0) is not the same as X' for all frequencies due to the resonant response of the piezo, which has to be calibrated.

To calibrate the resonance of the scanner piezo, a lock-in amplifier is used to apply a sinusoidal signal to the scanner piezo in x-direction to oscillate the tip laterally when the tip is in contact with the surface. The same lock-in amplifier is used to monitor the amplitude of the lateral signal due to the statical fraction between the tip and surface. In order to make sure that there is no slippage between the tip and mica surface, the amplitude applied to the scanner piezo in x-direction is the minimum output of the lock-in amplifier, 0.004 V, which is correlated to 0.08 nm if there is no resonance, so the measured amplitude (torsion amplitude in Fig. 2.2.5) will be proportional to the displacement of the piezo in x-direction. Figure 2.2.13 shows the resonant behavior of the scanner piezo in x-direction from 50Hz to 3kHz. The amplitude is normalized to the value at low frequency (50Hz) because of no resonance at low frequencies. By applying the resonant curve in Fig. 2.2.13, the true amplitude of the tip/scanner, X_0 in Fig. 2.2.6, can be extracted. The value X_0 has no effect on lateral force measurements, however it plays an important role in calculating the shearing speed (V_{shear}) in next chapter.

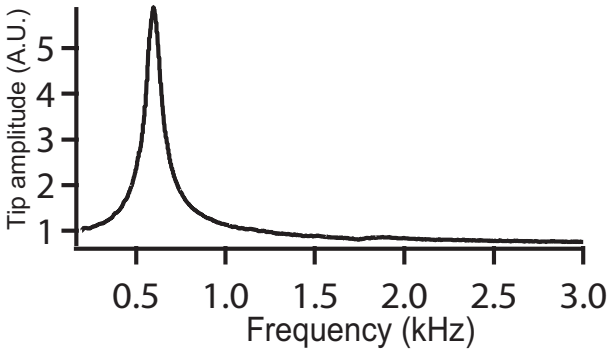

Figure 2.2.13: *There is a significant resonance of the scanner piezo in x-direction. The silicon tip is in contact with mica surface with the normal force* $F_N \cong 10$ *nN. This experiment was done with the same setup as in Fig. 2.2.6 with* $X' = 0.004$ *V*$=$ 0.08 *nm, which is small enough to guarantee a hard contact without slippage.*

CHAPTER III

STRUCTURED AND VISCOUS WATER IN SUB-NANOMETER GAPS

(*This chapter originally appeared as a paper by the author*: "Structured and viscous water in subnanometer gaps," by Tai-De Li, Jianping Gao, Robert Szoszkiewicz, Uzi Landman, and Elisa Riedo, in **Physical Review B**, volume 75, page 115415, in 2007.)

In this chapter, we report on direct high resolution atomic force microscope (AFM) measurements of oscillatory solvation forces and markedly increased viscosity in sub-nanometer pure water films. The role of wettability and roughness of the confining surfaces is also investigated. In our AFM experiments [10, 67], a nano-size spherical silicon tip is brought quasi-statically to the vicinity of a flat solid surface, all immersed in purified water, while small lateral oscillations are applied to the cantilever support (see Chapter II). The normal and lateral forces acting on the tip are measured directly and simultaneously as a function of the water film thickness, i.e. tip-sample distance (Fig. 3.0.14. Because of the mechanical stability of our apparatus, and a judicious proper choice of the cantilever stiffness (see 1.4.2), we are able to measure, during force acquisition, the tip-surface distance with sub-Angstrom resolution, all the way down to the last adsorbed water layer. In order to investigate the role of roughness and surface chemistry of the confining surfaces we have studied water films nano-confined between a silicon tip and three different solid surfaces: an atomically smooth hydrophilic, i.e. wetting, surface (mica), a nano-rough (root-mean-squared (rms) roughness less than 1 nm) hydrophilic surface (soda lime untreated glass), and an atomically smooth hydrophobic, i.e. non-wetting, surface (highly oriented pyrolytic

graphite, HOPG). We remark that the surface of our Si tip is likely to be oxidized [68]. All the Molecular Dynamic (MD) simulations in this chapter are provided by Prof. Landman and Dr. Gao.

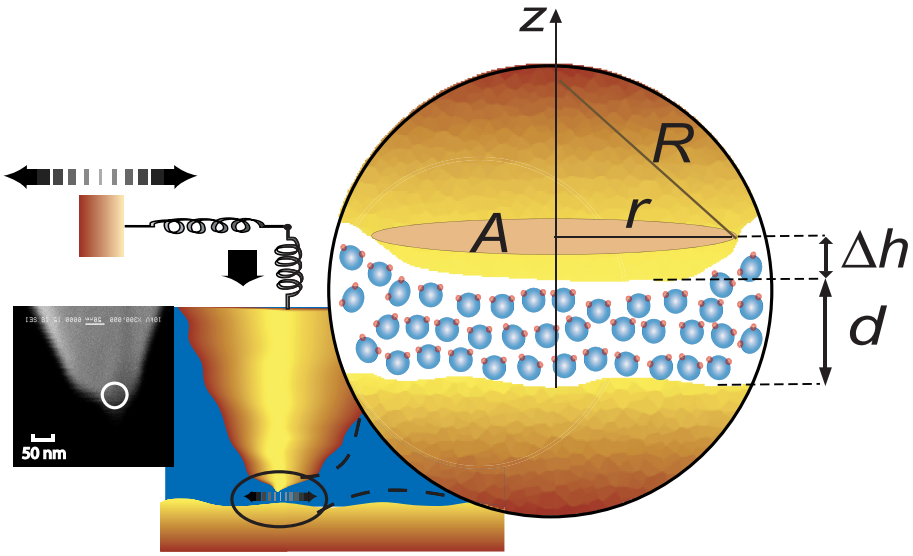

Figure 3.0.14: *An AFM was used to measure the normal and lateral forces between a nanosize untreated silicon tip and three different flat solid surfaces in deionized water. In this figure we also show a scanning electron microscopy (SEM) image of the tip apex and the schematic of how we approximate the area in Eq. 3.4.1 .*

3.1 State of the Art

Water under nano-confinement is ubiquitous, with examples including clay swelling, aquaporines, ion channels [5, 6], and water menisci in micro-electromechanical-systems [69, 10]. However, the structural and rheological characteristics of nano-confined pure [36, 32, 24, 60, 70, 72] and ionized water [33, 26, 25] continue to be the subject of discussion and debate. In particular, for nano-confined pure water, contradictory results have been reported about the presence [58], or absence [24, 37, 61], of oscillations in the solvation forces and concerning the value of the viscosity [24, 60, 71, 72, 61]. This unsatisfactory situation is mainly due to the lack of direct, high resolution measurements of the solvation forces and viscosity for water confinements smaller than

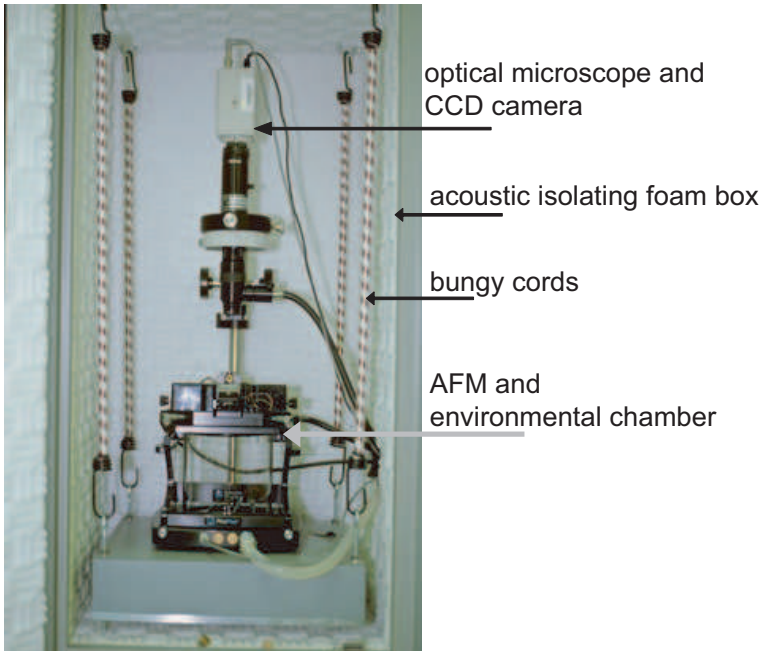

Figure 3.2.1: *A Molecular Imaging PicoPlus AFM.*

1-2 nm. Moreover, the influence of the wettability and roughness of the confining surfaces on the properties of nano-confined pure water remains largely unknown.

3.2 Experimental Setup

The experiments were performed with a Molecular Imaging PicoPlus AFM. We remark that our direct and quasi-static normal force measurements require a signal to noise ratio close to the instrumental limit of an AFM working in liquids. For good protection against external mechanical vibrations, our AFM is closed in a noise-isolated box and hung up by four bungy cords with low resonance frequency (see Fig. 3.2.1). The complete system is mounted on an optical table (RS1000-36-18) from Newport. Another instrumental problem in quasi-static force measurements is that, during the tip-sample approach, the tip snaps into contact with the surface at a distance where the gradient of the tip-sample forces exceeds the cantilever normal spring constant, k_N[24, 37], i.e. when $|\partial F_N/\partial d| \geq k_N$. To overcome this problem, we used relatively stiff cantilevers (see details in 1.4.2).

While the AFM tip approached the solid surface in water, lateral oscillations were applied to the cantilever holder by means of a lock-in amplifier (see details in 2.2.2). In order to shear parallel to the sample surface, the stage that holds the sample was tilted before each measurement until the difference in height of the sample surface topography across an area of 1×1 μm^2 (as obtained from AFM sample topography imaging) was smaller than 1 nm (see details in 2.2.5). This corresponds to an angle smaller than 0.06^o between the sample surface and the tip during shearing.

We remark that even when the noise conditions were ideal, not all the measurements presented oscillations in the normal force. Oscillations were detected in 7 measurements on mica, 5 on glass, and 7 on HOPG. After SEM measurements, we noted that the presence of protuberances on the tips was the origin of the disappearance of oscillations close to the solid surface. However, the results for the viscosity are nicely repeatable in all the measurements (about 30 measurements for each surface). We estimated that the error in the normal and lateral force was about ± 0.1 and 0.05nN, respectively. The error in the piezo z-position was estimated to be ± 0.3Å.

The purity of the water used in our AFM liquid cell was tested before and after the experiments by the methods described in 2.1.1.

3.3 Normal Solvation Force

Oscillatory solvation forces for sub-nanometer water confinement were obtained previously only from indirect dynamic measurements on a soft sample [58], where a nanotube tip is vibrated along the approach direction with an amplitude of 3.7 nm and the forces are then extracted from the measured frequency shift through a mathematical model [58]. Earlier direct quasi-static measurements of solvation forces in purified water did not show oscillations and/or could not access confinements smaller than 2.5 nm [24, 37, 61].

Figure 3.3.1 presents direct quasi-static normal force, F_N, measurements ((A),

(A'), (a) and (b)) together with theoretically calculated F_N ((a') and (b')) as a function of the tip-sample distance d for wetting and non-wetting surfaces. Figure 3.3.1(A) shows the presence of oscillations in F_N vs. d curves when the AFM tip approaches a (wetting) nano-rough glass surface in water for 0.3 nm $< d <$ 2 nm. Figure 3.3.1(A') shows F_N vs. d for the same glass surface for the full range of distances, e.g. 0 ± 0.03 nm $< d <$ 3 nm; the $d = 0$ location was inferred as the distance for which the slope of the curve diverges. We remark that the data for separations smaller than $\sim$ 0.3 nm correspond to relatively strong interactions between the last water layer and the wetting surface [73]. Figure 3.3.1(a) shows oscillatory solvation forces for a (wetting) mica surface, which is atomically smooth. The average distance, δ, between adjacent steps in Fig. 3.3.1(A) and (a) is 0.27 and 0.22 nm, respectively. Oscillations of the normal force and values of δ close to the dimension of a water molecule indicate transitions occurring when the water film passes from $n + 1$ to n layers [13, 14, 74].

From Fig. 3.3.2 (for the mica surface), we observe that for smaller d values, δ decreases from 0.37 to about 0.21 nm, in agreement with the results of X-ray reflectivity measurements [75]. A maximum of four different adjacent oscillations are observed in our experiments. Our measurements indicate the presence of layering on atomically smooth and nano-rough wetting surfaces. While atomic-scale roughness obliterates liquid density oscillations of hydrocarbon chain molecules (e.g. alkanes [14]), the effect is significantly weaker for globular molecules. Small H_2O molecules interact strongly with point charges of the atomically rough wetting glass surface, thus "filling the holes" and effectively smoothing the morphological inhomogeneities.

Figure 3.3.1(b) shows experimental F_N vs. d curves for a non-wetting graphite surface. The force oscillations found for this case are less developed compared to the smooth wetting surface case (Fig. 3.3.1(a)).

The stepwise shape of the experimental normal force curves reflect the inability

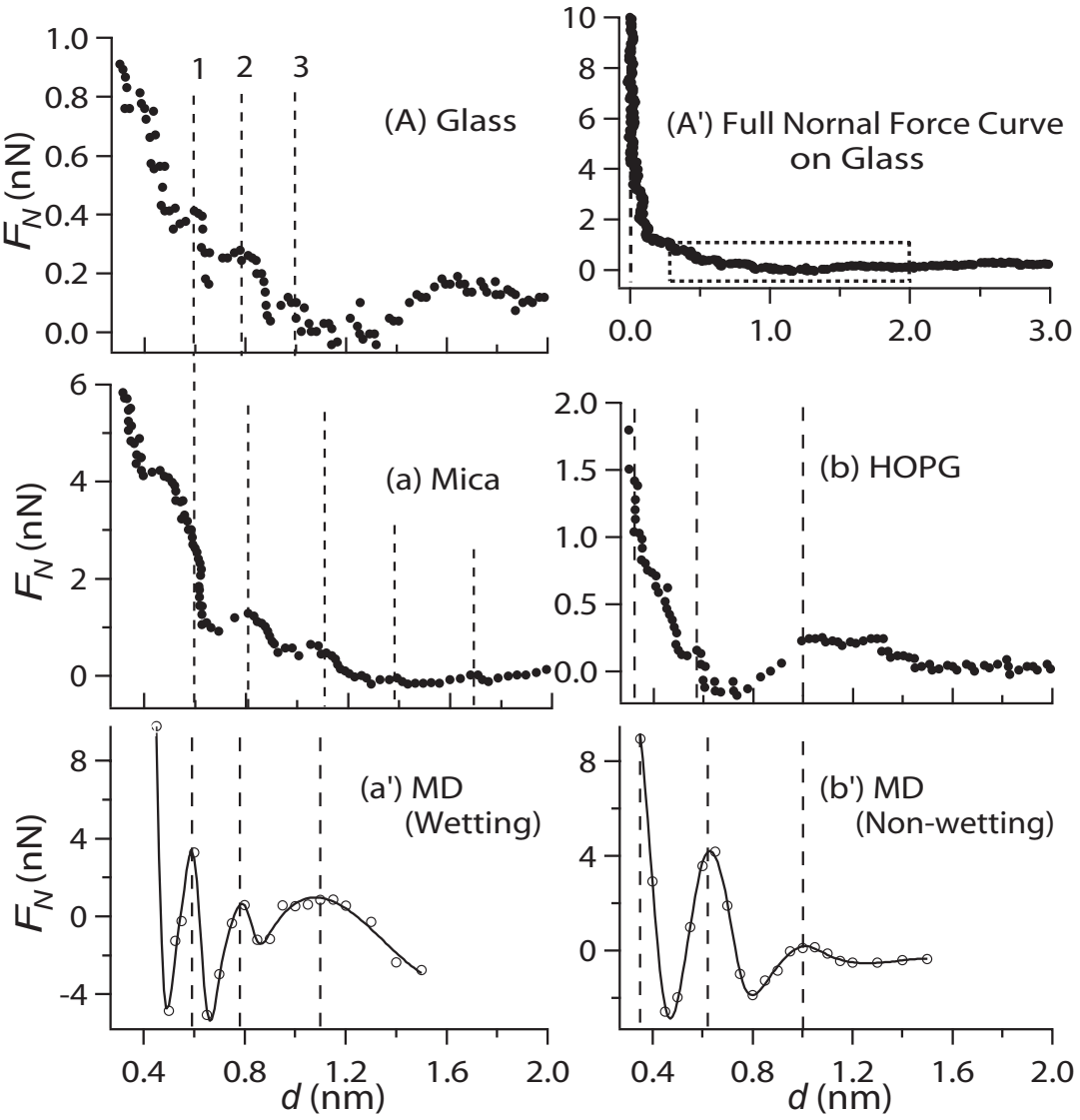

Figure 3.3.1: *F_N vs d for wetting ((A), (A'), (a), and (a')) and non-wetting ((b) and (b')) surfaces. The vertical dashed lines indicate the position of the force maxima corresponding to layer $n = 1$, 2, and 3. The estimated error in F_N is ± 0.05 nN; the error in d is ± 0.3 Å.*

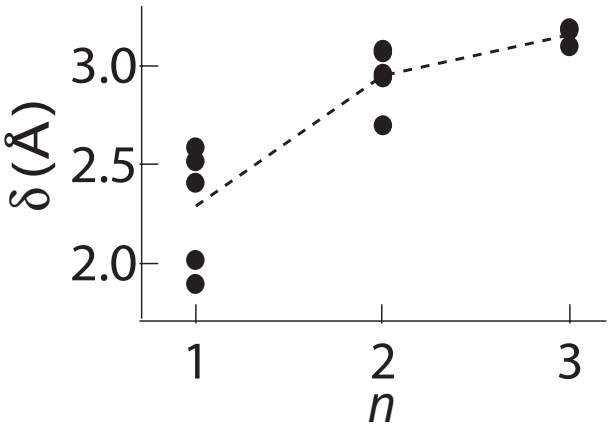

Figure 3.3.2: *Average distance (δ) between adjacent steps in Fig. 3.3.1 corresponding to different layers, obtained from several measurements.*

of the cantilever to bend following the "true" force gradient in the attractive region [24, 37]. However, this problem does not affect the lateral force data (see Fig. 3.4.1) because the lateral force is given by the amplitude of the cantilever's torsion.

Figures 3.3.1(a') and (b') present the solvation forces for wetting (a') and non-wetting (b') quartz surfaces, obtained through MD simulations. The agreement between the salient features of the experimental and theoretical force curves is quite remarkable, exhibiting clearly a higher propensity for solvation force oscillations in the case of wetting surfaces, as well as a decreasing value of δ as the confining gap width becomes smaller.

3.3.1 Comparison of Experimental Results with DLVO and Structural Forces

The forces between a sphere and a plane surface have been previously described by the DLVO theory and structural force in section 1.1. Thus, the total force are given

by:

$$
\begin{aligned}
F(d) &= F_0 \cos(\frac{2\pi d}{a} + \phi) \exp(-\frac{d}{k}) + \alpha \lambda_D R \gamma^2 \exp(-\frac{d}{\lambda_D}) - \frac{AR}{6d^2} \\
&\text{where} \qquad (3.3.1) \\
\alpha &= 128\pi C_0 \; k_B T \\
\gamma &= \frac{1}{2}[\tanh(\frac{e\Psi_1}{4k_B T}) + \tanh(\frac{e\Psi_2}{4k_B T})]
\end{aligned}
$$

where F_0 and ϕ are the amplitude and phase of the oscillatory solvation term; d is the distance between the tip and the sample; a is the periodicity of the oscillatory solvation force, which should be the molecular size of water; k is the decay length of the solvation force; k_B is Boltzmann's constant; T is the absolute temperature; λ_D is Debye length ($\lambda_D = 0.306/\sqrt{C_0}\ nm$ for $1:1$ electrolytes); R is the tip radius; e is the electron charge; Ψ_1 and Ψ_2 are the effective surface energies of the two surfaces in water [76, 62]; A is Hamaker's constant of the silicon-water-mica system [77]; C_o is the ionic concentration. The first term on the righthand side of Eq. 3.3.1 is the decaying oscillatory solvation force which corresponds to the transition between ordered and disordered states of the liquid layers (see 1.1.4). The second and third term are from the DLVO theory (see 1.1.2 and 1.1.1). For water without salt, C_o is the concentration of protons which is measured by a pH-meter. We note that pure water in air is slightly acidic due to atmospheric CO_2 being dissolved into water. The number of K^+ ions desorbed from the mica surface is negligible compared with protons from CO_2 [78]. Table 3.3.1 shows the values of the parameters used in Eq. 3.3.1 to fit the experimental normal force vs. distance curves. We remark that the only fitting parameters are F_0, ϕ and k.

As we discussed in 1.1, in our experiment, DLVO forces are uniform for distance larger than 1 nm, as shown in Fig. 1.1.3. Thus, the DLVO terms in Eq. 3.3.1 were offset to fit the background force. However, for $d < 1$ nm, the structural force dominates the interaction. The experimental result does not fully follow the theoretical curve

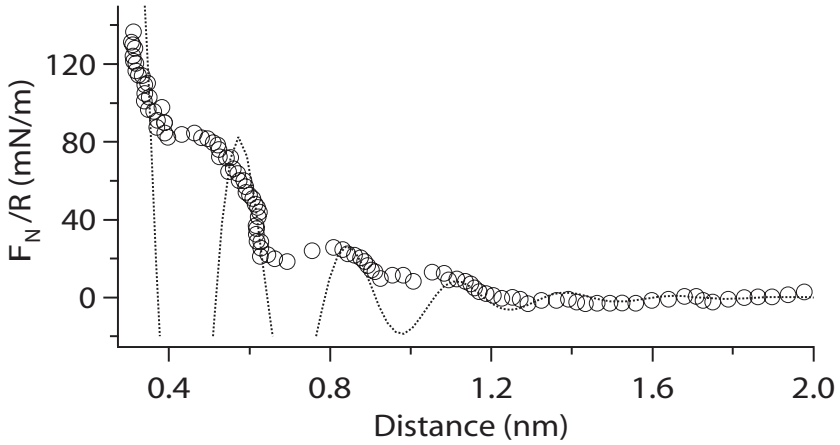

Figure 3.3.3: *Comparison between experimental data and the theoretical forces. The fitting force curve was offset to fit the background force.*

h

Table 3.3.1: Parameters used in the Eq. 3.3.1 to fit the experimental curves. F_0, ϕ, and k are fitting parameters. R is measured by scanning electron microscopy (SEM). ψ_{mica}, ψ_{si}, and H are from Ref. [76, 62, 77]. (Ψ_{Si} was calculated from the surface charge density provided in Ref. [62])

F_0[nN]	a[$\mathring{A}$]	ϕ	k[nm]
38	2.7	1.4	
$C_0[10^{-6}\text{M}]$	R[nm]	Ψ_{mica}[mV], Ψ_{si}[mV]	A[10^{-20} J]
3.16	50 ± 10	130,600	3.5

because the force gradient can not larger than the spring ($|\frac{\partial F}{\partial d}| \geq k_N$), as discussed in 1.4.2. The experimental result is in a good agrement with the theory presented in chapter I.

3.4 Viscous Force and Viscosity of Nano-confined Water

To date, only a few measurements of the viscosity of confined purified water have been reported [24, 60]. In the first study [24], a surface force apparatus was used to estimate, through the use of a drainage formula, the viscosity of films with thicknesses less than 2.4 nm. In this way, a viscosity comparable with bulk water has been estimated. In the second study [60], the viscous force in water films with thickness $d > 1$ nm was derived by means of a technique based on scanning near-field optical microscopy. An increased viscosity, by up to 4 orders of magnitude, was reported. This is in agreement with a dramatic transition in the mechanical properties of a water meniscus found in Ref. [61]. Clearly, these indirect measurements yielded contradictory results and did not access the $d < 1$ nm regime which is indeed the focus of this study.

In our AFM experiments, we detect simultaneously the normal solvation forces and the viscous lateral forces as a function of the tip-sample distance. We can thus directly extract the viscosity of the water film confined between our tip and a mica, glass and HOPG surface (see Fig. 3.4.1 (a), (b) and (c), respectively). In the insets to these figures we show the lateral force divided by the shear velocity for each surface. The viscosity has been calculated following the model of two smooth parallel sliding plates separated by a distance d with a fluid in between them. The lateral force F_L required to keep one plate moving at a velocity v_{shear} with respect to the other one is proportional to the contact area A and to $\frac{v_{shear}}{d}$. The proportionality coefficient η is called the dynamic viscosity. For a simple incompressible Newtonian fluid, η is given

by [12]:

$$\eta = \frac{F_L}{v_{shear}} \cdot \frac{d}{A}. \tag{3.4.1}$$

A more rigorous treatment of our experimental geometry involves consideration of a spherical tip, of radius $R = 50$ nm, sliding close to a planar solid with a distance d from the tip apex to the surface. Such a case was indeed considered by Goldman *et al.* [79] but with a constant viscosity everywhere. Since in our experiments for $d < 1.3$ nm the confined water film is able to sustain a shear stress over macroscopic times, i.e. the viscosity at $d < 1.3$ nm is much higher in the vicinity of the tip apex than everywhere else, we limit the treatment [80] to the liquid confined by the tip in a region of thickness $0 \leq z \leq d + \Delta h$ (see Fig. 3.0.14), where the solid surface is at $z = 0$. We then use the expression for the local Newtonian shear stress $\sigma = \eta[v_{shear}/(d + \Delta h(r))]$ (see Fig. 3.0.14), to evaluate the total lateral force via

$$F_L = \int_0^{r'} 2\pi r \sigma(r) dr, \tag{3.4.2}$$

where $r' = \sqrt{2R\Delta h - \Delta h^2}$. This yields the expression for the viscosity,

$$\eta = \frac{F_L}{2\pi v_{shear}[(R + d)\ln(1 + \frac{\Delta h}{d}) - \Delta h]}. \tag{3.4.3}$$

Equation 3.4.3 gives results which are well approximated by the planar geometry considered in Eq. 3.4.1, where the effective area A corresponds to the spherical segment defined by the intersection between the spherical tip and a plane at $z = d + \Delta h$. The largest difference in the viscosity calculated by using the spherical and planar approximations occurs for small d and large Δh. For example, for mica with $\Delta h = 0.25$ nm (a water molecule diameter) and $d = 0.5$ nm, the spherical approximation yields $\eta = 3.5 \times 10^2$ poise, while for the planar one $\eta = 3 \times 10^2$ poise (see Fig. 3.4.2).

For wetting surfaces (Fig. 3.4.1 (a), and (b)), the viscosity of nano-confined water increases when increasing the confinement, reaching a value at $d = 0.5$ nm which is four orders of magnitude larger than the viscosity of bulk liquid water at room

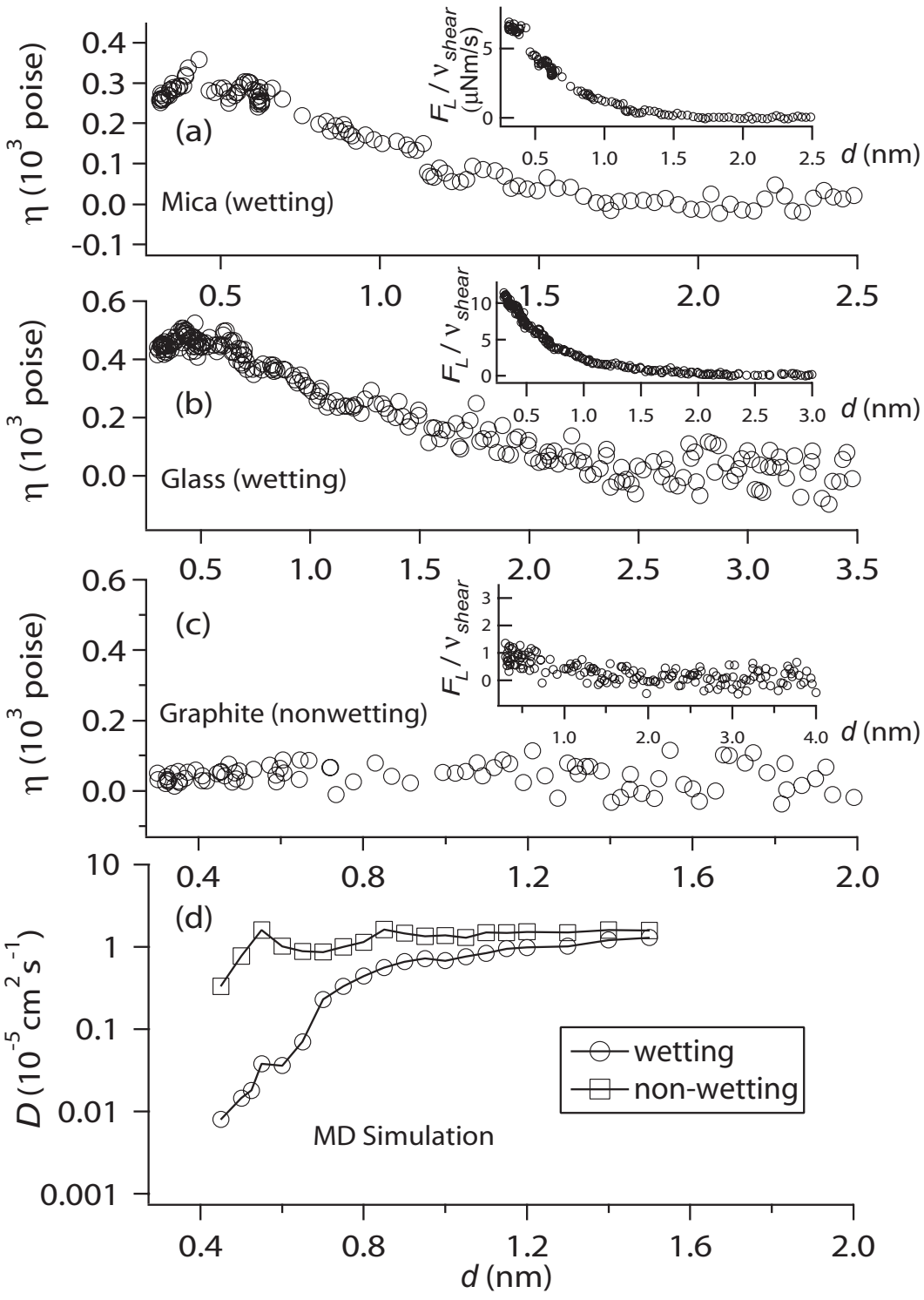

Figure 3.4.1: *Experimental η vs d as calculated from Eq. 3.4.1 (where $A = 75$ nm^2 calculated for $\triangle h = 0.25$ nm, see text) for (a) mica, (b) glass, and (c) HOPG. The estimated error in F_L is ± 0.05 nN; the error in d is ± 0.3 Å. In the insets of these figures, we show for the corresponding surfaces the experimental F_L/v_{shear} vs d. In (d), Simulated diffusion constant (D) vs d in water films confined by wetting and non-wetting interfaces.*

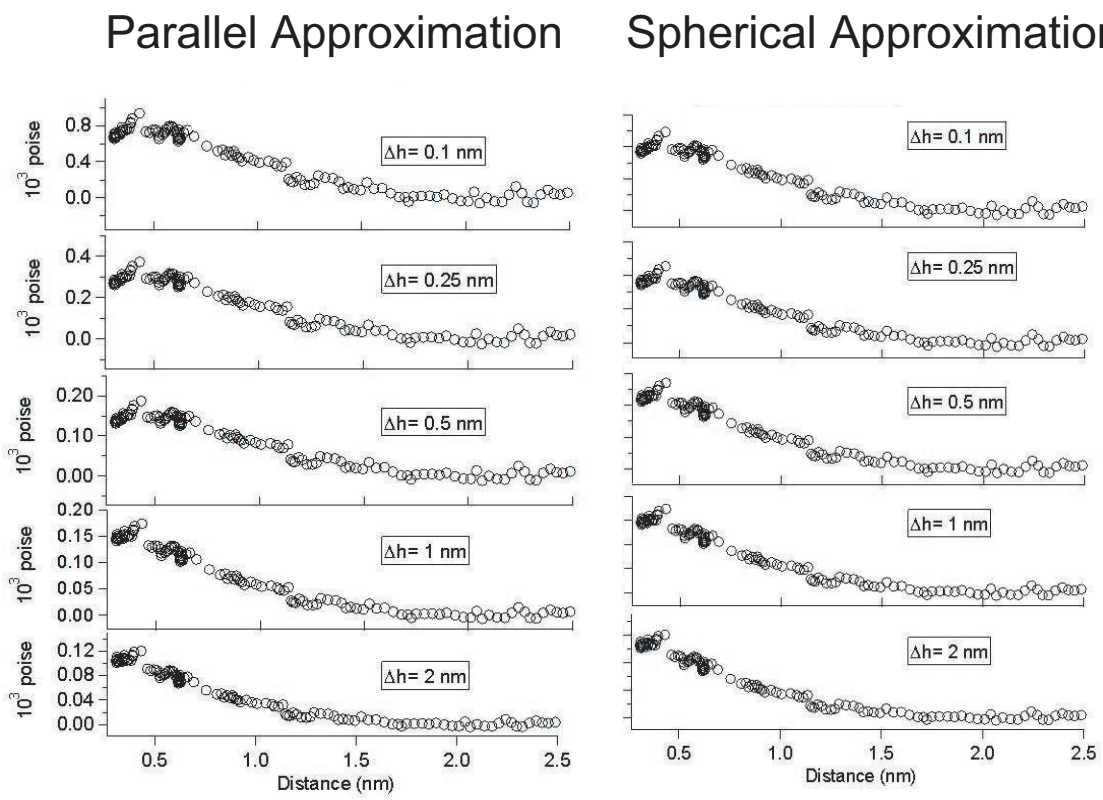

Figure 3.4.2: *The comparison between viscosities calculated from planar and spherical approximation.*

temperature, i.e. about 10^{-2} poise. The bulk viscosity of water is recovered for gaps larger than 1.6 nm and 2 nm, for mica and glass surfaces, respectively. In contrast, for the non-wetting surface (HOPG), the viscosity of the confined water film remains constant, within experimental error, with increasing confinement (Fig. 3.4.1 (c)); the slight increase of the lateral force itself (see inset) for smaller values of the gap width is consistent with Eq. 3.4.1. These measurements are in agreement with the sharp drop in the diffusion constant, D, (circles in Fig. 3.4.1 (d)) obtained by MD calculations on the wetting surface, while D remains essentially constant for the non-wetting case. We believe that the different viscosity and diffusivity between wetting and non-wetting surfaces is due to the fact that water remains well attached to wetting surfaces, while it can slip easily on non-wetting surfaces. The overall non-oscillatory (see caption of Fig. 3.4.1) increase of the viscosity, and the decrease of the diffusion constant in the

wetting cases originate from stronger pinning interactions between the partial charges of the water molecules and those associated with the hydrophilic surfaces as the two surfaces are brought closer to each other.

3.5 Calculations of the minimum number of water molecules between the AFM tip and the sample

The number of water molecules can be estimated by the following method:

1. The tip apex is modelled as a sphere with a radius of R=50 nm. Our data (Fig. 3.3.1) show that below 0.3 nm, there is no oscillation of the normal force for all samples, and 0.3 nm is comparable to the size of a single water molecule. Therefore, we calculate the volume V of the hashed volume showed in Fig 3.5.1 between the tip and the sample. V is obtained by subtracting the volume of the spherical cap V_{cap} (of height $h_1 = 0.3$ nm, and radius $R = 50$ nm) from the volume of the cylinder V_{cyl} (of base radius $a = [R^2 - (R - h_1)^2)]^{1/2}$, and height $h_2 = 0.3$ nm + 0.3 nm = 0.6 nm). We obtain: $V = V_{cyl} - V_{cap} = \pi a^2 h_2 - \pi(h_1)^2(R - h_1/3) = 42.3$ nm^3.

2. From the molar mass of water, $M = 18$ g/mole, the water density in ambient conditions $\rho = 1$ g/cm^3, and the Avogadro number $N_A = 6.02 \times 10^{23}$ molecules/mole, we obtain the average volume occupied by one water molecule in bulk, $V_w = (M/\rho)/\mathrm{N_A} = 0.03\mathrm{nm}^3$.

3. By dividing V by V_w, we obtain the lower bound (since bulk water is considered) on the minimum number, N, of water molecules in the confined region: $N = V/V_w = 1410$.

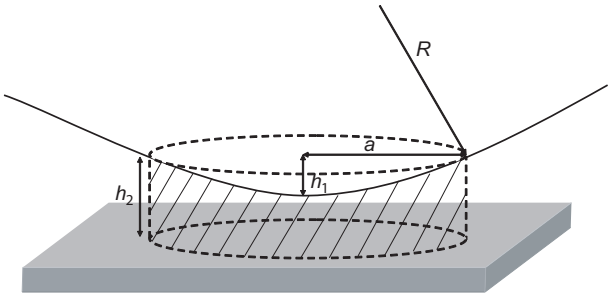

Figure 3.5.1: *Schematic of the volume of interest in our experiment.*

CHAPTER IV

VISCOELASTICITY OF NANO-CONFINED WETTING FLUIDS

(*This chapter originally appeared as a paper by the author*: "Nonlinear Viscoelastic Dynamics of Nanoconfined Wetting Liquids," by Tai-De Li and Elisa Riedo, in **Physical Review Letters**, volume 100, page 106102, in 2008.)

This chapter will emphasize the investigation of the viscoelastic response of nano-confined water and silicon oil (octamethylcylotetrasiloxane, OMCTS), as a function of shear amplitude and rate, by means of direct high-resolution AFM measurements. We observe a nonlinear viscoelastic behavior remarkably similar to that widely observed in metastable complex fluids, such as gels and supercooled liquids [81, 82, 83]. The origin of this nonlinear viscoelasticity in nano-confined water and in other nano-confined wetting liquids is a strain rate dependent relaxation time and slow dynamics. By measuring the viscoelastic modulus at different frequencies and strains, we find that the intrinsic relaxation time, τ_0, of nano-confined water is in the range $0.1 - 0.0001$ s, orders of magnitude longer than that of bulk water, and comparable to the dielectric relaxation time measured in supercooled water at $170 - 210$ K. [84].

4.1 State of the Art

Confined fluids exhibit unique structural, dynamical, electrokinetic, and mechanical properties that are different from those of the bulk [10, 85, 60, 70, 58, 86, 61, 88, 90]. Their behavior depends on the degree of confinement, strain rate, temperature, fluid molecular structure, and interactions with boundaries. Surprising effects have been found when water is confined in nanogaps. For example, the electric field induced

freezing of water at room temperature [8] and the extremely high viscosity of water close to a mica surface [26, 60]. Previous experiments and calculations have pointed out the key role of the confining surfaces [58]. A notable increase in viscosity and decrease in the diffusion constant was measured only when water was confined between hydrophilic surfaces (see chapter III). For hydrophobic confinement, the observed increase of viscosity was not very pronounced. Intriguingly, a similar behavior has been observed in confined glassy materials. When a glass-forming fluid is cooled down to the glass transition temperature, T_g, its viscosity grows by many orders of magnitude, and the confinement can increase or decrease T_g for strong or weak interactions with the walls, respectively [88].

So far, the viscosity measurements for nano-confined water have been performed in the linear viscoelastic regime. However, as observed in *macroscopic* rheological measurements, the study of the viscoelastic properties as a function of shear amplitude and rate is important for a better understanding of the dynamical and structural properties of fluids [81].

4.2 Non-linear Viscoelasticity

When a viscoelastic material is confined between two parallel plates separated by d, with area A, and a sinusoidal strain is applied to one of the plates at the frequency ω, $\gamma = \gamma_0 \sin(\omega t)$, the resulting stress between the plates can be written as $\sigma = \sigma_0 \sin(\omega t + \theta)$. The relationship between the strain amplitude, $\gamma_0 = \frac{X_0}{d}$, and the stress amplitude, $\sigma_0 = \frac{F_L}{A}$, is given by:

$$\frac{F_L}{A} = \mid G^* \mid \frac{X_0}{d} \tag{4.2.1}$$

where G^* is the viscoelastic modulus (see chapter I). The viscoelastic modulus contains the dissipative and elastic response of the confined material. In particular, G^* can be written as a complex sum of the storage modulus, G', and the loss modulus,

G'', i.e., $G^* = G' + iG''$, where [46]:

$$G' = \frac{F_L d}{AX_0}\cos\theta,\ G'' = \frac{F_L d}{AX_0}\sin\theta \tag{4.2.2}$$

For a purely elastic solid, σ and γ remain in phase, $\theta = 0$, and so $G'' = 0$ and $G' = G^*$.

In order to study the viscoelastic behavior of nano-confined water we have measured F_L and θ when we laterally oscillate the AFM cantilever holder. As a first approximation, the lateral spring constant of our silicon cantilever is much larger than the lateral tip-water contact stiffness for $d < 1$ nm [87]. As a consequence, the applied oscillation amplitude to the cantilever holder is equal to the shear amplitude of the tip apex. Figure 4.2.1 shows F_L and θ as a function of d for three different shear amplitudes at $\omega = 955.3$ Hz. For tip-sample distances larger than 1 nm, F_L is equal to zero within the instrumental error for any X_0. As soon as $d < 1$ nm, F_L increases with decreasing d, and almost diverges at $d = 0$ nm when the tip is in hard contact with the mica surface. In our previous study (chapter III), F_L has been used to calculate the viscosity of water (η) by using Eq. 4.2.1, and by considering water as purely viscous, that is, by making the approximation $\mid G^* \mid \approx G'' \approx \eta \cdot \omega$. This approximation is true when $\theta \cong 90^o$, which, as we show later, is the case for large strain rate amplitudes defined as $\dot{\gamma_0} \equiv \gamma_0 \cdot \omega$. However, the phase measurements presented in Fig. 4.2.1 show that in general the behavior of nano-confined water is viscoelastic, and furthermore, F_L does not grow proportionally with the shear amplitude, nor with ω (not shown here). This indicates that the viscoelastic response is not linear, and the viscoelastic modulus is shear amplitude dependent, $G^* = G^*(\gamma_0)$. Therefore, a detailed study of G^* as a function of γ_0 is needed to shed light into this nonlinear behavior.

By applying Eq. 4.2.2 to the data in Fig. 4.2.1, we have extracted G' and G'' as a function of d for different X_0 at a fixed ω. (The A used for Eq. 4.2.2 is the contact area corresponding to the spherical segment defined by the intersection between the spherical tip and a plane at $z = d + \triangle h$, $\triangle h = 0.25$ nm, i.e., a water molecule

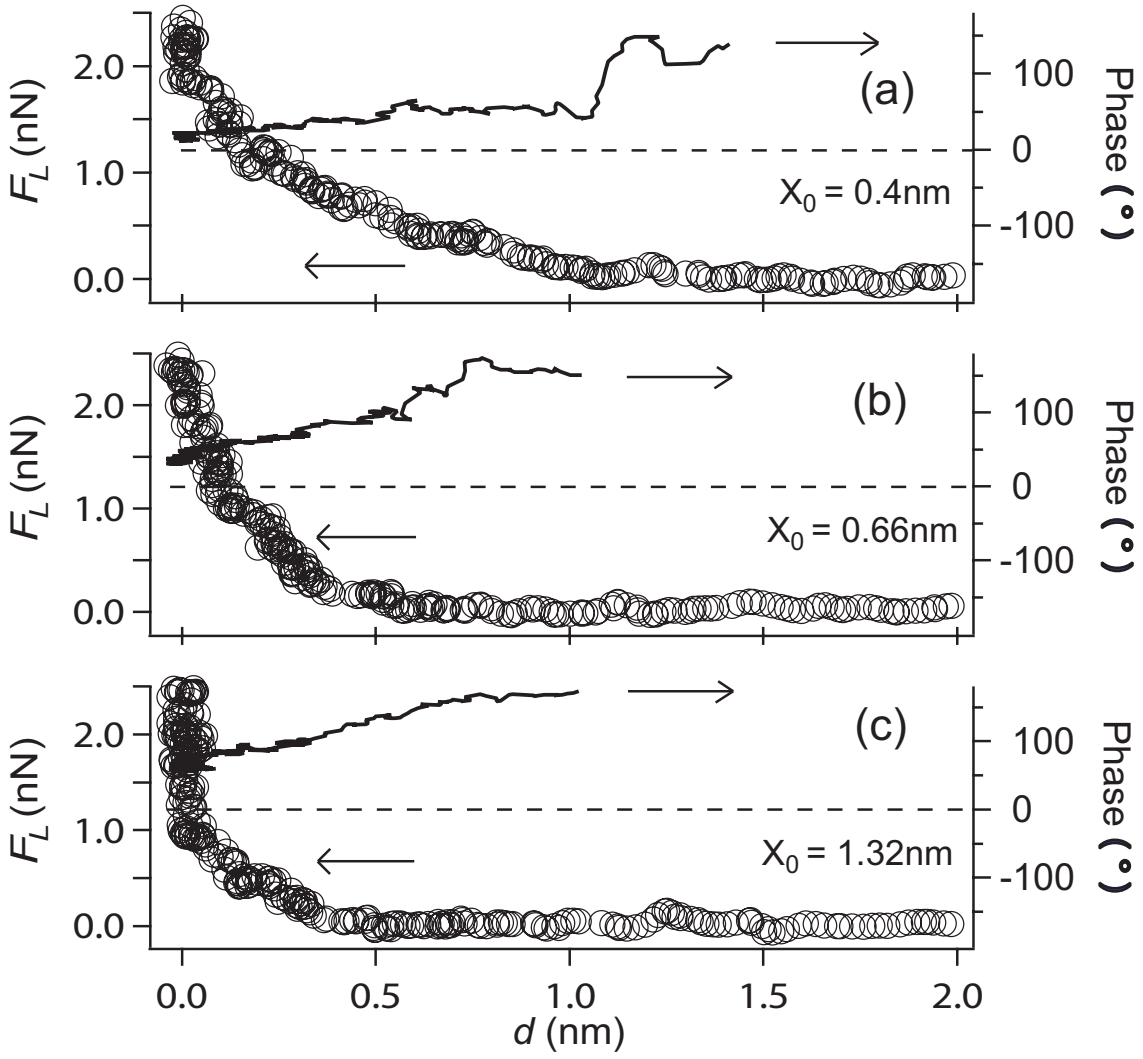

Figure 4.2.1: *F_L and ω in water as a function of d at $\omega = 955.3$ Hz, and for three different X_0 values, (a) $X_0 = 0.4$ nm. (b) $X_0 = 0.66$ nm. (c) $X_0 = 1.32$ nm. The phase for $d > 1$ nm is not shown because it fluctuates randomly*

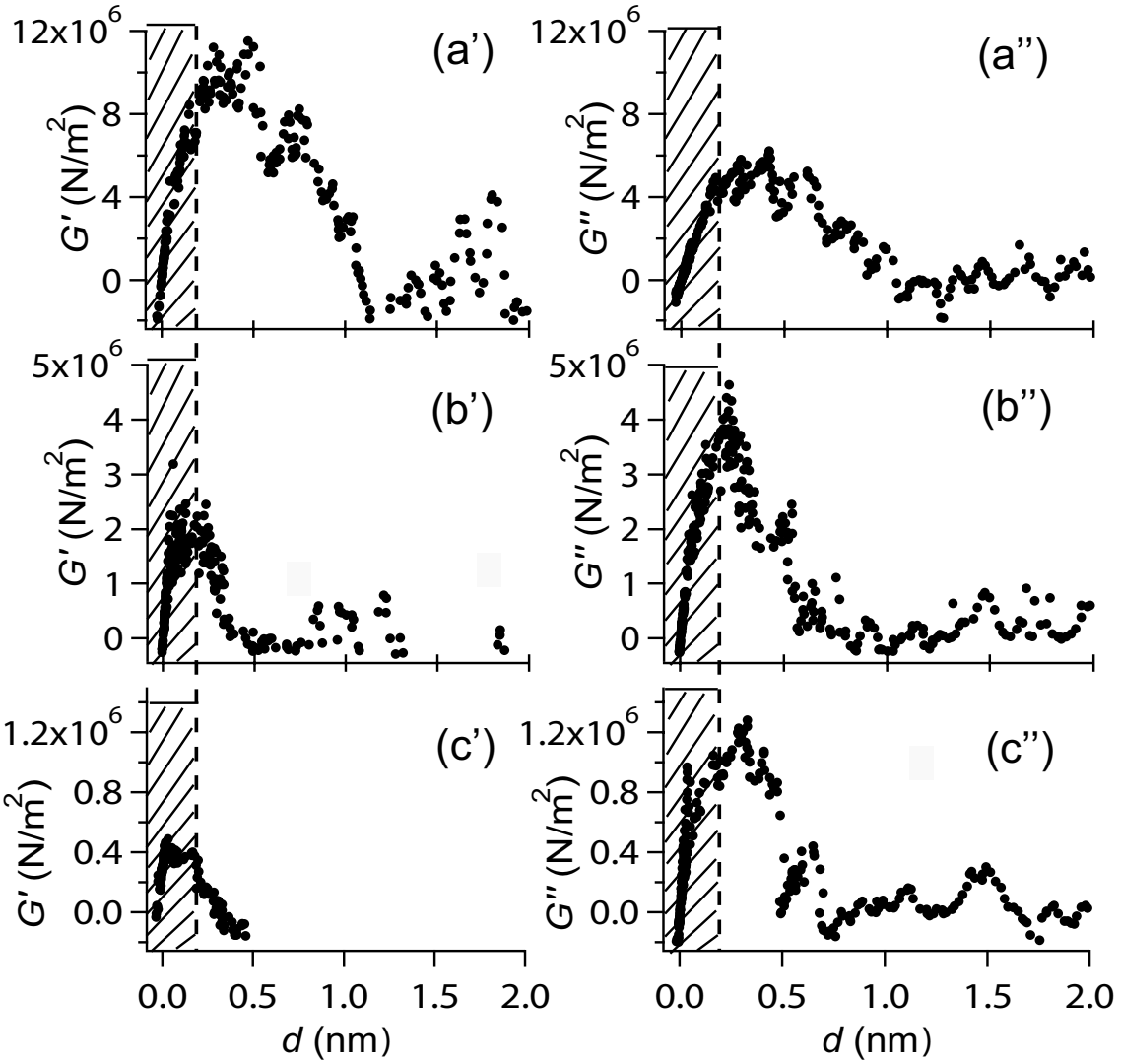

Figure 4.2.2: *G' and G'' in water as a function of tip-sample distance. The shadowed area, $d < 0.2$ nm, is not discussed here because the gap size is smaller than a water molecular dimension. ω is 955.3 Hz, and the X_0 is 0.4 nm for (a') and (a"), 0.66 nm for (b') and (b"), and 1.32 nm for (c') and (c").*

diameter.) Figure 2 shows very clearly that G' and G'' strongly depend on X_0. For large X_0, G'' dominates over G', resulting in the response of nano-confined water becoming purely viscous. Also, by decreasing the gap size, the rise of G' and G'' takes place *later* (smaller d) for larger X_0. Furthermore, for all the investigated X_0, the rise of G'' occurs *earlier* (larger d) than the rise of G'. The dramatic drop of both G' and G'' for $d < 0.2$ nm (shadowed area in Fig. 4.2.2) is due to the invalidity of Eq. 4.2.2 for d smaller than the dimension of one water molecule. Figure 4.2.2 indicates that the shear amplitude dependence of the viscoelastic modulus is very complex and nonlinear. For this reason we have performed measurements over a large range of X_0 and ω (0.06 nm$< X_0 <$ 2.8 nm, 50 Hz $< \omega <$ 2 kHz).

Following the Maxwell model for a linear viscoelastic system, the relationship between the intrinsic relaxation time, τ_0, and the moduli, G' and G'', is given by [46]

$$G' = \frac{G_0(\omega\tau_0)^2}{1+(\omega\tau_0)^2},\ G'' = \frac{G_0(\omega\tau_0)}{1+(\omega\tau_0)^2} \tag{4.2.3}$$

where G_0 is a constant. According to Eq. 4.2.3, G' and G'' do not depend explicitly on γ_0. However, many metastable complex fluids experience a drastic decrease of their structural relaxation time when they are subjected to large strains. This phenomenon gives rise to a strong strain dependence of G' and G'', which can be described by the introduction of an *effective* relaxation time, τ, that depends on the *intrinsic* relaxation time and the strain rate, $\dot{\gamma_0} = \gamma_0 \cdot \omega$ [81]. Once defined τ, it is used to replace τ_0 in Eq. 4.2.3, and thus to predict G' and G'' as a function of the strain. Recently, a phenomenological expression has been found to characterize a $\dot{\gamma_0}$ dependent effective relaxation time in metastable complex fluids [81]

$$\frac{1}{\tau} \simeq \frac{1}{\tau_0} + K \cdot \dot{\gamma_0}^{\nu} \tag{4.2.4}$$

where ν is a positive exponent, and K is a constant. In a glassy system which shows slow dynamics ($\omega \gg \frac{1}{\tau_0}$), $\nu \sim 1$ and $K \sim 1$ [89]. By replacing τ_0 in Eq. 4.2.3 with τ in Eq. 4.2.4 when $\omega \gg \frac{1}{\tau_0}$, the maximum of G'' is near $\gamma_0 \simeq 1$, independently of the

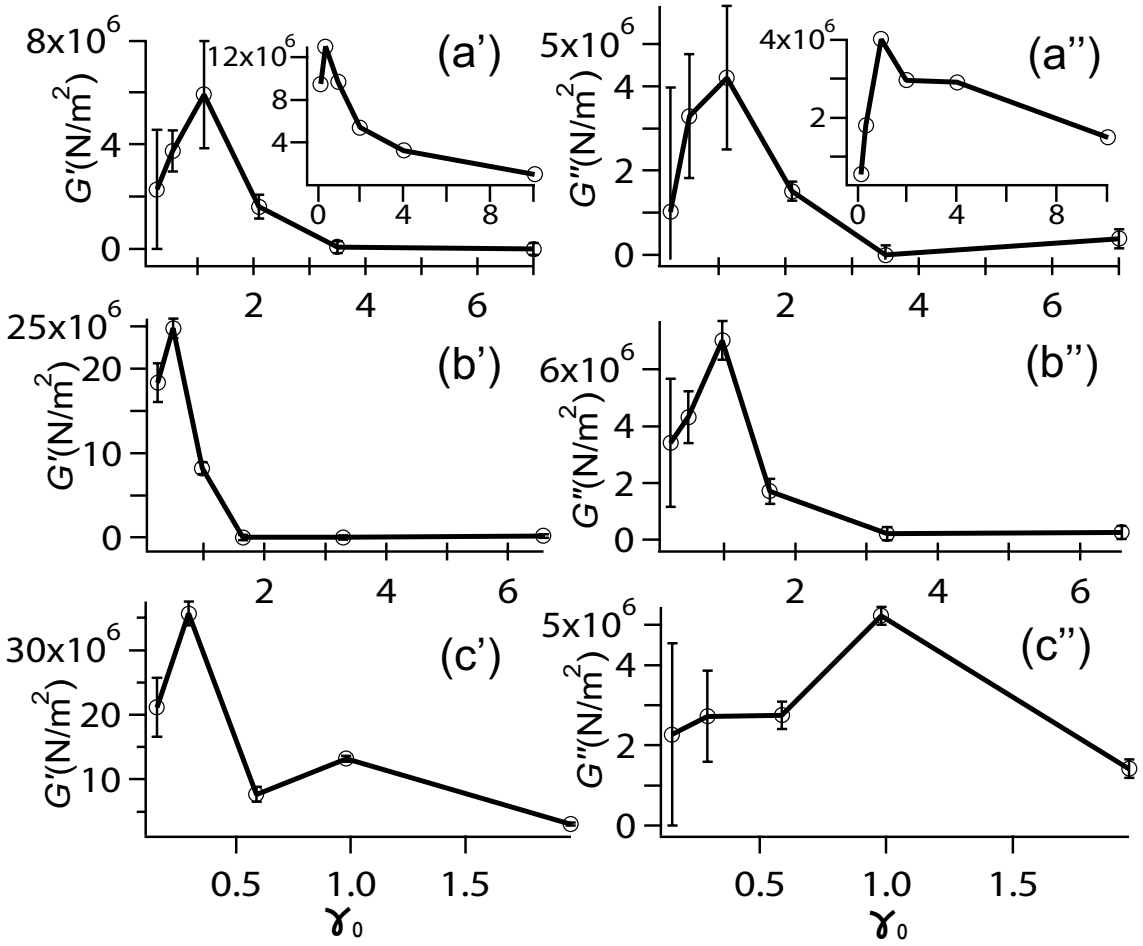

Figure 4.2.3: *At $d = 0.4$ nm, G' and G'' in water as a function of $\gamma_0 = X_0/d$, with ω equals to 52.02 Hz for (a') and (a"), 955.3 Hz for (b') and (b"), and 1.9689 kHz for (c') and (c"). The insets show the results for OMCTS at $d = 1.4$ nm*

ω. Figure 3 presents G' and G'' vs. γ_0 for nano-confined water, obtained by applying Eq. 4.2.2 to the measured F_L and θ at three different ω for $d = 0.4$ nm. In Fig. 4.2.3, G' and G'' show remarkable behaviors: (i) the peak position of G'' is around $\gamma_0 \simeq 1$ over a wide range of frequencies; (ii) for $\gamma_0 < 1$, the viscoelasticity is dominantly elastic, i.e., $G' > G''$; and (iii) G' and G'' decay to zero for large values of γ_0. These features of our nano-confined water system are ubiquitous in metastable complex fluids [81] and they are all captured by the argument of the strain rate dependent τ. Indeed, by using Eq. 4.2.3 and 4.2.4 the shape of the curves presented in Fig. 3 can be fully described. In order to understand if other fluids, newtonian in the non-confined state, behave like metastable complex fluids and follow Eq. 4.2.3 and 4.2.4 once confined, we performed the same measurements in nanoconfined OMCTS. OMCTS is a mica-wetting non-polar liquid, with a molecular diameter of about 0.7 nm. From the measurements showed in the insets of Fig. 4.2.3 and 4.2.4, it is clear that, nano-confined OMCTS also presents a nonlinear viscoelasticity with strain rate dependent effective relaxation times.

4.3 Relaxation Time

From Eq. 4.2.3, τ can be predicted by:

$$\tau = \frac{G'}{G''} \cdot \frac{1}{\omega} \tag{4.3.1}$$

By using Eq. 4.3.1 and the experimental values of G' and G'', τ as a function of $\dot{\gamma_0}$ for water at $d = 0.4$ nm is determined and shown in Fig. 4. The effective relaxation time of nano-confined water decreases from 40 ms to 0.7 ms when $\dot{\gamma_0}$ increases from 14 s^{-1} to 6000 s^{-1}. The nonlinearity of the relaxation time sets in when the experimental time scale ($\dot{\gamma_0}$) is faster than the intrinsic relaxation time (τ_0). In this case, the time response can only be measured effectively as a function of the experimental time scale.

By fitting the data in Fig. 4 with Eq. 4.2.4 we found that $\tau_0 = 0.06 \pm 0.03$ s for nano-confined water at $d = 0.4$ nm. In OMCTS, τ_0 is longer than in water

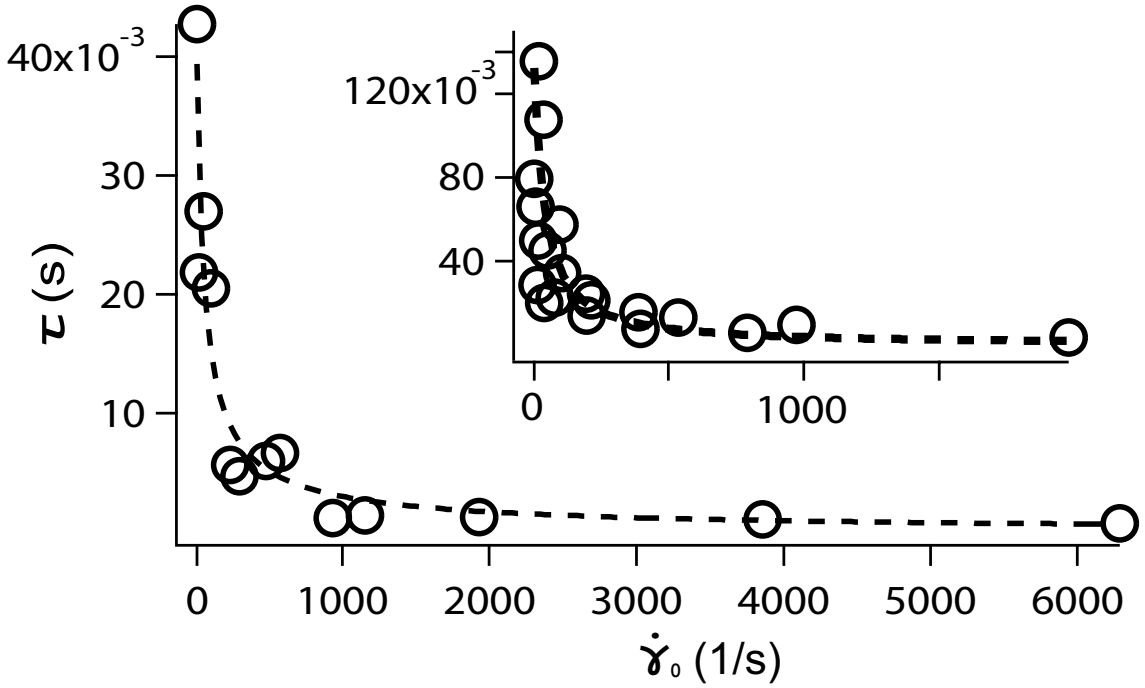

Figure 4.2.4: *τ vs. $\dot{\gamma}_0$ for water at $d = 0.4$ nm. The dash line is the fitting with Eq. 4.2.4 for $K = 0.95 \pm 1.49$ and $\nu = 0.84 \pm 0.29$ [89]. In the inset, the results for OMCTS at $d = 1.4$ nm.*

for the same d, in particular, τ_0 $\sim$0.13 s for $d = 1.4$ nm. The striking result is that the observed τ and τ_0 are orders of magnitude slower than the relaxation time of bulk water and OMCTS at room temperature. The fact that confinement can drastically slow down the dynamics of a fluid has been previously observed in diverse systems [12], such as colloidal suspensions [91], and polymers [86], where for strong fluid-wall interactions, the glass transition temperature is shifted towards high temperatures upon confinement [88]. An alternative way to view this behavior is to consider that the confinement defines an effective temperature of the system which is lower than the canonical temperature [92]. According to a previous study [84], the dielectric relaxation time of supercooled water confined in clays at 175 K is about 0.06 s, similar to the relaxation time found in our experiments on nano-confined water at room temperature. Moreover, the value of the viscosity measured in our investigations is comparable with that of supercooled water at 140 K in a 100 μm

radius tube [93]. A recent study has shown that the dielectric relaxation time of supercooled water is very sensitive to the confinement [94]. For confinement lengths of the order of 1 nm, it was found that, over a wide range of temperatures, the dielectric relaxation times are always longer than in bulk water. In our experiments, we also observe that τ is longer for increased confinement, i.e., with decreasing d. Unfortunately, for $d \geq 1$ nm F_L becomes too small to be measured precisely due to low signal-to-noise ratio. The only information that we can extract is that the intrinsic relaxation time for $d \geq 1$ nm is shorter than 10^{-4} s.

In conclusion, we have studied the viscoelastic properties of nano-confined wetting liquids at 300 K, finding a slow dynamical behavior similar to that observed in metastable complex fluids. By measuring the viscoelastic modulus at different frequencies and strains, the intrinsic relaxation time of nano-confined water is determined to be ≈ 0.06 s. This value is comparable with the dielectric relaxation time measured in supercooled water at 175 K.

CHAPTER V

PERSPECTIVE ON FUTURE DEVELOPMENTS

The properties of fluids in confined geometries depend, as described in the previous chapters, on the fluid molecular structure and the degree of confinement. The future research activity described in this chapter will be focused on fluids confined in gaps and/or channels with dimensions of 20 nm down to 0±0.03 nm. In such a high confinement the properties of liquids are expected to be very different from the properties of bulk liquids.

The goal of future research is to understand the dynamic properties, namely viscosity, slippage and electrokinetic effects, of liquids confined in gaps and/or channels with dimensions in the range 0-20 nm. To achieve this goal we plan to use atomic force microscopes (AFM) equipped with thermal and conductive AFM tips. Chemical and topographical nano-patterning and nano-channels will be prepared by means of a new nano-lithography technique developed by our group in collaboration with the groups of Prof. S. Marder and Prof. W. King at GeorgiaTech.

5.1 Slippage

In classical fluid dynamics, there is the assumption that fluids do not slip on the boundary when flowing across a surface. The "non-slippage" assumption is a good approximation at the macro-scale. However, at the micro- or nano-scale, the usual no-slip (zero-velocity) boundary condition is no longer a good approximation. The slip length is then defined as the distance within the solid where the extrapolated flow velocity is zero, as shown in Fig. 5.1.1. Resent studies show that the slip length of water can be several nanometers to micrometers depending on the wettability and roughness of the boundary surfaces [95]. On hydrophilic surfaces, the slip length of

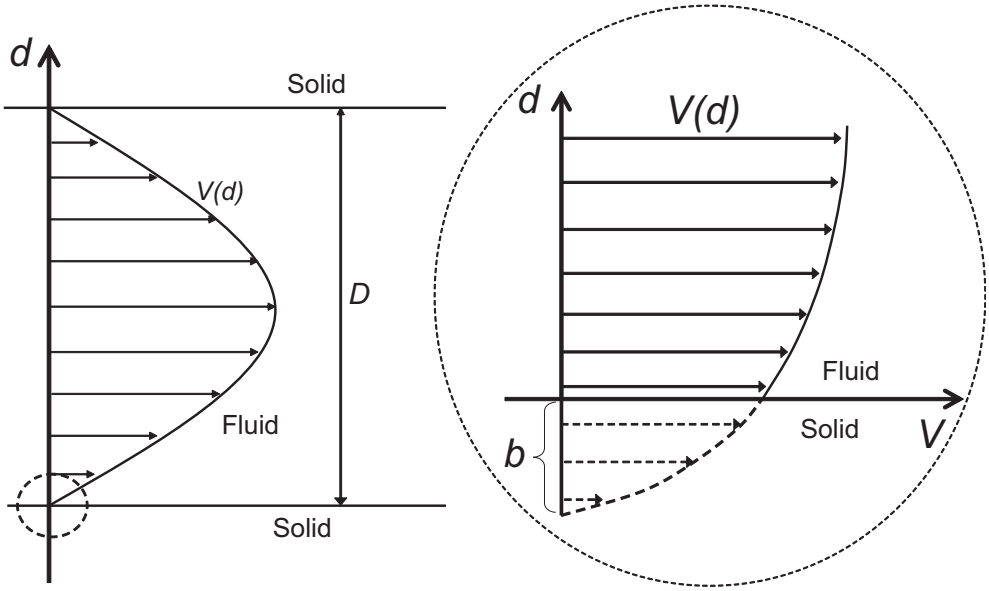

Figure 5.1.1: *Schematic of the definition of the slip length. The left figure shows the case where fluids flow in a macro-scale channel. The right figure shows that the non-slippage condition is not negligible at the nano-scale.*

water is only $\sim$ 1 nm; on hydrophobic surfaces, the slip length can be as long as ~ 1 μm.

In our nano-confined liquids experiments, the equation used for calculating viscosity (Eq. 3.4.1) is also based on the assumption of zero slippage on either the AFM tip or sample surface. The non-zero slip length leads to unexpected flow velocities in Eq. 3.4.1. The viscosity calculated by Eq. 3.4.1 can then be considered as an effective viscosity which can be written as [96]:

$$\eta_{eff} = \frac{\eta_0}{1 + \frac{b}{d}} \tag{5.1.1}$$

where η_0 is the intrinsic viscosity, b is the slip length, and d is the distance between two confining plates.

The surface-dependent slip length offers an alternate physical interpretation of different viscous behaviors on hydrophilic and hydrophobic surfaces presented on chapter III. We argue that the different viscosities measured on wetting and non-wetting surfaces are due to the a slip length on non-wetting surfaces, as compared to wetting

surfaces. In other words, viscous nano-confined fluids slip on hydrophobic surfaces and the measured lateral force is thus reduced by this slippage. In order to extract the slip length of water on a hydrophobic surface (HOPG) from our previous results, we assume that the intrinsic viscosity of water on hydrophilic (mica) and hydrophobic (HOPG) surfaces are equal, $\eta_0^{mica} = \eta_0^{HOPG}$. By arbitrarily fixing the slip length of water on mica (b_{mica}), by using the values of η_{eff}^{mica} and d as measured in Fig. 3.4.1, we can find the intrinsic viscosity of water on mica at different distances ($\eta_0^{mica}\{d, b_{mica}\}$) by means of Eq. 5.1.1. The slip length of water on HOPG can be extracted by substituting the measured η_{eff}^{HOPG} in Fig. 3.4.1 and considering $\eta_0^{HOPG}\{d, b_{HOPG}\}$ as $\eta_0^{mica}\{d, b_{mica}\}$ in $\eta_{eff}^{HOPG} = \frac{\eta_0^{mica}}{1+\frac{b_{HOPG}}{d}}$.

Preliminary results of the slip length of water on HOPG are shown in Fig. 5.1.2. The slip length of water on HOPG (b_{HOPG}) is expected to be constant for different d. Based on this expectation, the results for $b_{mica} = 0 - 1$ nm for $d \leq 1$ nm offer the best fit, corresponding to $b_{HOPG} = 2 - 10$ nm. However, there are some issues related to these preliminary results. First, the resolution of η_{eff}^{HOPG} in Fig. 3.4.1 is not good enough, especially for larger distances, giving rise to larger errors in b_{HOPG}. Second, the intrinsic viscosity for mica and HOPG surfaces (η_0^{mica} and η_0^{HOPG}) are not necessary equal under the same geometrical confinement. Since the liquid molecules are attached or extremely close to the surface, chemical surface energy (wettability) may have an important role in the intrinsic viscosity in nano-confinements. Presently, the group is working on these problems.

5.2 Properties of Liquids Confined in Open Fluid Nano-channels

So far, this thesis has presented results on the rheological and dynamical properties of liquids confined between an AFM tip and a solid sample surface separated less than few nanometers, i.e., confined in a quasi-2-D plane. However in nano-fluidics, a more interesting confined geometry is 1-D, i.e., a nano-channel.

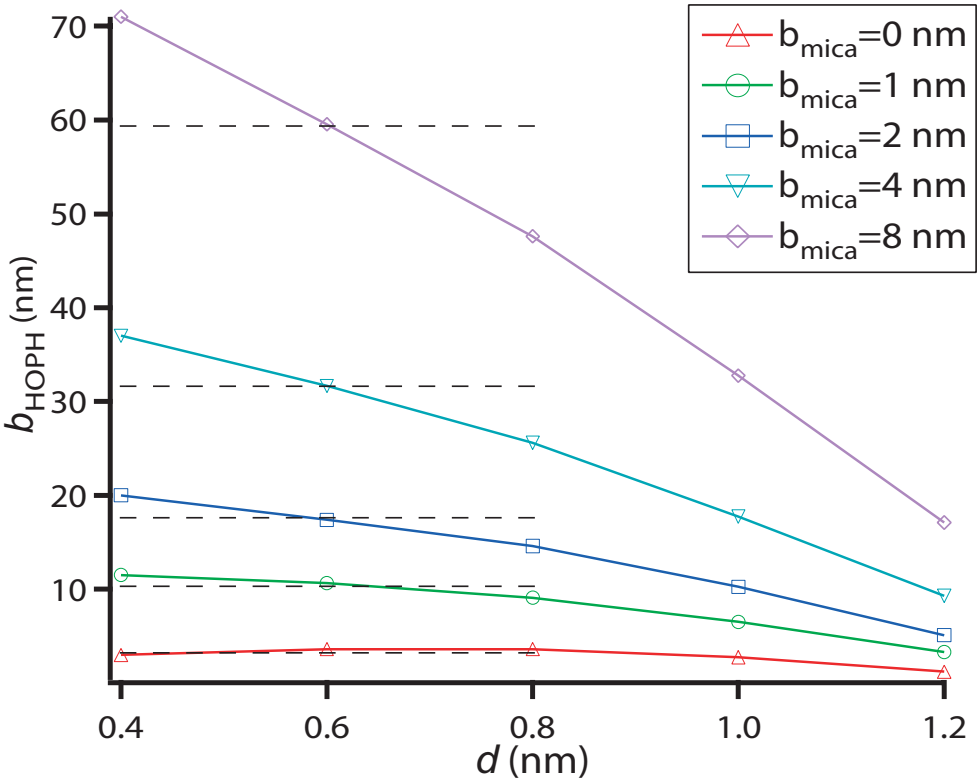

Figure 5.1.2: *The slip length of water on HOPG at different distances and for different chosen* b_{mica}.

Recently, Liu *et al.* [97] measured the shear viscosity of water confined in a single wall carbon nanotube (SWCN) by detecting the difference of stiffness between a SWCN in air and a SWCN filled with water. They observed that the shear viscosity of water confined in a SWCN is twice of the bulk value. However, the geometry, dimension, and wettability of confining surfaces can not be manipulated in this experiment.

A key point in our research is to find a simple, fast and versatile technique to modify and control the topography and chemistry of our surfaces with nano-resolution. Such a technique will give us the possibility to investigate viscosity, slippage, electrokinetic effects and flow of liquids as a function of chemical and topographical nanopatterning.

5.2.1 Thermo- Chemical Nanolitography, TCNL

Recently, we developed a new lithography technique called thermo- chemical nanolitography (TCNL) [38]. TCNL employs a resistively- heated AFM cantilever to induce well-defined chemical reactions to change the surface functionality of thin polymer films (or, potentially, self assembled monolayers). Such an approach is appealing because the thermal profile in the vicinity of a heated AFM tip gives rise to sharp thermal gradients, and the chemical reaction rates increase exponentially with temperature; therefore we can achieve a very high degree of spatial resolution. A wealth of thermally-activated chemistries can feasibly be employed to change the subsequent reactivity, surface energy, solubility, conductivity etc. of the material, as desired. Our TCNL technique can be employed to create a controlled chemical pattern on a polymer surface with high density and at high resolution. Figure 5.2.1 shows the use of TCNL to write a chemical change on a copolymer film by heating it locally with a silicon thermal cantilever (via deprotection of the carboxylic acid functionality). The magnitude of the friction force between the tip and the sample surface is a sensitive

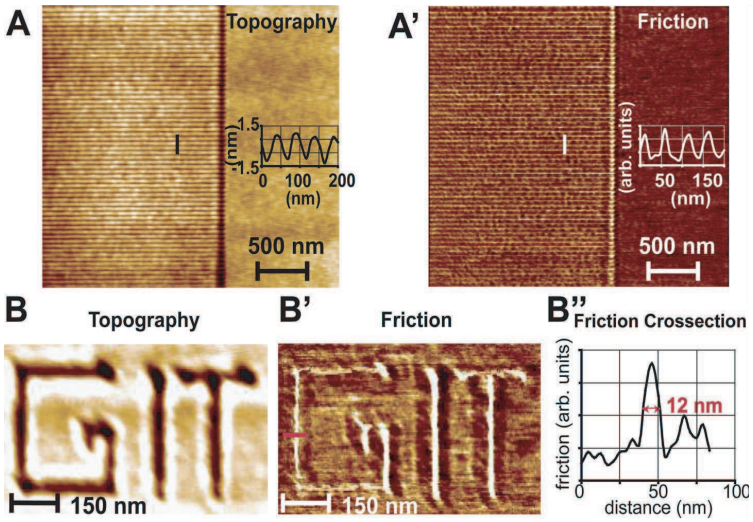

Figure 5.2.1: *(A) AFM topography image and (A') corresponding friction image of a cross-linked* $p(THP-MA)_80p(PMC-MA)_20$ *film showing a high-density line pattern written chemically on the left side. (B) AFM topography and corresponding friction image (B') of a modified copolymer film with the indentation depth kept within 3 nm. (B") The cross-section profile of modified part in (B').*

relative measurement of the sample hydrophilicity, e.g., the larger the friction force, the more hydrophilic the sample [10]. The differences visible in the topographical image arise from desorption of dihydropyran. Figures 5.2.1 B and B' show topography and friction images of "GIT" written chemically on a copolymer sample. Figure 5.2.1 B" gives the cross-section of a friction line, demonstrating that chemically-modified lines can be created easily and reproducibly with a width at half-maximum as small as 12 nm, and the indentation depth kept within 3 nm. By heating at higher temperatures the indentation depth can be increased up to tens of nanometers. The width of the lines can be as large as requested.

5.2.2 Fluid Nanochannels Fabricated by TCNL

Future research activity could include the following experiments:

1. Preparation of surfaces with different chemical and topographical nanopatterns and fabrication of nanochannels with width in the range 5 to 20 nm and depth

in the range of 1.6 to 10 nm.

2. Local (within areas of 1 to 100 nm^2) measurements of the **dynamic viscosity of water and other liquids** in different confined geometries (down to 0.3 nm at least in one direction) as a function of shear velocity, ion concentration, ion specificity, topographical and/or chemical nano-patterning, temperature and electric field, as described in Fig. 5.2.2.

3. Study of the interplay between confinement induced effects on the viscosity and slippage.

4. Study of **electrokinetic effects** as a function of the depth of **nanochannels** that are 5-20 nm wide and 1.6-10 nm deep. Role of ion specificity, ion concentration, surface chemistry, temperature, slip length will also be studied in different nanochannel sizes (See Fig. 5.2.3).

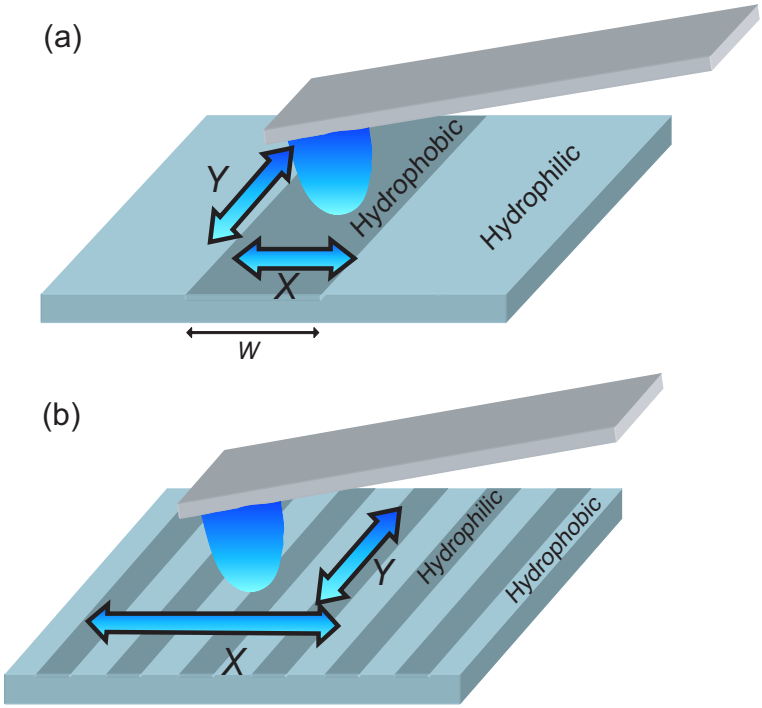

Figure 5.2.2: *Experimental setup for an open 1-D channel, (a), and a nanopatterned surface, (b).*

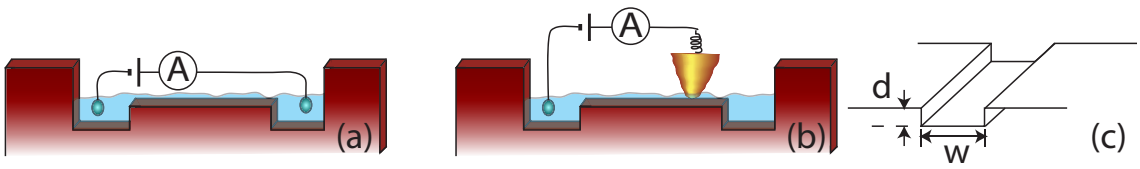

Figure 5.2.3: *a) and b) show Electrokinetic measurements in a nano-channel. c) shows the 3-D view of a nano-channel.*

REFERENCES

[1] J. C. T. Eijkel, and A. van den Berg, Microfluid Nanofluid **1** 249 (2005).

[2] H. G. Craighead, Science **290** 1532 (2000).

[3] T. M. Squires, and S. R. Quake, Rev. Mod. Phys. **77** 977 (2005).

[4] G. M. Whitesides, Nature **442** 368 (2006).

[5] O. Beckstein and M. S.P. Sansom, Phys. Biol. **1**, (2004).

[6] Y. Zhou, J. H. Morais-Cabral, A. Kaufman, and R. Mackinnon, Nature **414**, (2001).

[7] G. Sposito, N. T. Skipper, R. Sutton, S. H. Park, A. K. Soper, and J. A. Greathouse, Proc. Natl. Acad. Sci. **96** 3358 (1999).

[8] E.-M. Choi, et al., Phys. Rev. Lett. **95**(085701) (2006).

[9] R. Szoszkiewicz, and E. Riedo, Appl. Phys. Lett. **87** 033105 (2005).

[10] R. Szoszkiewicz and E. Riedo, Phys. Rev. Lett. **95**, 135502 (2005).

[11] L. Sirghi, R. Szoszkiewicz, and E. Riedo, Langmuir **22** 1093 (2006).

[12] H.-W. Hu, et al., Phys. Rev. Lett. **66**, 2758 (1991).

[13] J. Isrealachivili, Intermolecular and Surface Forces **2nd 0123751810** (1991).

[14] J. Gao, W. Luedke, and U. Landman, J. Phys. Chem. B **101**, 4013(1997).

[15] F. Mugele, and M. Salmeron, Phys. Rev. Lett. **84** 5796 (2000).

[16] S. Granick, Z. Q. Lin, and S. C. Bae, Nature **425** 467 (2003).

[17] Y. Zhu, and S. Granick, Langmuir **19** 8148 (2003).

[18] A. L. Demirel, and S. Granick, J. Chem. Phys. **115** 1498 (2001).

[19] A. L. Demirel, and S. Granick, Phys. Rev. Lett. **77** 2261 (1996).

[20] M. Heuberger, M. Zach, and N. D. Spencer, Science **292** 905 (2001).

[21] R. Zangi, and A. E. Mark, Phys. Rev. Lett. **91** 025502 (2003).

[22] R. J. Mashl, S. Joseph, N. R. Aluru, and E. Jakobsson, Nature **412** 802 (2001).

[23] K. Koga, G. T. Gao, H. Tanaka, and X. C. Zeng, NanoLetters **3** 589 (2003).

[24] U. Raviv, P. Laurat, and J. Klein, Nature **413**, 51 (2001).

[25] U. Raviv, and J. Klein, Scisnce **297**, 1540(2002).

[26] Y. Zhu and S. Granick, Phys. Rev. Lett. **87**, 096104 (2001).

[27] T. R. Jensen, M. O. Jensen, N. Reitzel, K. Balashev, G. H. Peters, K. Kjaer, and T. Bjornholm, Phys. rev. Lett. **90** 086101 (2003).

[28] R. Steitz, T. Gutberlet, T. Hauss, B. Klosgen, R. Krastev, S. Schemmel, A. C. Simonsen, and G. H. Findenegg, Langmuir **19** 2409 (2003).

[29] K. Leung, A. Luzar, and D. Bratko, Phys. Rev. Lett. **90** 065502 (2003).

[30] K. Lum, D. Chandler, and J. D. Weeks, J. Phys. Chem. B **103** 4570 (1999).

[31] D. Schwendel, T. Hayashi, R. Dahint, A. Pertsin, M. Grunze, R. Steitz, and F. Schreiber, Langmuir **19** 2409 (2003).

[32] S. Jarvis, T. Uchihashi, T. Ishida, H. Tokumoto, and Y. Nakayama, J. Phys. Chem. B **104**, 6091(2000)

[33] J. Israelachivili, and R. Pashley, Nature **306**, 249(1983).

[34] K. Koga, J. Chem. Phys. **116** 10882 (2002).

[35] M. Rovere, and P. Gallo, J. Phys.:Condens. Matt. **15** s145 (2003).

[36] J. P. Cleveland, T. E. Schaffer, and P. K. Hansma, Phys. Rev. B **52**, R8692(1995).

[37] S. O'Shea, and M. Welland, Appl. Phys. Lett. **60**, 2356(1992).

[38] R. Szoszkiewicz, T. Okada, S. C. Jones, T.-D. Li, W. P. King, S. R. Marder, and E. Riedo, Nanoletters **7**, 1064(2007).

[39] W. H. Keesom, Physik. Zeitschr. **22** (129) (1921).

[40] P. Debye, Zeitschr. f. Physik. **63** (17) (1930).

[41] F. London, Physik. Zeitschr. **22** (129) (1921).

[42] B. Derjaguin, KOLLOID-ZEITSCHRIFT **69** (155) (1934).

[43] R. Hunter, Foundations of Colloid Science **2nd 0198505027** (2001).

[44] F. F. Abraham, J. Chem. Phys. **78** (1978).

[45] H. Brenner, Chem. Eng. Sci. **16** (1961).

[46] J. D. Ferry, *Viscoelastic Properties of Polymers* (Willey, 1980), 3rd ed., ISBN 0-471-04894-1.

[47] G. Binnig, C. F. Quate, and Ch.. Gerber, Phys. Rev. Lett. **376** (1986).

[48] V. Franz, and H. Butt, J. Phys. Chem. B **106** (2002).

[49] R. Lim, and S. J. O'Shea, Phys. Rev. Lett. **88**(24) (2002).

[50] S. Jeffery, P. M. Hoffmann, J. B. Pethica, C. Ramanujan, H. O. Ozer, and A. Oral, Phys. Rev. B **70** (2004).

[51] D. Tabor, and R. H. S. Winterton, Proc. R. Soc. Lond. A. **312** (1969).

[52] J. N. Israelachivili, and G. Adams, J Chem. Soc.- Faraday Trans. I. **74** (1978).

[53] R. G. Horn, J. N. Israelachivili, J. Chem. Phys. **75** (1981).

[54] U. Raviv, J. Klein, and P. Laurat, Nature **413** (2001).

[55] J. N. Israelachivili, and P. M. MaGuiggan, Science **241** (1988).

[56] F. J. Giessibl, and C. F. Trafas, Rev. Sci. Instrum. **65** (1994).

[57] J.E. Sadar, and S. P. Jarvis, Appl. Phys. Lett. **84** 10 (2004).

[58] T. Uchihashi, et al., Nanotechnology **16**, S49 (2005).

[59] J. E. Houston, and H. I. Kim, Acc. Chem. Res. **35** (7) (2002).

[60] M. Antognozzi, et al., Appl. Phys. Lett. **78**, 300 (2001).

[61] R. C. Major, J. E. Houston, M. J. McGrath, J. I. Siepmann, and X.-Y. Zhu, Phys. Rev. Lett. **96**, 177803(2006).

[62] B. V. Zhmud, A. Meurk, and L. Bergstrom, J. Coll. Interf. Sci. **207** 332 (1998).

[63] J. Klein, and E. Kumacheva, Science **269** (1995).

[64] R. W. Carpick, et al., Appl. Phys. Lett. **70**(12), 24 (1997).

[65] Y. Song, B. Bhushan, Phys. Rev. B **74**(165401) (2006).

[66] K. L. Johnson, Contact Mechanics 0521347963 (2003)

[67] R. Luthi E. Meyer, L. Howald, W. Gutmannsbauer, M. Giggisberg, M. Bammerlin, and H.-J. Guntherodt, Surf. Sci. **338**, (1995).

[68] K.-H. Chung Y.-H. Lee and D.-E. Kim, Ultramicroscopy **102**, (2005).

[69] M. Scherge, X. Li, and J. A. Schaefer, Tribol. Lett. **95**, 135502(2005).

[70] S. Jeffery, et al., Phys. Rev. B **70**(054114) (2004).

[71] H. Kim, J. Kushmerick, J. Houston, and B. Bunker, Langmuir **19**, 9271(2003).

[72] Y. Leng, and P. T. Cummings, Phys. Rev. Lett. **94**, 026101(2005).

[73] P. B. Miranda, L. Xu, Y. R. Shen, and M. Salmeron, Phys. Rev. Lett. **81**, 5876(1998).

[74] J. Gao, W. Luedke, and U. Landman, Phys. Rev. Lett. **79**, 705(1997).

[75] L. Cheng, P. Fenter, K. K. Nagy, M. L. Schlegel, and N. C. Sturchio, Phys. Rev. Lett. **87**, 156103(2001).

[76] U. Raviv, S. Gaisson, J. Frey and J. Klein, J. Phys.: Condensed Matt. **14**, 9275 (2002).

[77] T. J. Senden, and C. J. Drummond, Col. Sur. A **94** 29 (1995).

[78] R. M. Pashley, J. Coll. Interf. Sci. **83** 531 (1981).

[79] A. J. Goldman, R. G. Cox, and H. Brenner, Chem. Eng. Sci. **22**, 637(1967).

[80] E. Kumacheva, and J. Klein, J. Chem. Phys. **108**, 6996(1998).

[81] K. Miyazaki, et al., Europhys. Lett. **3** (2006).

[82] M. D. Ediger, et al., J. Phys. Chem. **100** (1996).

[83] N. Giovambattista, et al., J. Phys. Chem. B **108**, 6655 (2004).

[84] S. Cerveny, et al., Phys. Rev. Lett. **93**, 245702 (2004).

[85] E. Riedo, F. Levy, and H. Brune, Phys. Rev. Lett. **88**, 185505 (2002).

[86] M. Alcoutlabi and G. B. McKenna, J. of Phys.: Cond. Matt. **17** (2005).

[87] From the results in Fig. 2, the shear elastic mudulus of nanoconfined water, G', is three orders of magnutide smaller than the shear modulus of silicon, $G^s \simeq 50$ GPa. The tip-water contact lateral stiffness is approximately equal to $K_L^c \sim 8a(\frac{1}{G'} + \frac{1}{G^s})^{-1} \sim 0.4$ N/m, (a is the contact radius, $a \simeq 4.5$ nm in these experiments), which is two orders of magnitude smaller than the torsion and lateral force constant.

[88] P. Scheidler, et al., Europhys. Lett. **59**(5), 701 (2002).

[89] K. Miyazaki and D. R. Reichman, Phys. Rev. E **66**(050501(R)) (2002).

[90] J. Gao, W. Luedke, and U. Landman, **102**(5033) (1998).

[91] C. R. Nugent, et al., arXiv:cond-mat/0601648v1 (2007).

[92] M.-C. Bellissent-Funel, J. Phys. Cond. Matt. **13**, 9165 (2001).

[93] J. Hallett, Proc. Phys. Soc. of London **82** (1963).

[94] J. Swenson, et al., Phys. Rev. Lett. **96**, 247802 (2006).

[95] P. Joseph, C. Cottin-Bizonne, J.-M. Benoit, C. Ybert, C. Journet, P. Tabeling, and L. Bocquet, Phys. Rev. Lett. **97** 156104 (2006).

[96] L. Bocquet, J.-L. Barrat, Soft Matter **3**, 685 (2007).

[97] Y. Liu, and Q. Wang, Phys. Rev. B **72** 085420 (2005).

LIST OF PUBLICATIONS

This thesis is partly based on the following articles:

1. T.-D. Li and E.Riedo, *"Nonlinear Viscoelastic Dynamics of Nanoconfined Wetting Liquids"*, Phys. Rev. Lett. **100**, 106102 (2008).

2. T.-D. Li, J. Gao, R. Szoszkiewicz, U. Landman, and E. Riedo, *"Structured and viscous water in subnanometer gaps"*, Phys. Rev. B **75**, 115415 (2007).

3. R. Szoszkiewicz, T. Okada, S. C. Jones, T.-D. Li, W. P. King, S. R. Marder, and E. Riedo, *"High-Speed, Sub-15 nm Feature Size Thermochemical Nanolithography"* , Nanoletters **7**, 1064 (2007).

4. S. Yoo, W. J. Potscavage Jr., B. Domercq, S.-H. Han, T.-D. Li, S. C. Jones, R. Szoszkiewicz, D. Levi, E. Riedo, S. R. Marder, B. Kippelen, *"Analysis of improved photovoltaic properties of pentacene/$C_6$0 organic solar cells: Effects of exciton blocking layer thickness and thermal annealing"*, Solid-State Electronics **51**, 1367 (2007)

5. T.-D. Li and E. Riedo, *"AFM based method for nano-rheology studies"* in preparation for submission to Rev. Sci. Ins.